Technische Universität München
TUM School of Engineering and Design

Feasibility studies for the identification of plastics on land surfaces and their functional assignment using optical remote sensing

Shanyu Zhou

Vollständiger Abdruck der von der TUM School of Engineering and Design der Technischen Universität München zur Erlangung einer

Doktorin der Ingenieurwissenschaften (Dr.-Ing.)

genehmigten Dissertation.

Vorsitz:

Prof. Dr.-Ing. Yuanyuan Wang

Prüfer*innen der Dissertation:

1. Prof. Dr.-Ing. Xiao Xiang Zhu
2. Hon.-Prof. Dr. Michael Rast
3. Prof. Dr. Hannes Feilhauer

Die Dissertation wurde am 16.05.2023 bei der Technischen Universität München eingereicht und durch die TUM School of Engineering and Design am 16.08.2023 angenommen.

Abstract

This PhD thesis focuses on the feasibility of using different spatial and spectral resolutions in optical remote sensing to identify distinct types of plastics on land surfaces at the best possible rate and to associate them with their respective functions. The work consists of three substantively interrelated studies that build on each other and investigate the possibilities and limitations of super- to hyperspectral remote sensing techniques, methods and machine learning algorithms to accurately classify various plastic materials.

The first study examines the use of WorldView-3 (WV-3) satellite data to detect plastic materials on land surfaces. The study provides a detailed explanation of the spectral features of plastics in the short-wave infrared (SWIR) range and groups plastic materials into three clusters, one aliphatic and two aromatic, according to their molecular structure. A knowledge-based decision-tree classifier has been developed built on diagnostic spectral features of plastic materials in the SWIR range and applied to laboratory, aircraft and WV-3 satellite data to identify the different groups of plastic materials. The study concludes that the combination of WV-3 data and the newly designed classifier is an efficient and reliable approach for global monitoring and identifying plastic materials on different backgrounds.

The second study expands on the first by investigating the feasibility of identifying distinct types of plastics using deep - and machine learning models based on hyperspectral satellite data. The study creates a comprehensive database of mixed pixels of different plastic and non-plastic materials using in-house and public spectral libraries. The algorithms selected for classification are a Convolutional Neural Network (CNN), a Random Forest (RF) approach, and a Support Vector Machine (SVM). The study validates its models using a test group of the spectral database and controlled laboratory as well as aircraft experiments. Ten different plastic materials can be identified this way whereby the RF classifier is the most robust one, followed by the SVM and CNN models. The RF further outperforms the other two models in the evaluation of the aircraft data from controlled experiments. The RF is then applied to one GaoFen-5 and two PRISMA satellite recordings of the coastal area in Weifang City, Shandong Province, China, producing transferable results with a very high accuracy of about 96%.

The third study is a continuation of the second one and focuses on a machine-aided association of the hyperspectrally detected plastic materials to their respective functionality using deep learning models trained with Sentinel-2 satellite imagery. The study identifies five major functional types of plastics in the investigated area, namely plastic cover sheetings for construction areas, greenhouse structures, photovoltaic panels (PVs), roof materials, and sport field floorings. Among several models deployed, a VGGNet-13 achieved an overall accuracy of 78% on the test dataset. The model performs well in identifying PVs, greenhouses, and covered construction sites, with F1 scores of 0.85, 0.77, and 0.71, respectively. The results thus indicate that deep learning algorithms trained by Sentinel-2 satellite imagery are suitable to associate the respective functions to plastic materials on land surfaces.

Overall, this thesis provides a comprehensive research and contributes to the development of efficient and reliable approaches for monitoring and identifying various types of plastic materials on land surfaces using optical remote sensing combined with machine learning, and deep learning algorithms. The findings of this thesis also serve for issues such as environmental monitoring, waste management, and resource conservation efforts.

Zusammenfassung

Die vorliegende Dissertation befasst sich mit der Machbarkeit, unterschiedliche räumliche und spektrale Auflösungen in der optischen Fernerkundung zu nutzen, um verschiedenartige Kunststoffmaterialien auf Landoberflächen bestmöglich zu identifizieren und sie mit ihren jeweiligen Funktionen zu verknüpfen. Die Arbeit besteht aus drei inhaltlich zusammenhängenden, aufeinander aufbauenden Studien, in denen die Möglichkeiten und Grenzen von super- bis hyperspektralen Fernerkundungstechniken, Methoden und Algorithmen des maschinellen Lernens zur genauen Klassifizierung verschiedener Kunststoffmaterialien untersucht weden.

In der ersten Studie wird die Verwendung von WorldView-3 (WV-3) Satellitendaten zur Erkennung von Kunststoffen auf Landoberflächen untersucht. Die Studie liefert eine detaillierte Erläuterung der spektralen Merkmale von Kunststoffen im kurzwelligen Infrarotbereich (SWIR) und sortiert diese auf der Grundlage ihrer Molekularstruktur in drei Gruppen, eine aliphatische und zwei aromatische. Basierend auf diagnostischen Spektralmerkmalen im SWIR-Bereich wird ein wissensbasierter Entscheidungsbaum-Klassifikator entwickelt und auf Labordaten, Flugzeugaufzeichnungen und WV-3 Satellitendaten angewendet. Die Studie kommt zu dem Schluss, dass die Kombination von WV-3-Daten und dem neu entwickelten Klassifikator ein effizienter und zuverlässiger Ansatz für ein globales Monitoring und die Identifizierung von Kunststoffmaterialien auf unterschiedlichen Landoberflächen ist.

Die zweite Studie baut auf der ersten auf, indem sie die Möglichkeiten zur Identifikation von Kunststoffen mit Hilfe von Modellen des maschinellen Lernens auf der Grundlage von hyperspektralen Satellitendaten untersucht. Dabei wird unter Verwendung eigener und öffentlicher Spektralbibliotheken eine umfassende spektrale Datenbank aus Mischsignaturen, bestehend aus unterschiedlichsten Kunststoffen und Nicht-Kunststoffen erstellt. Die für die Klassifizierung ausgewählten Algorithmen sind ein 'Convolutional Neural Network' (CNN), der 'Random Forest' Ansatz (RF) und eine 'Support Vector Maschine' (SVM). Die Studie validiert ihre Modelle anhand einer Testgruppe aus der Spektraldatenbank und kontrollierten Labor- und Flugzeugexperimenten. Das Ergebnis ist die Identifikation von 10 verschiedenartigen Plastikmaterialien, wobei der RF-Klassifikator die besten Ergebnisse liefert, gefolgt von den Modellen SVM und CNN. Der RF-Ansatz übertrifft die beiden anderen Modelle auch bei der Auswertung der Flugzeugdaten aus kontrollierten Experimenten. Zuletzt wird der RF-Algorithmus auf eine GaoFen-5 und zwei PRISMA Satellitenaufnahmen des Küstengebiets von Weifang City, Provinz Shandong, China, angewendet und liefert übertragbare Ergebnisse mit einer sehr hohen Genauigkeit um die 96%.

Die dritte Studie ist eine Fortsetzung der zweiten und konzentriert sich auf eine rechnergestützte Zuordnung der hyperspektral detektierten Kunststoffe zu einer entsprechenden Funktionalität. Dabei kommen Deep-Learning-Modelle zum Einsatz, die mit Hilfe von Sentinel-2-Satellitenbildern trainiert worden sind. Die Studie identifiziert dabei fünf wichtige, häufig vorzufindende Funktionsarten von Kunststoffen im Untersuchungsgebiet, nämlich als Kunststoffabdeckungen für Baugebiete, Gewächshausstrukturen, Pho-

tovoltaikmodule (PV), Dachmaterialien und Beläge von Sportplätzen. Dabei wird, unter vielen getesteten Modellen, mit einem VGGNet-13 eine Gesamtgenauigkeit von 78% im Testdatensatz erreicht. Das Modell schneidet bei der Identifizierung von Photovoltaikanlagen, Gewächshäusern und überdachten Baustellen gut ab, mit F1-Werten von 0,85, 0,77 bzw. 0,71. Damit zeigen diese Ergebnisse, dass Deep-Learning-Algorithmen, die über Sentinel-2-Satellitenbildern trainiert wurden, zur Identifizierung von Kunststofffunktionen auf Landoberflächen geeignet sind.

Insgesamt gesehen liefert diese Arbeit einen umfassenden Forschungsbeitrag zur Entwicklung effizienter und zuverlässiger Ansätze für das Monitoring und die Identifizierung von Kunststoffen auf Landoberflächen basierend auf Daten und Methoden der optischen Fernerkundung in Kombination mit maschinellen Deep-Learning-Algorithmen. Die Ergebnisse dienen des Weiteren der Umweltüberwachung, der Abfallwirtschaft und dem Ressourcenschutz.

Acknowledgements

As I stand here at the culmination of my arduous journey, I am filled with gratitude for the many souls who have graced my path, lending unwavering support both in body and spirit. The ups and downs were endless, a constant flux of joy and sorrow, triumph and defeat, comings and goings, punctuated by breathtaking vistas that stirred the soul. Adventures and obstacles arose at every turn, thwarting progress at times, but with dogged determination, I have finally arrived at the end of my Ph.D. candidacy. And so, with the curtain about to fall, I will endeavor to express my heartfelt appreciation to all who have made this feat possible.

First, I would like to express my sincere appreciation to Charly (Prof. Hermann Kaufmann) for his constant support and trust in my work. I appreciate his innovative ideas and unconventional approach, as well as his availability to answer questions and discuss my research. He consistently offers valuable recommendations and constructive critiques that have aided me in enhancing my work. His unwavering support during challenging times and giving me the freedom to work independently have been invaluable.

Although my time as a member of Prof. Xiaoxiang Zhu's team has been brief, I am deeply grateful for the opportunity to pursue my PhD under her guidance. Her leadership serves as an excellent example for me, both as a competent researcher and a responsible person for a team. Behind the scenes, she provides helpful suggestions and critiques to aid in the progress of students. Furthermore, she frequently offers opportunities for members of the group to attend international conferences and present their research to the community. In her personal life, she fosters a friendly and stress-free atmosphere for group members by organizing outdoor activities and encouraging open communication.

I would like to express my special gratitude to Ms. Sylvia Magnussen for her exceptional management of IT and computer-related matters that have made my research life smoother and more efficient. Her friendly and helpful demeanor has been invaluable in assisting me with technical issues such as Linux. Her assistance has saved me a significant amount of time during my Ph.D. studies, and I am grateful for her support. I also want give my sincere thanks to Mrs. Claudia Wartenberg, Dr. Julia Kollofrath, and Yingjie Schreiber-Liu for the scientific management and secretary issues that ensure and ease my research life. In addition, I would like to express my sincere gratitude to Eleonora Weiss and Frau Stefanija Stiebre at the TUM Graduate Center for their patient responses and valuable assistance throughout my enrollment at TUM and through my application for a thesis defense.

I express gratitude to all of my collaborators, coauthors, and anonymous reviewers who have contributed to my work. Specifically, I want to acknowledge Dr. Karl Segl, Dr. Mathias Bochow and Dr. Theres Kuester for their invaluable support and contributions to our collaborative efforts, including the provision of excellent satellite data. Their feedback and insights have significantly improved the quality of our research, and their support for field work has provided me with valuable opportunities for experimentation. I would also like to extend my thanks to Dr. Lichao Mou for his contributions to my research, including his critical feedback and unwavering motivation. Additionally, I thank

Dr. Yuansheng Hua, Dr. Niklas Bohn, Dr. Maximilian Brell and Mr. Lixian Zhang for their cooperation, guidance, and contributions to our collaborative work, which have given me a comprehensive understanding of various fields related to our research.

I also would like to thank all the collegues in GFZ section 1.4, especially Prof. Sabine Chabrillat, Dr. Robert Milewski, , Dr. Christian Mielke, Dr. Monika Göldel, Friederike Kästner, and Nicole Köllner for their kind help and guidance, especially during the initial stage of my Ph.D. program. Their expertise and knowledge in various domains were invaluable to me and helped me gain a deeper understanding of my research area. They are generous scholars who are always ready to provide professional support and insightful discussions.

Furthermore, I would like to express my deep gratitude to my office mate Zhuge Xia, with whom I shared the struggles of pursuing a doctoral degree and offered each other mutual support. I am truly thankful for all the friends and colleagues I met during my Ph.D. life, including Dr. Mimi Peng, Dr. Deying Ma, Zhiyuan Wang, Carolina Cañizares, Wandi Wang, Xiaohang Wang, Chenyu Wang, Yan Ye, Shijing Chen, Dr. Chao Zhou, Haonan Jiang, Tianqi Xiao and all the above-mentioned persons. I also appreciate Fang Xu for her warm welcome in TUM and introducing me to her friends. Truly thanks to new colleagues and friends I met near the end of my Ph.D.: Zhenghang Yuan, Daixin Zhao, Pu Jin, Konrad Heidler, Tian Li, and Dr. Qian Song, The time we spent together, whether cycling, traveling, hiking, wandering, sharing meals and drinks, or having game nights, is something I cherish deeply. The memories of tackling challenging together still inspire me when I face obstacles.

Finally, I want to express my utmost appreciation to my family, my besties Xinyue Yin and Jia Zheng, who have always supported my decisions. I am thankful to my parents for their trust, constant communication, and assistance, particularly during the challenging times of the pandemic. Working from home brought about significant changes and difficulties, and their support was crucial in helping me overcome depression and complete my Ph.D. studies.

Contents

List of Abbreviations

Abbreviation	Description
ABS	Acrylonitrile Butadiene Styrene.
CHIME	Copernicus Hyperspectral Imaging Mission for the Environment.
CNN	Convolutional Neural Network.
EnMAP	Environmental Mapping and Analysis Program.
ESA	European Space Agency.
EVAC	Ethylene Vinyl Acetate Copolymer.
FOV	Field of View.
GF-5	GaoFen-5.
GSD	Ground Sampling Distance.
IFOV	Instantaneous Field of View.
MLE	Maximum Likelihood Estimation.
NIR	Near-Infrared.
OLI	Operational Land Imager.
PA	Polyamide.
PBAT	Polybutylene Adipate Terephthalate.
PC	Polycarbonate.
PE	Comprising Polyethylene.
PET	Polyethylene Terephthalate.
PMMA	Polymethyl Methacrylate.
POM	Polyoxymethylene.
PP	Polypropylene.
PRISMA	PRecursore IperSpettrale della Missione Applicativa.
PS	Polystyrene.
PU	Polyurethane.
PVC	Polyvinylchloride.
RF	Random Forest.
RGB	Red, Green, Blue.
SAM	Spectral Angle Mapper.

Abbreviation	**Description**
SAN	Styrene-Acrylonitrile.
SBG	Surface Biology and Geology.
SHALOM	Space Hyperspectral Applications Land and Ocean Mission.
SVM	Support Vector Machine.
SWIR	Shortwave Infrared.
TIR	Thermal Infrared.
UAV	Unmanned Aerial Vehicle.
VNIR	Visible and Near-Infrared.

1 Introduction

1.1 Outline

This thesis contains an introduction (Chapter 1), a theoretical background (Chapter 2), a description of the methodology used (Chapter 3), three main chapters representing the three manuscripts published (Chapter 4-6), and an overall synthesis and discussion (Chapter 7). Chapter 4 and 5 are original publications that have been published in the journal *Remote Sensing of Environment*. Chapter 6) has been submitted to a further peer-reviewed scientific journal and is currently awaiting review. All work represents stand-alone independent research. There is some overlapping of general information between publications, particularly in the description of the study areas, as all work was conducted at the same test sites. Applied spectroscopic methods, e.g. field reflectance measurements and laboratory analysis are valid throughout all studies.

1.2 Motivation and objectives

Plastic products are increasingly dominating the market since being widely introduced in the 1930s due to their characteristics such as low weight, water resistance, and durability. Thereby the global manufacturing of plastics has quadrupled over the last four decades (Geyer et al., 2017). Now, the inappropriate disposal of plastic waste, along with its longevity and durability, has resulted in its extensive accumulation in terrestrial and aquatic ecosystems (Derraik, 2002). The plastic waste enters the environment through various pathways and has serious detrimental effects on our living environment. This has caused substantial damage to both wildlife (Browne et al., 2008; Uhrin and Schellinger, 2011) and their habitats (Lebreton et al., 2017). Consequently, an increasing attention is now being paid to the impact of plastics on ecosystems and human health (Lithner et al., 2011; Rochman et al., 2013; Law and Thompson, 2014; Law, 2017). The growing interest in this phenomenon has triggered the idea to investigate the possibility of using remote sensing techniques and associated methods to monitor and identify plastic waste in the terrestrial environment.

Optical remote sensing techniques have been developed over the years to investigate the Earth's surface and monitor changes in vegetation, aqueous bodies, and land use (Tong et al., 2019; Karthikeyan et al., 2020; Toure et al., 2019; Chawla et al., 2020). Thereby, several recent studies also demonstrated the potential of these techniques for the detection and monitoring of plastics on land surfaces. Optical remote sensing technologies involve employing field spectrometers, aircraft - and satellite sensors to collect electromagnetic radiation reflected and emitted from the Earth's surface. The collected data are then utilized to perform a processes of detection and classification according to the spectral characteristics of the different types of materials. Conventional approaches to examine land surface materials such as visual inspections, tend to be time-consuming, expensive, and prone to man-made errors (Smith et al., 2021). As far as plastic is concerned,

remote sensing techniques offer a reliable and efficient way to monitor plastics on the land surface on a larger scale. Diverse types of plastics can have different characteristics allowing them to persist for varying periods in the environment (Andrady, 2017). Many of these plastics can be chemically hazardous in certain situations. More than 50% of plastics are intrinsically toxic (Lithner et al., 2011). Even when not toxic, plastics can absorb and bio-accumulate other contaminants (Teuten et al., 2009; Rochman et al., 2013). When plastics are exposed to ambient solar radiation, they slowly decompose into microplastics and release greenhouse gases, including methane and ethylene, which contribute to climate change and global warming effects (Royer et al., 2018; Vishwakarma, 2020). Through the identification of distinct types of plastics on land surfaces, potential environmental impacts can be assessed and adequate measures can be taken to alleviate damages. The detection of various types of plastics further helps determining also their routes and origins. Such information in turn serves for the establishment of strategies to mitigate plastic waste at the source and prevent it from entering the environment. Periodic monitoring and detection of plastic materials for better identification of the sources and pathways of plastic litter and assessment of its accumulation over time is a challenging future obligation. Despite the potential of optical remote sensing technology for plastic litter monitoring, several challenges remain to be overcome to achieve accurate and reliable results.

The main challenges and objectives of plastic detection using optical satellite data are as follows:

- Devise and implement a remote sensing technique for plastic detection: This key aim focuses on an approach that can accurately identify various distinct types of plastic materials on land surfaces.
- Assess the effectiveness of diverse optical remote sensing techniques for plastic detection: Thereby, the efficiency of multispectral and hyperspectral imaging at different spatial resolutions has to be investigated.
- Research the potential of presently operating air-, and spaceborne satellite sensors for plastic detection: This targets potential instruments with different spatial, spectral and temporal designs usable for detecting plastic materials.
- Find the optimum evaluation algorithms for plastic detection: Here diverse methods, primarily machine learning models like decision-tree classifiers, CNN, RF, and SVM need to be tested and examined.
- Test and validate the plastic detection on different background materials: To ensure the efficacy, reliability and transferability of the developed plastic detection approach(es), the developed methods need to be tested and verified at different environmental conditions and land surfaces.
- Find and test possible solutions to automatically add functions to the detected plastic materials: This aims at producing a new database of functionalities for plastic and to test and validate its accuracy.

In summary, the overall objective of plastic detection based on satellite data requires an approach that includes the investigation and assessment of diverse optical techniques,

available instruments, suitable evaluation methods such as machine learning algorithms, testing and validation of results at different environmental conditions and the assignments of functions.

1.3 Research framework, sensor data used and test sites

This chapter serves as an introduction to the research framework and data collection procedures adopted in the study. A multi-spatial and multi-spectral scale approach is used to address the research tasks set. Thereby, unique multi-, and hyperspectral datasets recorded in the laboratory, by air-, and spaceborne, sensors and created by simulation approaches are combined with ground truth data acquired during three field campaigns.

The research framework encompasses a list of laboratory data (Section 1.3.1), the configuration of optical sensors (Section 1.3.2), and an overview of the study area (Section 1.3.3) used throughout the various chapters.

1.3.1 Laboratory data and spectral simulations

1.3.1.1 US public spectral libraries

- USGS spectral library (Kokaly et al., 2017)

  This is a library of spectra compiled using laboratory, field and airborne spectrometers covering a wide range of wavelengths from the ultraviolet to the far infrared (0.2 to 200 μm). It contains reflectance spectra from samples of specific minerals, rocks, and soils as well as of vegetation, microorganisms, and man-made materials, involving PE, PVC, PET, and PA. The category of organic chemical substances is excluded in this study as their molecular structures are similar to plastics, but rarely disperse in nature. In many cases purified samples are used to identify unique spectral features and establish spectro-chemical relationships. These relationships are critical to the interpretation of remote sensing data obtained from a variety of platforms, such as aircraft or spacecraft. The library also contains a mixture of physical constructions and mathematical calculations. Four types of spectrometers were used, including the Beckman™ 5270 (0.2 to 3 μm), the Analytical Spectroscopy Devices (ASD) field portable spectrometer standard, high resolution (hi-res) and high resolution next generation (hi-resNG) models (0. 35 to 2.5 μm), the Nicolet™ Fourier Transform Infrared (FTIR) interferometer spectrometer (1.12 to 216 μm), and the NASA Airborne Visible/Infrared Imaging Spectrometer AVIRIS (0.37 to 2.5 μm). Samples of rocks, soils, and natural mineral mixtures were measured in laboratory and field environments, while different types and species of vegetation plots and plant compositions were also included in the library. For forest vegetation plots, where the field spectrometer cannot reach due to tall trees, measurements are made with an airborne spectrometer.

- ECOSTRESS spectral library (Meerdink et al., 2019)

  ECOSTRESS (Ecosystem Thermal Radiometer Experiment on Space Station) is a NASA mission to study plant health by measuring surface temperature and evapotranspiration from the International Space Station (ISS). As part of this mission, a spectral library has been established to support the interpretation of data collected by the ECOSTRESS instrument. The ECOSTRESS spectral library provides a

Table 1.1: Nominal parameters of optical air-, and spacecraft sensors whose data were used in this thesis

Sensor	IFOV	FOV	Swath	Spectral range	Band no.	Spectral res.
HySpex-VNIR-1600	0.36 mrad	1600 px	-	0.4-0.9	160	5
HySpex-SWIR-320m-e	1.5 mrad	320 px	-	0.9-2.5	256	6
HySpex Mjolnir S-620	0.54 mrad	620 px	-	1.0-2.5	300	5.1
HyMap	2 mrad	512 px	-	0.4-2.5	128	13-17
WorldView-3	1.2/3.7m	-	13.1	0.4-2.4	16	-
Sentinel-2	10/20/60m	-	290	0.4-2.2	13	-
PRISMA	30 m	-	30	0.4-2.5	237	12
GaoFen-5	30 m	-	60	0.4-2.5	330	4.3-7.9

comprehensive collection of natural and artificial laboratory-measured spectra covering the wavelength range of 0.35-15.4 μm. It includes nearly 2,000 spectra of soils, rocks, minerals, meteorites, vegetation, non-photosynthetic vegetation (NPV), water/snow/ice, and man-made materials. There are two roofing rubbers in the man-made category, which are plastic samples. Some samples were purified to better understand the spectral characteristics associated with their chemical structure. The library includes data from laboratory, field and airborne spectrometers. Laboratory instruments used include a Nicolet Fourier Transform Infrared spectrometer and a Thermo Fisher Scientific DXR Raman microscope. Field measurements were collected using an Analytical Spectroscopy Device (ASD) field portable spectrometer and a Gerber Spectral Imaging field spectrometer. Airborne measurements were recorded using the Airborne Visible/Infrared Imaging Spectrometer (AVIRIS) and the Hyperspectral Thermal Emission Spectrometer (HyTES).

1.3.1.2 PlaMAPP in-house spectral library

The PlaMAPP spectral library is an in-house (GFZ) created collection of high-resolution spectra measured in the near infrared and shortwave infrared range (0.97-2.5 μm). It includes five types of household plastics, which cover 95% of the global production namely Comprising Polyethylene (PE), Polypropylene (PP), Polyvinylchloride (PVC), Polyethylene Terephthalate (PET), and Polystyrene (PS), as well as nine types of industrial plastics: ABS, EVAC, PA, PBAT, PC, PMMA, POM, PU, and SAN.

1.3.2 Optical remote sensing sensors

To test and validate the potential of the classifier being developed in this study to identify different types of plastic materials in real-world environments, aircraft - and satellite data from different regions with diverse surface characteristics were used (Fig. 1.1).

The specifications of the sensors are listed in Table 1.1.

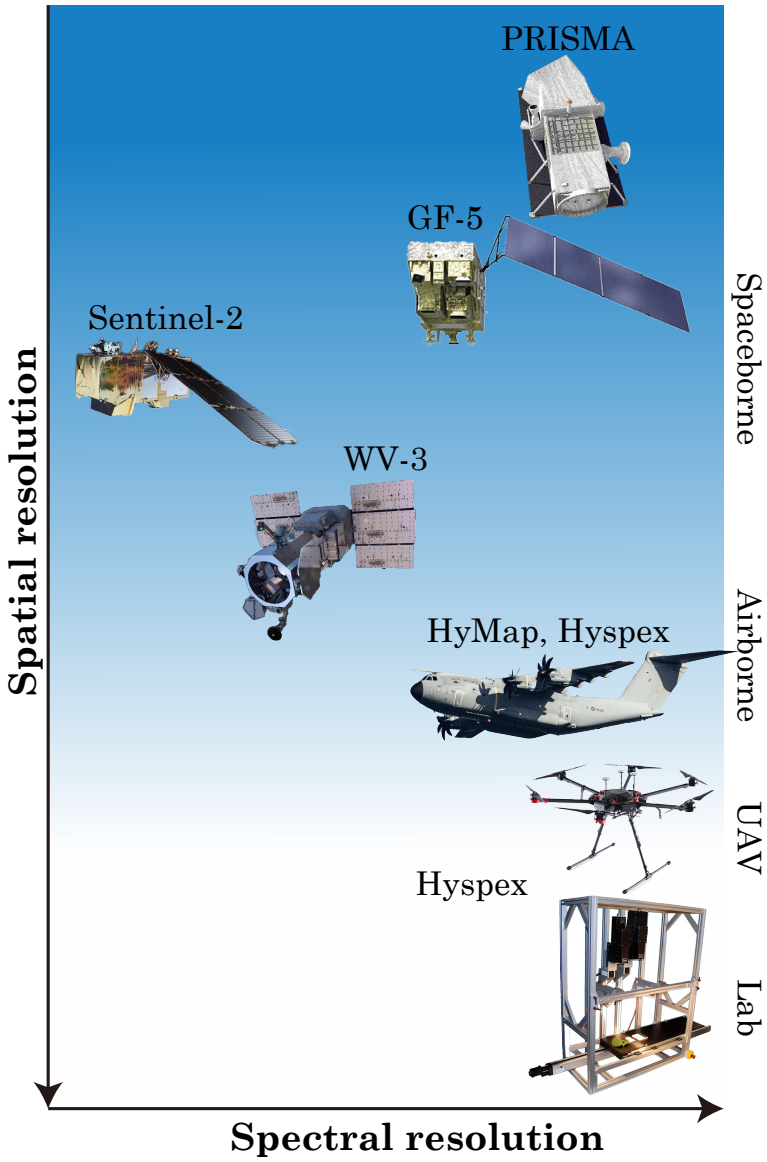

Figure 1.1: Diagram depicting the various scales of data utilized in the thesis and the remote sensing equipment employed.

1.3.2.1 Airborne hyperspectral HySpex/HyMap sensors

In this study, data from three push-broom sensors, namely the HySpex-VNIR-1600, HySpex-SWIR-320m-e, and HySpex Mjolnir S-620 (NEO), and one whisk-broom scanner, the HyMap sensor ((Cocks et al., 1998)) were utilized.

The HySpex airborne system, developed by Norsk Elektro Optikk (NEO), is a highly advanced hyperspectral imaging system consisting of two imaging spectrometers or cameras. These cameras record solar radiance reflected at the Earth's surface in the wavelength range of 400-2500 nm. The first camera, known as VNIR-1600, is designed to work in the visible and near-infrared spectral domain and can record data with 160 channels distributed between 420-990 nm. The second camera, referred to as SWIR-320m-e, can acquire data with 256 channels in the short-wave infrared range of 970-2500 nm. Both cameras employ the push-broom scanning technique or line imaging, which allows a simultaneous recording of the radiation spectrum of all cross-track pixels. Each frame of data collected in this manner corresponds to a specified scan range or field of view, which can be measured in meters or degrees. The instantaneous field of view (IFOV) is the field of view of a single pixel. The final image is formed by merging consecutive frames combined with the steady along-track motion of the camera during aircraft movement. HySpex cameras are typically operated in small single- or twin-engine aircraft, facing the sky floor, at altitudes between 1000 and 2000 meters above ground level. A field-of-view expander is typically employed to double the field of view of each camera, achieving greater range and pixel size at a given flying height. The spatial resolution of the HySpex sensor is 0.5-2 m, depending on the respective flight altitude.

The HySpex Mjolnir S-620 was mounted on a UAV, covering the wavelengths range between 1000 nm and 2500 nm with up to 300 bands at 5.1 nm intervals. It records lines with 620 pixels with an across-track IFOV of 0.54 mrad. It is a hyperspectral imaging system with high-performance for a broad range of applications, from environmental monitoring to geological mapping, agriculture and forestry. The Mjolnir S-620 has a maximum data rate of 100 fps, allowing for rapid and accurate acquisition of data, which makes it ideal for time-sensitive applications, such as catastrophe response or surveillance of fast-moving processes. In addition, the system is designed to be portable and user-friendly, enabling its operation from a laptop or tablet using HySpex's intuitive software. The software provides the user with the ability to configure the camera, capture data and analyze results in real time. The system is also multi-functional as it can be easily mounted on a drone, aircraft or ground vehicle, allowing it to be adapted to different environments and applications.

The HyMap imager is a highly capable hyperspectral sensor that is designed for aircraft operation only. Its imaging system has an IFOV of 2.0 mrad providing 512 pixels in the across-track direction. It captures 128 spectral bands ranging from 0.45-2.48 μm, with intervals of 13-17 nm. The HyMap is typically operated by research institutions, government agencies, and private companies that specialize in remote sensing and earth observation.

The position and attitude of the sensor in 3D space is monitored by a Global Positioning System (GPS)-assisted Inertial Navigation System (INS). The INS is equipped with a DGPS receiver and an inertial measurement unit (IMU), which records lateral acceleration in all spatial dimensions and rotational acceleration around the relevant axis. The synchronization of position and attitude measurements with the image is ensured

by synchronization pulses from the sensor to the INS. The main geometric and spectral characteristics of each sensor described above are summarized in the Table 1.1.

All these hyperspectral sensors provide a powerful tool for the accurate detection and identification of plastic materials in a variety of environments. By utilizing multiple types of sensors with different spectral ranges and spatial resolutions, researchers can obtain comprehensive and detailed data that can help develop effective monitoring and management strategies to mitigate the environmental impacts of plastic products.

1.3.2.2 Spaceborne multispectral Sentinel-2 sensor

Sentinel-2 is a satellite system developed and operated by the European Space Agency (ESA) as part of the Copernicus program to deliver global, high-resolution multispectral images of the Earth's surface. The Sentinel-2 mission consists of two identical satellites, Sentinel-2A and -2B, which were launched in 2015 and 2017. Its advanced sensors, known as MultiSpectral Instruments (MSIs), are designed to capture images at a swath of 290 km and a spatial resolution of 10, 20, or 60 meters, depending on the respective spectral band. An MSI sensor is composed of two independent optical modules that operate together to capture the imagery. One covers the Visible and Near-Infrared (VNIR) wavelengths, encompassing the spectral range from 400 to 1000 nm, at a Ground Sampling Distance (GSD) of 10 or 20 meters. The second module operates in the Shortwave Infrared (SWIR) range that covers the wavelengths from 1000 to 2500 nm at a GSD of 20 or 60 meters.

There are 13 spectral bands provided by the MSI sensor, including four in the VNIR range (blue, green, red, and near-infrared) and nine bands in the SWIR range (including water vapor, cirrus clouds, and various other bands useful for land and vegetation monitoring). The two Sentinel-2 satellites circle the Earth in a sun-synchronous orbit phased at 180 degrees to each other, allowing for a repeat rate of 5 days. A high-speed data delivery system is used on these satellites, offering a rapid transmission of data to ground stations for processing and fast dissemination to the end users.

1.3.2.3 Spaceborne superspectral WorldView-3 sensor

The WorldView-3 (WV-3) satellite is a commercial system with a very high spatial resolution, also operating in a sun-synchronous orbit. Its sensor records data with relatively small and well placed spectral bands in the VNIR and SWIR range. In the VNIR range, it provides four standard color bands along with four additional bands designed for specific tasks - coastal, yellow, red edge, and near-IR2. A detailed configuration of the spectral bands is given in Table 3. The major advance of the WV-3 system is the inclusion of eight well placed SWIR bands in the 1195-2365 nm atmospheric window that allow an improved detection and partly identification of minerals and man-made materials as compared to the limitations of operating multispectral sensors in this wavelength region. Additionally, twelve so-called CAVIS bands (Clouds, Aerosols, Vapors, Ice, and Snow) ensure accurate estimates of aerosols and water vapor for atmospheric compensation of the data. The satellite operates at an altitude of 617 km and provides a GSD of 0.31 m for the panchromatic band, 1.24 m for the VNIR bands, 3.7 m for the SWIR bands, and 30 m for the CAVIS bands at nadir. The swath width of the instrument is 13.1 km, and it has a descending node at 10:30 a.m. Thanks to the fast-reacting "Control Moment Gyros" (CMGs) onboard, the revisit time for off-nadir images is less than a day. All data

provided by this system are already geo-corrected, making it easy to use for a range of applications.

1.3.2.4 Spaceborne hyperspectral GaoFen/Prisma sensors

- GaoFen-5

  The Chinese meteorological satellite GaoFen-5 (GF-5) was launched in May 2018, to a sun-synchronous orbit at an altitude of 705 km. Its main sensor, the Advanced Hyperspectral Imager (AHSI), is designed to capture hyperspectral data with a very high spectral resolution at a GSD of 30 m. It operates in the VNIR-SWIR spectral range, with a spectral configuration consisting of 256 bands in the 0.4-2.5 μm range and 128 bands in the 2.5-3.95 μm range. The spectral sampling interval is approximately 5 nm in the VNIR-SWIR range, enabling detailed analysis of the spectral characteristics of various targets on the Earth's surface. The AHSI sensor has a swath width of 56 km, which allows for a moderate large-scale data collection at a moderate repetition rate. The ground processor delivers level 1 (L1) radiance products that include radiometric corrections and system geocoding (https://www.cheosgrid.org.cn/index.htm). The satellite stopped operating in 2020 but a second generation of the GF-5 was already launched in September 2021.

- PRISMA

  PRISMA is a free flyer satellite launched by the Italian Space Agency (ASI) in 2019 (Cogliati et al., 2021). It also operates in a sun-synchronous low Earth orbit at an altitude of 615 km. It is designed to capture high-resolution spectral data in the VNIR-SWIR spectral range at a GSD of 30 m. The spectral configuration of PRISMA provides 223 spectral bands ranging from 0.4-2.5 μm with a spectral sampling interval of 5.8 nm. This high spectral resolution allows for detailed analysis of the spectral characteristics of various targets on the Earth's surface, foremost minerals, rocks and soils as well as man-made materials. The sensor has a swath width of 30 km, which enables moderate small-scale data collection at a low repetition rate. PRISMA's ground processor produces a number of standard products, which are made available to users. Details are available in the PRISMA Products Specification Document (ASI, 2020). With their advanced hyperspectral capabilities, PRISMA, as well as GaoFen-5 represent systems that allow the diagnostic detection and identification of numerous surface materials in a unique way.

1.3.3 Study areas

In order to assess the feasibility for identifying various plastic materials in real-world environments under different conditions, multiple regions with diverse surface characteristics were recorded using aircraft and satellite data (Table 1.2, Figure 1.2).

1.3.3.1 Sites recorded by airborne sensors incl. ground-truth data

To conduct the study, data were collected from the following regions. Three sites were selected in Germany, one each in Spain, Ghana and Egypt and one in China, each characterized by a different landscape. The study areas recorded by aircraft include an urban

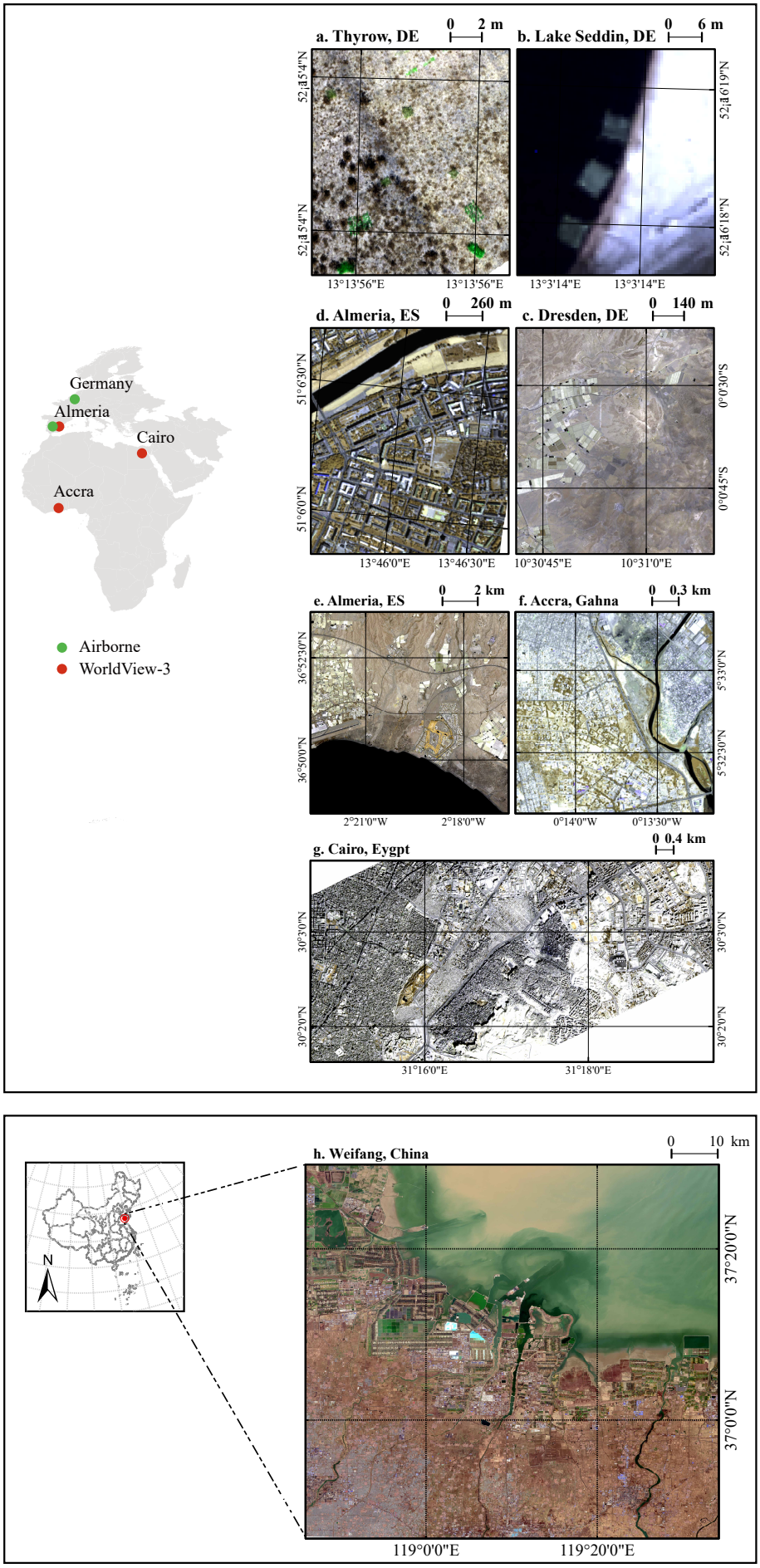

Figure 1.2: Sketch map and detailed coordinates of the study areas

Table 1.2: Study areas and respective data recordings.

Location	Sensor	Date	GSD
Thyrow, DE	Mjolnir S-620	Jun, 13, 2019	3 cm
Lake Seddin, DE	VNIR-1600/ SWIR-320m-e	Feb. 16, 2015	40 cm
Dresden, DE	HyMap	Jul. 07, 2004	4 m
Almeria, ES	HyMap	Jun, 15, 2005	5 m
Almeria, ES	WorldView-3	Jun. 26, 2018	3.7 m
Accra, AF	WorldView-3	Mar. 03, 2018	3.7 m
Cairo, EG	WorldView-3	Jan. 29, 2019	3.7 m
Weifang, CN	Sentinel-2	Dec. 02, 2021	10 m
Weifang, CN	PRISMA	Dec. 21, 2019	30 m
		Nov. 27, 2021	
Weifang, CN	GaoFen-5	Nov. 14, 2019	30 m

landscape in Dresden, Germany, a grassland-dominated area in Thyrow, Germany, a location at Lake Seddin, Germany, and an area with bare soils and greenhouse agriculture in Almeria, Spain. To ensure the validity of the data, plastic targets visible in the airborne datasets were not included in the spectral libraries used for the development of the classifier.

In the grassland-dominated area in Thyrow, Germany, the HySpex Mjolnir S-620 imager mounted on a UAV was used to record the data. The authors placed well-defined and spectrally measured materials on the ground, including transparent PET plastic bottles of different sizes and large foils made of PBAT, PET, and PE plastic. The geometric postprocessing was conducted using the PARGE software, and the atmospheric correction was done in-house using the SICOR software. The data of the Lake Seddin, Germany were recorded by combined HySpex VNIR-1600 and SWIR-320m-e sensors aboard an airplane. Three arrays of white and opaque PS foam boards and one blue PE tarpaulin were set up over the shallow lake water and on its sandy bank.

The urban landscape in Dresden, Germany, was recorded by the HyMap system from an aircraft. Ground control of locations covered by distinct plastic materials was maintained through fieldwork using portable spectrometers and GPS equipment. Among a total of more than 40 different urban materials, four plastic materials (PE, PET, PP and PVC) were identified and mapped based on hyperspectral ground measurements.

In the area with bare soils and greenhouse agriculture in Almeria, Spain, the HyMap system onboard an airplane was used to record the data. The study area was dominated by PE plastic sheds utilized as greenhouses for agricultural purposes. Similar to the Dresden dataset, the ground control was conducted by field measurements with portable spectrometers and GPS. However, due to the lack of diversity of plastics, only greenhouses made from PE were collected for the ground truth map with more than 10,000 pixels. All the datasets were available as level 2 products, passing radiometric corrections, atmospheric corrections, and ortho-rectification.

1.3.3.2 Sites recorded by spaceborne sensors

Investigated targets recorded by satellite sensors lie in different regions of the world - in Almeria, Spain; Accra, Ghana; Cairo, Egypt; and Weifang City, China.

- Almeria, Spain

  The city of Almeria, located in the southeastern part of Spain, is known for its vast agricultural lands and greenhouses that produce tons of fruits and vegetables. The plastic greenhouses, mostly made of polyethylene (PE), cover a significant portion of the area's cropland and are essential for the local economy. However, the high usage of plastic in the region has also led to significant plastic waste generation, with over 30,000 tons produced every year. The plastic waste problem in Almeria is particularly severe, as the discarded plastic often ends up in the Mediterranean Ocean, affecting marine life. The abandoned greenhouses, after shredding, are a significant contributor to the plastic waste problem, as it is not adequately managed, leading to its accumulation in the environment.

- The city of Accra, Ghana, West Africa, capital of Ghana, is home to one of the largest electronic waste dump sites in the world - Agbogbloshie. The site is the destination for more than 150,000 tons of electronic waste shipped from around the world every year. Electronic waste is often dismantled in unsafe and unregulated conditions, leading to environmental contamination and health risks for the workers and the local population. Electronic waste contains significant amounts of plastic, which accounts for up to 20% of the waste stream. However, only 15% of electronic waste is recycled, leading to the accumulation of plastic waste in the environment. Moreover, the urban areas of Accra generate around 760,000 tons of municipal solid waste every year, leading to further plastic waste generation.

- The city of Cairo, Egypt, capital of Egypt, is home to one of the world's most extensive informal waste management systems. The Zabbaleen community, which has been living in Cairo since the 1940s, collects and sorts the city's waste, recycling around 80% of it. The Zabbaleen community lives in impoverished conditions, often among the sorted waste and their livestock. The plastic waste generated in Cairo, estimated at around 9,000 tons per day, is a significant contributor to the environmental problems of the city. However, the Zabbaleen community's waste management system has been successful in recycling and reusing plastic waste, reducing its amount that usually ends up in the environment.

- Weifang City, Shandong Province, China is known for its thriving agriculture, with plastic greenhouses covering around 20% of the city's cropland. The municipality has invested in green energy, followed by an increased installation of photovoltaic panels. These are made of different plastic materials such as PP, PE, and EVA. Furthermore, huge sheets of plastic covers are used on any construction site in this area to avoid the denudation of soils. The growing industrial activity in the region leads to additional and higher consumption of plastic products. Coupled with an inadequate waste management system, this fosters also the accumulation of plastic waste in the environment.

2 Theoretical background

Optical Remote Sensing involves the recording of radiation reflected and emitted by observed surfaces within a specific range of wavelengths in the electromagnetic spectrum. This range extends from the visible spectrum, that starts at 0.4 micrometers, reaching to the near infrared (NIR) and ends at the thermal infrared (TIR) region, at about 15 micrometers.

2.1 Principles of spectroscopy

When radiation interacts with matter, several processes occur, including reflection, scattering, absorption, fluorescence/phosphorescence (absorption and re-emission), and photochemical reactions (absorption and bond breaking). As light is a form of energy, the absorption of light by matter causes an increase in the energy content of the molecules (or atoms) within the material. The total potential energy of a molecule is represented by the sum of its electronic energy, vibrational energy, and rotational energy:

$$E_{total} = E_{electronic} + E_{vibrational} + E_{rotational} \tag{2.1}$$

The energy that a molecule possesses in each form is not a continuous range, but rather a series of discrete levels or states. The differences in energy between different states are arranged in the following order: electronic state >vibrational state >rotational state.

In some molecules and atoms, the photons of incoming UV and visible light have enough energy to cause transitions between different electronic energy levels. The wavelength of the absorbed light has the energy required to move electrons from lower energy levels to higher energy levels. The energy associated with electromagnetic radiation is defined as:

$$E = h\nu = \frac{hc}{\lambda} \tag{2.2}$$

where:

E is the energy (in Joules),
h is Planck's constant (6.62×10^{-34} Js),
ν is the frequency of light (in s^{-1}), c is the speed of light in (m/s),
and λ is the wavelength of the light in (m^{-1}).

Spectroscopy studies how matter interacts with or emits electromagnetic radiation. There are different types of spectroscopy, depending on the wavelength range being measured. Rotational spectroscopy is associated with the far infrared to microwave region, vibrational spectroscopy with the near infrared and short wave infrared regions, while electronic spectroscopy belongs to the ultraviolet, visible, and near infrared regions (Fig. 2.1). It should be noted that these divisions are not strictly defined.

The main components of plastics include polymerization units and additives such as flame retardants and plasticizers, all primarily composed of carbon, hydrogen, oxygen and

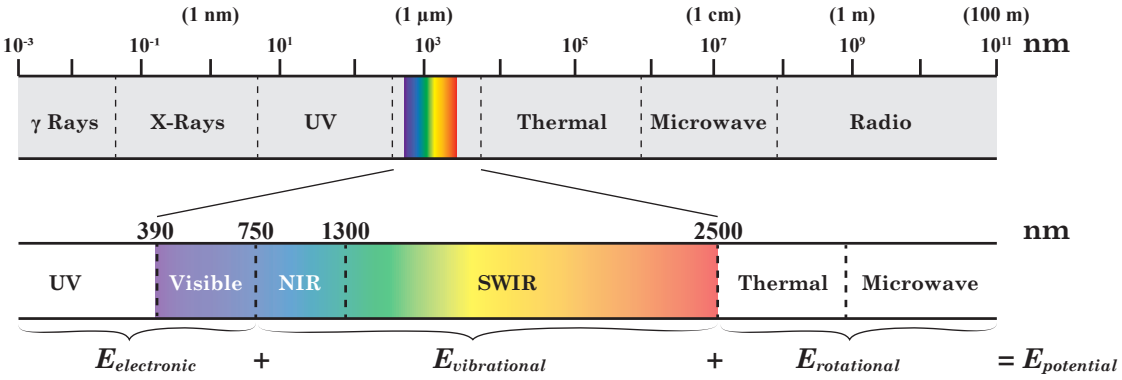

Figure 2.1: The electromagnetic spectrum, showing the regions of interest in the context of the visible/infrared reflectance spectroscopy, namely the visible region (390 to 750 nm), the near infrared (NIR; 750 to 1300 nm) and the short-wave infrared (SWIR, 1300 to 2500 nm).

nitrogen. They are petroleum derivatives with the backbone of C-H chains and distinctive functional groups. Thus, the dominant diagnostic bands arise from the fundamental vibrations of the corresponding sub-molecular groups, as well as their overtones and combination bands (Eisenreich and Rohe, 2006). There are further absorption features displayed in the visible range (400-780 nm). However, most of these correspond to electronic transitions between pigment molecules and are excluded from the identification process for this reason. Therefore, most diagnostic spectroscopic features corresponds to molecular vibrational transitions located in the NIR and SWIR wavelengths and are primarily explored in this study.

The interpretation of vibrational features assumes the molecules to be oscillators, excited by the absorption of infrared radiation. These molecular vibrations can be described by the classical physics model of a harmonic diatomic oscillator vibration system. Two vibrating masses are joined by a spring with a given force constant, leading to a change in the intra-nuclear distance. Combining Hooke's law with Newton's law of force, the vibrational frequencies ν of an oscillator which consists of two atoms of masses m_1 and m_2 are derived from a force constant k and the reduced mass μ:

$$\nu = \frac{1}{2\pi}\sqrt{\frac{k}{\mu}}, \quad \mu = \frac{m_1 m_2}{m_1 + m_2} \tag{2.3}$$

Following a quantum mechanical description, the harmonic oscillator's vibrational energy is not continuous, but rather exists as specific, discrete energy levels. The energy levels of the oscillator are distinguished by the quantum number n:

$$E_{vib} = h\nu\left(n + \frac{1}{2}\right) = h\left(n + \frac{1}{2}\right)\frac{1}{2\pi}\sqrt{\frac{f}{\mu}}, \quad n = 0, 1, 2, ... \tag{2.4}$$

The masses (m1) and (m2) correspond to the atoms involved in the molecular structure, while the force constant (f) is dictated by the chemical bond between them. As presented in Eq. 2.3 and 2.4, the relationships clarify how the unique combination of atoms lead to distinguishable absorption spectra of different molecules.

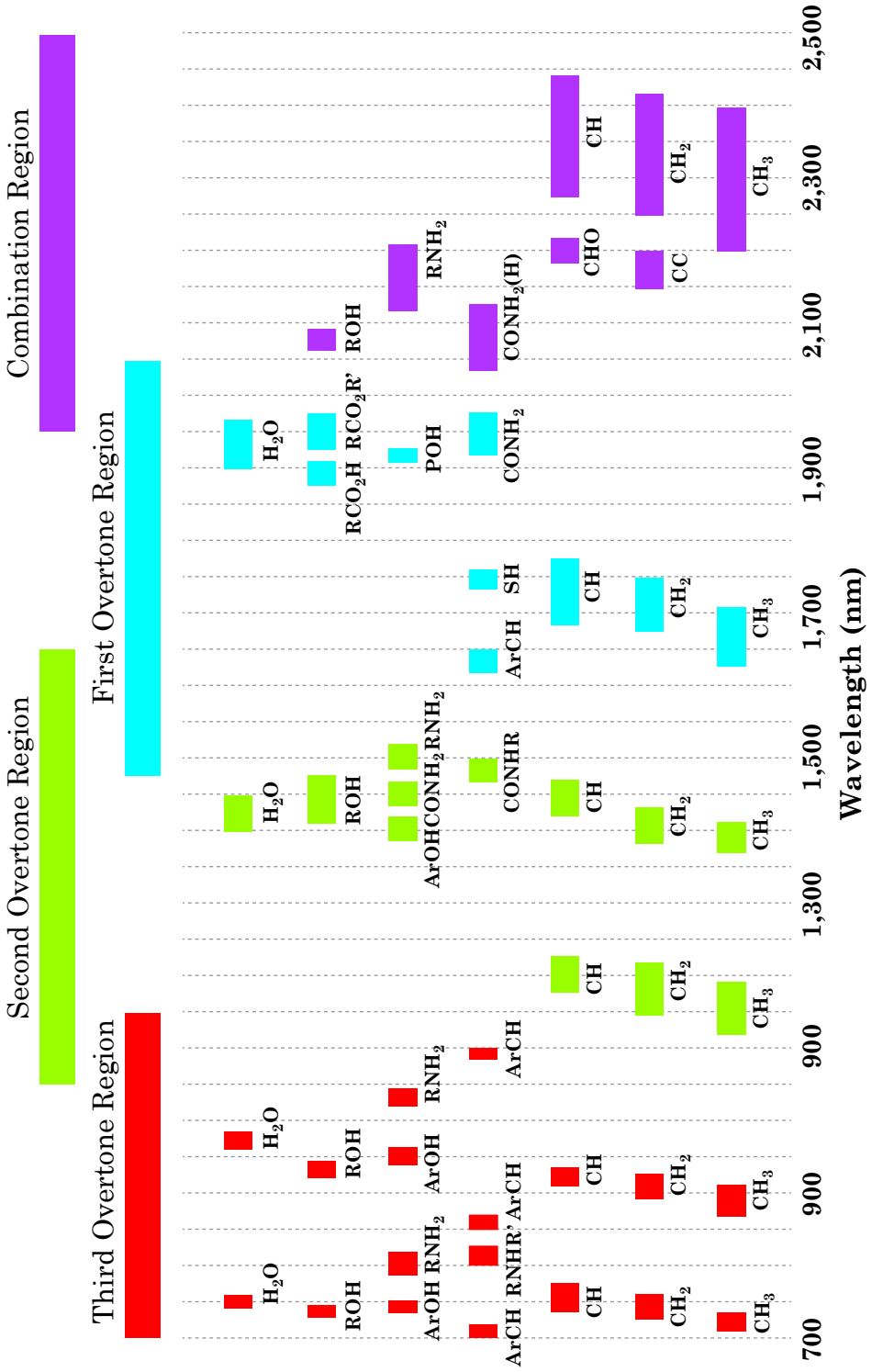

Figure 2.2: Major analytical bands and relative peak positions for prominent near-infrared absorptions. Source: Metrohm Monograph 8.108.5026EN - A guide to near-infrared spectroscopic analysis of industrial manufacturing processes. Metrohm AG, CH-9101 Herisau, Switzerland.

The vibrational quantum number can only have integer values. Only transitions between adjacent and equidistant energy levels are allowed in harmonic oscillators. The Boltzmann distribution governs the distribution of molecules among allowed vibrational levels. At room temperature, the majority of molecules occupy the ground vibrational level (n=0), making the fundamental transition to the first allowed vibrational level (n=1) the dominant spectral feature. The further allowed transitions are much weaker, deriving from vibrationally excited levels and the associated bands. The absorption of photons depends on whether the frequency of the photon is comparable to the energy gap between the two vibrational states of the bond. But that's not all that is required for energy absorption. The absorption and emission of photons by real molecules is a more intricate process. Complex molecules, particularly those containing long polymeric chains like the plastic examined in this study, are recognized as having a system of coupled oscillators. The precise calculation of absorption bands necessitates a complex mathematical approach, taking into consideration various factors, including:

- Resonance theory posits that a means must be established for efficiently transferring energy to molecules. In the case of molecular vibrations, this transfer occurs via molecular polarity, wherein the interaction of infrared radiation with the vibrating molecule only transpires when the vibration is accompanied by a change in the dipole moment. The extent to which this dipole moment varies during the vibrational shift largely determines the intensity of light absorption. Vibrational-spectral transitions between photons of light and molecular vibrations are only observed in heteronuclear diatomic molecules. As the lightest atom, hydrogen exhibits the largest vibrations in bonds (C-H, N-H, O-H, and S-H), these overtones and combinations are assigned bands as shown in Fig. 2.2. Most molecules possess more than two atoms, with each bond being capable of undergoing more than one vibration (stretching, bending). Additionally, not all bonds vibrate independently, and many true vibrations are coupled.

- The vibrational mode of a real molecule is anharmonic and its energy levels structures change with respect to Eq. 2.4 and allow switching between different vibrational modes. When anharmonicity is taken into account, the vibrational energy levels are no longer equally spaced and the energy difference becomes smaller with increasing quantum number n, which can be expressed by Eq. 2.5:

$$E'_{vib} = h\nu \left(n + \frac{1}{2}\right) - y \left(n + \frac{1}{2}\right) \tag{2.5}$$

  where y is the anharmonicity constant.

  Molecular oscillators exhibit inharmonic characteristics that give rise to the emergence of overtones and combinatorial bands. These features arise when the energy of an absorbed photon is utilized for two or more quanta of the same normal mode or split into two or more distinct normal modes of excitation. However, the absorption rates of overtones and combined vibrations are still substantially lower than those of fundamental vibrations.

Infrared spectra contain overtone transitions, which are multiples of the fundamental vibrational frequency and correspond to quantum numbers greater than one. These transitions can be observed between 780 and 2000 nm. However, overtone transitions are much

less likely than the fundamental vibrational frequency, which results in weaker bands. Polyatomic molecules can exhibit combination modes, where multiple vibrational modes interact. These modes are the sum of multiples of each interacting frequency and can be observed between 1900 and 2500 nm. Another factor that affects the infrared (IR) spectra is the non equidistant energy states of a vibration. This means that allowed transitions become smaller in energy, leading to weaker absorption bands.

2.2 Spectra of plastics in the NIR and SWIR wavelength range

The constituents of plastic materials, including macromolecular polymers, fillers, plasticizers, and significant additives like flame retardants, have been mentioned earlier. Furthermore, engineering plastics comprise of fiber-reinforced composites and polymeric resins, which are mainly composed of organic components containing C, H, O, and N.

The interpretation of complex molecules' spectra is based on the concept of group frequencies, which assumes that submolecular atom groups are weakly coupled to other submolecular groups. The absorption bands of these groups are referred to as eigenbands because they always occur at the same wavelength position and are slightly altered by weak interactions with neighboring groups. The unique bands of a single molecule are referred to as "fingerprint" bands. Plastics are composed of repeating units subjected to polymerization. Owing to their relatively uncomplicated molecular structure, their absorption properties in the IR range are easier to interpret than those of natural organic materials. CH, CH2 and CH3 groups are the most important functional groups that contribute to the vibrations which are induced by fundamental modes of motion between C and H atoms, including stretching, in-plane deformation, out-of-plane deformation, wagging, twisting and rocking (Eisenreich and Rohe, 2006).

In the Near-Infrared (NIR) and SWIR range, which are our main focus in this study, the diagnostic absorption features (Fig. 2.2) displayed by plastics are mainly controlled by the stretching vibration overtones and combination modes of C=O, C-C, and by hydrogen-containing functional groups (X-H) (Schwanninger et al., 2011). This is evident from Eq. 2.3, which shows that bands involving low weight atoms appear at shorter wavelengths in the IR spectrum. By summing up the wavenumbers of the fundamental modes involved, an approximate determination of the wavenumbers of the combination bands and overtones can be assigned. Fig. 2.3 and Fig. 2.5 show the chemical formula of the molecular structure and qualitative reflectance spectra of the polymer unit of various plastic materials that are studied in this thesis, respectively. The general absorption characteristics of C-H bonds in plastics can be understood in terms of their mode assignments (Beć and Huck, 2019), including the 1^{st} and 2^{nd} orders of the overtone stretching modes (2ν: 1600-1800 nm, 3ν: 1100-1250 nm) and the combination modes ($1\nu_{Comb}$: 2150-2500 nm, $2\nu_{Comb}$: 1300-1450 nm). The 2^{nd} order of the combination mode is not contemplated in this study as it is masked by the overlay of the 1^{st} overtone of water (O-H) emerging at 1400 nm 2.2. The spectra of all plastic materials show a stepped shape with the inflection points in the first overtone and combination bands. This is caused by a gradual decrease in absorption toward higher order overtones and combination tones (Zhou et al., 2021).

In the polymer units of each plastic type (Fig. 2.3), C-H bonds are linked to other functional groups that have different masses and bonding constants. As described in the previous section, the vibrational frequencies activated by C-H bonds do not fall in the

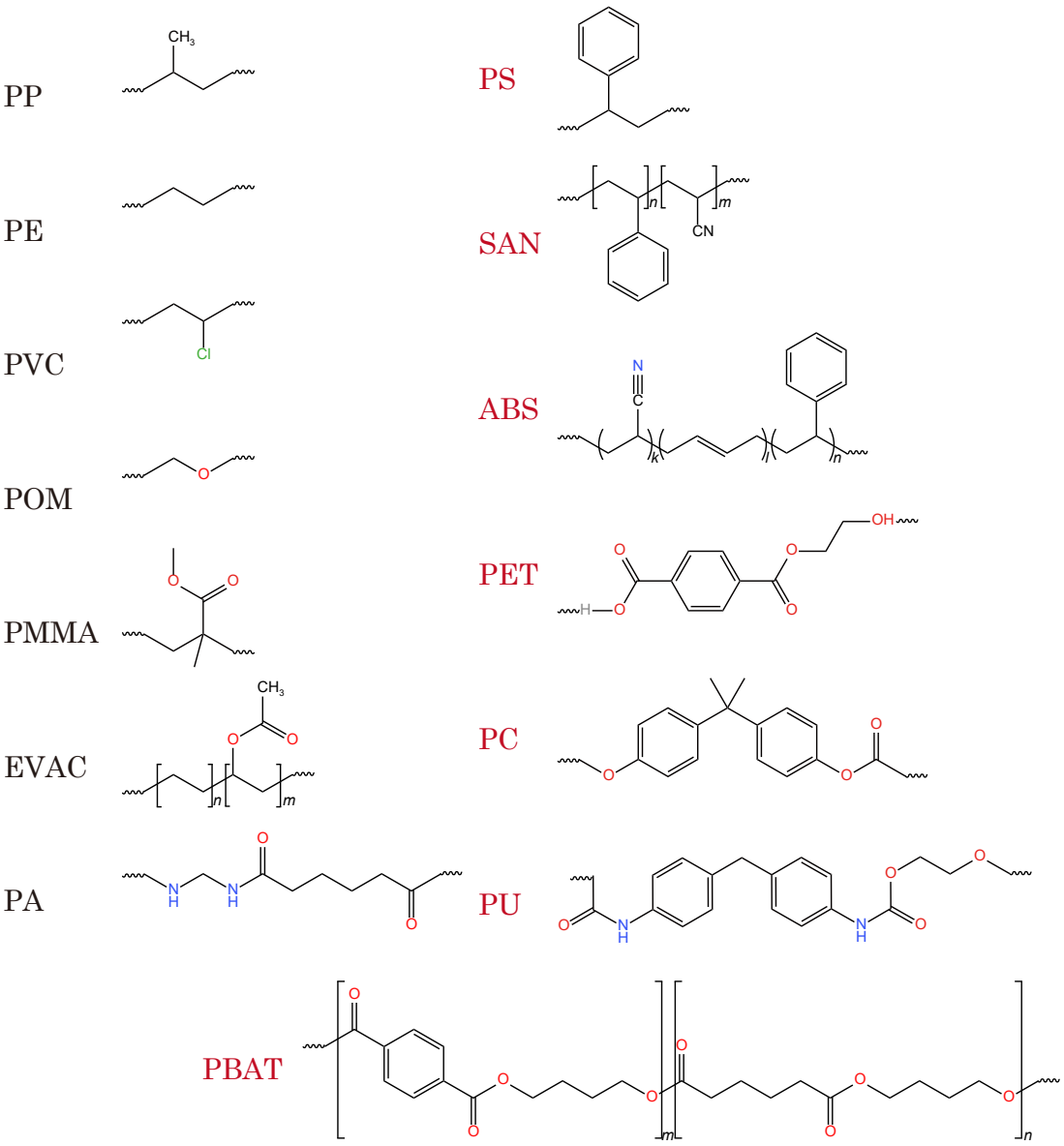

Figure 2.3: Skeletal formula of the unit structures of the investigated plastic materials

same spectral band in all plastics due to the presence of inharmonic and Fermi resonances (Eisenreich and Rohe, 2006). These spectral features offer the possibility to identify and distinguish different types of plastics based on their well-defined spectral absorption characteristics ((Czarnecki et al., 2015; Beć et al., 2018)).

Ma et al. (2019b) found that *sp* hybridization of the CC bonds affects the absorption diversity of materials containing C-H bonds. This entanglement occurs between the s and p orbitals of the outermost shell of the atom (Fig. 2.4).

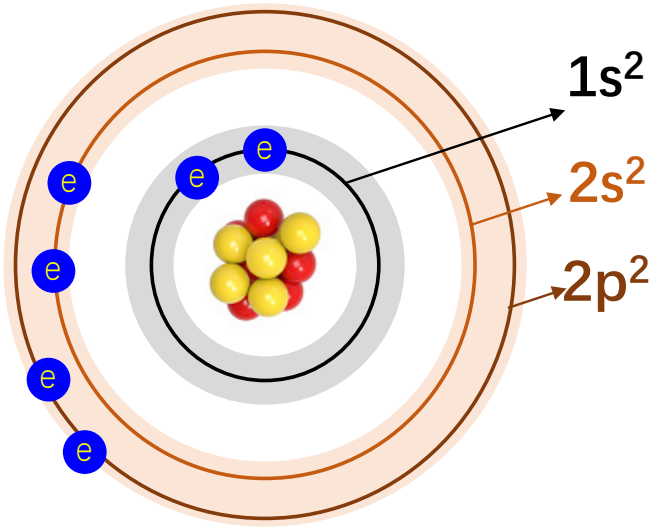

Figure 2.4: Microstructure of carbon atoms

Based on this property, plastic materials can be divided into two main groups based on their molecular structure shown in Fig. 2.3: aromatic polymers containing benzene rings (sp2 hybridization, plastic types marked in red) and aliphatic polymers without benzene rings (sp3 hybridization, plastic types marked in black). Sp2 hybridization's stronger bonding constants lead to higher absorption frequencies than sp3 hybridization (Ma et al., 2019b). As shown in the Fig. 2.5, plastics without benzene rings have a second overtone absorption around 1210 nm and a first overtone absorption at 1730 nm. While plastics with benzene rings exhibit higher absorption frequencies in the second overtone range around 1140 nm, and their first overtone absorption shows a "blue shift" to around 1660 nm. Aliphatic plastics exhibit strong absorption properties in the combined mode range around 2300 nm, due to the combined mode of C-H stretching and bending vibrations. Aromatic plastics also exhibit a broad absorption region in the combined mode associated with C-H and C-C stretching vibrations at about 2130 nm. In the near-infrared band, apart from the C-H bond, another chemical bond that can elicit noticeable absorption is the N-H bond. Its first overtone is located at about 1.5 μm which explains the absorption feature of Polyurethane (PU) and Polyamide (PA) here.

Overall, the spectral range of the first overtone and combined bands exhibit significant differences among various plastics. Accurately evaluating their relevant absorption properties allows for effective differentiation. This provides a dependable foundation for the classification of plastics based on optical remote sensing.

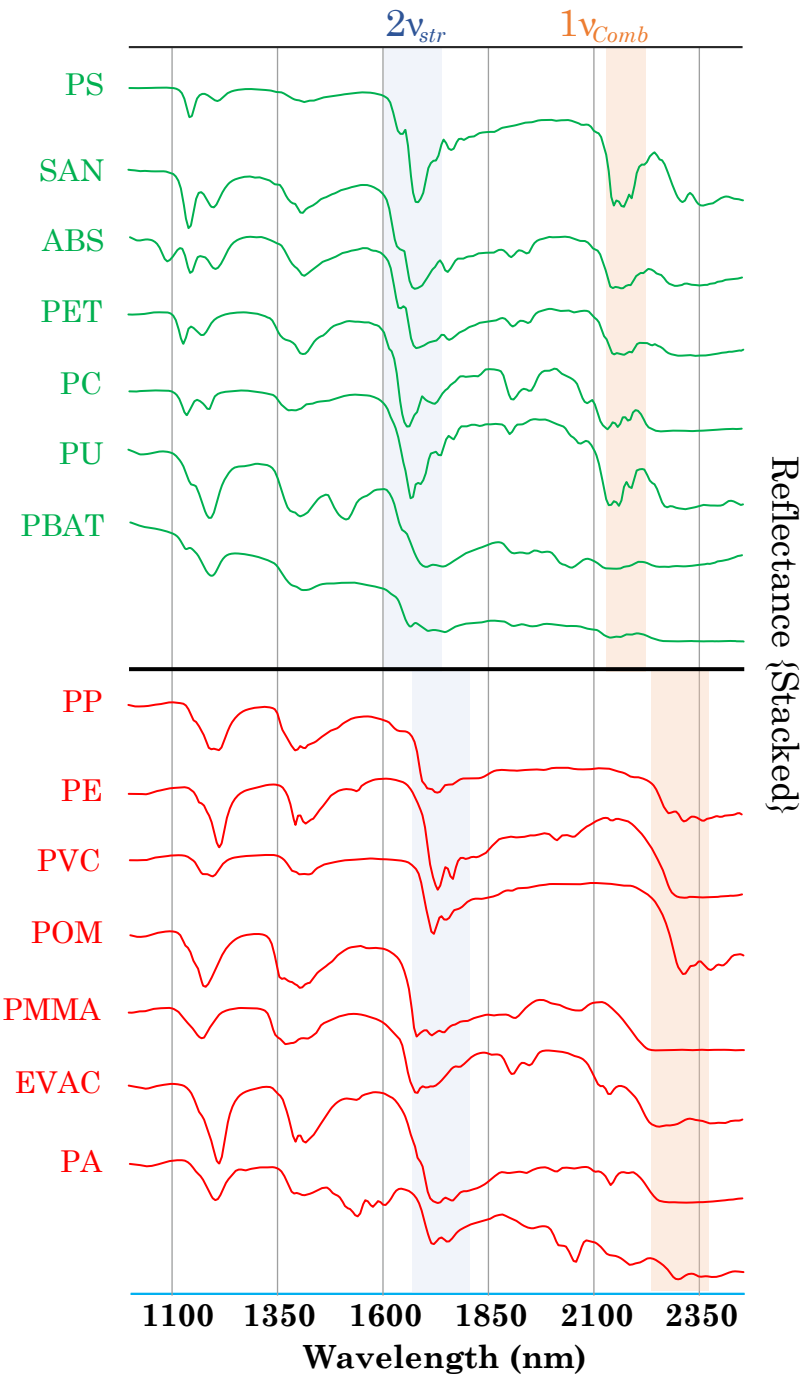

Figure 2.5: Stacked plot of laboratory-derived reflectance spectra (1 nm res.) of various plastic materials investigated in this study.

2.3 Plastic detection using optical remote sensing

As outlined in the previous chapter, the distinct optical properties of various plastic types in the NIR to SWIR range enable automatic sorting by the recycling industry (Huth-Fehre et al., 1995; Masoumi et al., 2012; Moroni et al., 2015). The advancement and refinement of SWIR imaging methods, which offer moderate to high temporal, spectral, and spatial resolution, make remotely sensed data a potential tool for mapping plastic presence in the environment both qualitatively and quantitatively (Moller et al., 2016).

Remote sensing technology has become an important tool in mapping and quantifying marine and coastal plastic litter, which poses a significant threat to the marine ecosystem and coastal communities. Various remote sensing data, including NIR, SWIR, and Thermal Infrared (TIR), have been utilized to identify and quantify plastic debris in the marine environment. Recent studies have demonstrated the effectiveness of remote sensing techniques in identifying and mapping plastic debris in coastal and offshore waters. For instance, Moy et al. (2018) utilized aerial imagery to map marine macro-debris across the main Hawaiian Islands, while Acuña-Ruz et al. (2018) introduces an innovative approach that combines laboratory characterization of AMD hyperspectral data with digital supervised classification in high-resolution imagery, ultimately improving the accuracy of macroplastic identification.

Garaba et al. (2018) demonstrated the potential of airborne SWIR imagery for identifying and quantifying ocean plastics, revealing unique SWIR spectral features common to plastics that can be used to detect them remotely, and Goddijn-Murphy and Williamson (2019) proved that using thermal infrared sensing technology for monitoring marine plastic litter is a promising approach based on radiative transfer theory, and is more effective in areas with air-sea temperature differences, while Fallati et al. (2019) and Veettil et al. (2022) used Unmanned Aerial Vehicle (UAV) to detect plastic debris along the beaches of the Republic of Maldives. Themistocleous et al. (2020) utilized various indices and proved the feasibility of detecting floating plastic using Sentinel-2 data. Recently, Kremezi et al. (2022) investigates fusing WorldView-2/3 images using state-of-the-art methods to detect small marine debris and finds VNIR and SWIR bands essential for detection. The use of remote sensing technology has shown great potential in mapping and quantifying marine and coastal plastic litter ((Martínez-Vicente et al., 2019; Biermann et al., 2020; El Mahrad et al., 2020; Topouzelis et al., 2020).

Although most plastic waste ends up in the ocean through various pathways, the source of marine plastic waste was found to be about 80% on land and 20% directly in the ocean (Li et al., 2016). Therefore, regular global monitoring of land-based plastic is becoming increasingly important in order to prevent further pollution. However, most studies focused on the differentiation of various plastic types by laboratory measurements and near real-time algorithms that can classify plastic waste harvested on automated conveyors using infrared spectroscopy (Yan and Siesler, 2018; Rani et al., 2019; Cruz Sanchez et al., 2020). Only a few studies have focused on detecting and identifying plastics on land, mostly based on hyperspectral imagers on board aircraft (Hörig et al., 2001; Kühn et al., 2004; Heiden et al., 2007). But airborne sensors are limited in terms of covering larger areas. Some researchers have used statistical classification algorithms based on multispectral data recorded by the Landsat-8 Operational Land Imager (OLI) sensor (Lanorte et al., 2017; Aguilar et al., 2020) or Sentinel-2 MSI system (Sun et al., 2021) to investigate the detection of plastic greenhouses. Others have used SUperspectral images recorded by

the spatially high-resolution Worldview-3 satellite sensor (GSD of SWIR bands is 3.7 m) and proposed a class index-based approach for plastic detection, where a "Superspectral" instrument like the DigitalGlobe WorldView-3 system is a trade-off between spectral and spatial resolution suitable solution. Asadzadeh and de Souza Filho (2016) have investigated WV-3 data to delineate the potential for detecting hydrocarbon materials based on simulated images. They further demonstrated that the data is capable of unambiguously detecting HCs in different background soils. Several researchers have proposed knowledge-based indices such as HI (Kühn et al., 2004), RBD (Asadzadeh and de Souza Filho, 2016) and NDPI, which can be used as single-class classifiers by imposing a threshold on the index value, where NDPI has been shown to have superior performance (Guo and Li, 2020). The index can innovatively highlight most plastics by amplifying the significant downward trend of most plastics from 1570 to 1730 nm and 2165 to 2330 nm, however, it does not cover all plastic types. However, these studies rarely provide a reliable identification of different plastic materials, although this is a major challenge in this regard.

Multispectral and hyperspectral satellite sensors offer a limited number of bands to distinguish each single plastic type. Recently, the development and application of hyperspectral satellite sensors has taken another step forward in this regard. For example, the Chinese meteorological satellite Gaofen-5 (GF-5) was launched in 2018 and provides data in the same wavelength range and spectral resolution as Hyperion, but with a 60 km scan range (Liu et al., 2019). A second GF-5 system with the same specifications was launched in September 2021. Another hyperspectral system, PRecursore IperSpettrale della Missione Applicativa (PRISMA), (Cogliati et al., 2021) was launched by the Italian Space Agency in 2019. It carries a hyperspectral imager covering the same wavelength range with a spectral resolution similar to that of Gaofen-5, providing a swath width of 30 km, and an additional panchromatic camera providing a spatial resolution of 5 m x 5 m. A further candidate to deliver hyperspectral data from space is the German Environmental Mapping and Analysis Program (EnMAP), launched on April 1, 2022, with technical specifications comparable to PRISMA (Guanter et al., 2015).

Future instruments providing hyperspectral data from space are the Surface Biology and Geology (SBG) system in the United States (Cawse-Nicholson et al., 2021), the European Space Agency (ESA) built Copernicus Hyperspectral Imaging Mission for the Environment (CHIME) (Rast et al., 2019), and the Space Hyperspectral Applications Land and Ocean Mission (SHALOM) proposed by Israel/Italy (Feingersh and Dor, 2015), with varying technical specifications. The increasing availability of recent hyperspectral satellite data offers the potential to discriminate plastic targets in multiple spatial and temporal modes over a larger range and to identify more types of plastics due to their sensitivity to subtle changes in plastic absorption characteristics, especially in the SWIR wavelength range. The major drawback is that hyperspectral recordings from space presently suffer from a low GSD $\geq$ 30 m due to the small band width and a limited quantum efficiency of recent detectors. Therefore, especially for plastics, even larger plastic waste aggregates may not be detectable from space, as they usually exhibit sparse and small-scale distributions. Therefore, the focus related to hyperspectral satellite data must be on synthetics with a large spatial extent, such as greenhouses, photovoltaic components, roofing materials and materials commonly found at industrial sites. Another constraint and challenge in identifying plastics from satellite data is that plastics of the same type have different optical properties. In particular, most plastics remain transparent or translucent and are thin to save cost, introducing a quadratic term in transmittance and reflectance of

the background directly below it. Thus, the background has a strong influence on the apparent reflectance (Kuester and Bochow, 2019; Eisenreich and Rohe, 2006).

Further, even if plastic types are successfully classified by satellite spectral data, it is still not possible to directly assign functions based on chemical bonds alone, but the assignment of functions will help determine whether these plastic materials need to be recycled. The previously mentioned pixel-level processing technique of assigning each pixel to one of the categories based on its spectral information is not sufficient for the function of a plastic material. The spectrally derived information for a unique plastic type does not necessarily correspond to the function of the respective plastic material. Plastic products with the same function can be made of different plastic types and vice versa, and can even have different appearances. For example, photovoltaic panels are a mixture of various plastic materials (Oreski et al., 2021) and plastic roofs can have different colors and shapes. Therefore, contextual information (in the spatial domain) should be additionally integrated to further distinguish the utility or function of plastic-covered areas.

3 Research methodology

3.1 Challenges in identifying and monitoring plastic using satellite remote sensing

Monitoring plastic using satellite remote sensing is a complex endeavor with a variety of challenges. Most significant ones are:

- **Spatial resolution**: Plastic waste can vary in size and shape, from large floating debris to small microplastics. The spatial resolution of satellite imagery is typically not high enough to detect small plastic debris on land surfaces. This limits the accuracy of plastic waste detection and classification.
- **Spectral resolution**: Plastic waste is composed of various materials, each with distinct spectral properties. However, the spectral resolution of satellite imagery may not be sufficient to distinguish between various sorts of plastic.
- **Cloud cover**: Cloud cover can obstruct the view of land surfaces, making it difficult to obtain clear satellite images. This can limit the frequency of observations and especially increase the likelihood of missing mobile plastic assemblies.
- **Data availability**: Access to satellite data can be limited due to factors such as cost and availability which is especially true for high spatial commercial systems. This can prevent the ability to perform long-term monitoring and the analysis of plastic waste trends.
- **Ground truthing**: Validating plastic waste detection and classification using satellite imagery requires accurate ground truth data. Obtaining ground truth data can be challenging, time-consuming, and expensive.
- **Surface reflectance variability**: The reflectance of land surfaces can vary depending on factors such as land cover, moisture content, and atmospheric conditions. This can affect the accuracy of plastic waste detection and classification using satellite imagery, as plastic debris can be easily masked by surface features with similar reflectance properties.
- **Interference from other sources**: Further sorts of man-made debris, such as e.g. glass and metal, can spectrally interfere with the properties of plastic waste. This can lead to confusion and misclassifications of debris, particularly in urban areas where a high concentration of man-made materials is to be found.

Addressing all these challenges requires a multidisciplinary approach that involves combining remote sensing techniques deployed on different platforms with field observations and laboratory experiments. Thus, the development of advanced and innovative

remote sensing techniques is needed, as well as a better understanding of the physical properties of plastic waste and their interactions with the environment to improve the accuracy and reliability of its detection and classification.

3.2 Data analysis methods used

This chapter focuses on the investigation of software and suitable analysis methods used in this thesis. By delving further into the methods applied for data analysis, one can better understand how the insights and conclusions in this thesis were obtained.

3.2.1 Standard classification algorithms

- **Spectral Angle Mapper (SAM)** is a signal-based spectral classification method used in remote sensing and image processing (Kruse et al., 1993; Hoffbeck and Landgrebe, 1996). The method is widely used in the classification of satellite and airborne imagery, as well as in identifying materials and features on the Earth's surface. SAM matches pixels to reference spectra by calculating the n-D angle between them, and determines the spectral similarity between the reference and unknown vectorized spectra. The SAM algorithm generalizes this geometric interpretation to n-dimensional space. SAM determines the similarity by applying the following equation:

$$a = cos^{-1}\left(\frac{\sum_{i=1}^{n} t_i r_i}{\sqrt{\sum_{i=1}^{n} t_i^2}\sqrt{\sum_{i=1}^{n} r_i^2}}\right) \tag{3.1}$$

  One of the main advantages of SAM is its insensitivity to varying illumination conditions. This means that the algorithm can be used to classify spectral data regardless of changes in Suns' position or strong relief differences on the target area. SAM achieves this by calculating the angle between the reference and unknown spectra, rather than comparing their absolute values. This makes SAM more robust than other spectral classification methods that rely solely on the absolute values of the spectra.

  SAM is also flexible in terms of the reference spectra used for classification. The reference spectra can be obtained from a spectral library or extracted directly from the respective image. To use SAM, the user must specify a maximum angle threshold in radians. Pixels with angles smaller than this threshold are classified as matching the reference spectrum, while those with angles larger than the threshold are not classified.

  SAM is particularly useful in situations where the spectral signatures of the materials being classified are well-defined. For example, it can be used to map land cover types, identify geological features, and monitor changes in vegetation cover. However, it may not be suitable for tasks where the spectral characteristics of the materials being classified are similar, or where there is significant overlap in the spectral signatures of different materials.

- **Maximum Likelihood Estimation (MLE)** The MLE method is a statistical approach for estimating the parameters of a probability distribution that best describe

the observed data. The method is widely applied in various fields, including remote sensing, where it is used for image classification based on the spectral signatures of pixels. The MLE approach assumes that the spectral signatures for each land cover class are normally distributed, and calculates the probability of a pixel belonging to a specific class based on its spectral signature. The method assigns each pixel to the class with the highest probability, which is known as the maximum likelihood class. The MLE method is unbiased and efficient, and provides a robust and accurate approach for image classification.

The MLE method uses the following equation to calculate the probability of a pixel belonging to a specific class:

$$P(c|x) = \frac{1}{(2\pi)^{d/2}|\Sigma_c|^{1/2}} e^{-\frac{1}{2}(x-\mu_c)^T \Sigma_c^{-1}(x-\mu_c)} \tag{3.2}$$

where c is the target class, x is the spectral signature of the pixel, d is the number of spectral bands, μ_c is the mean vector for class c, and Σ_c is the covariance matrix for class c. The notation $|\Sigma_c|$ denotes the determinant of the covariance matrix, and the superscript T denotes the transpose operation.

The MLE method assigns each pixel to the class with the highest probability, which is computed using the above equation for each class. The maximum likelihood class is given by:

$$c_{MLE}(x) = \arg\max_{c \in C} P(c|x) \tag{3.3}$$

where C is the set of all classes. The above equation finds the class that maximizes the probability of the spectral signature given the class, and assigns the pixel to that class. If the highest probability is below a specified threshold, the pixel remains unclassified.

3.2.2 Machine learning algorithms

- **SVM** support vector machines are machine learning algorithms commonly used for classification tasks, particularly well-suited for high-dimensional feature spaces where linear separation is not possible. In remote sensing, SVMs are used for land cover classification using spectral information. The SVM algorithm finds the optimal hyperplane that separates the data into two classes with the maximum margin. Given a training dataset of n samples with d features, the hyperplane is defined by:

$$f(x) = \boldsymbol{w}^T \boldsymbol{x} + b = 0 \tag{3.4}$$

where $\boldsymbol{x}$ is the feature vector, $\boldsymbol{w}$ is the weight vector, and b is the bias term.

The SVM algorithm aims to maximize the margin γ subject to the constraint that all training samples are correctly classified. The margin is given by:

$$\gamma = \frac{2}{||\boldsymbol{w}||} \tag{3.5}$$

where $||\boldsymbol{w}||$ denotes the Euclidean norm of the weight vector.

To overcome the non-convex optimization problem, the SVM algorithm uses a kernel function to transform the data into a higher-dimensional feature space, where linear separation is possible. The RBF kernel is particularly popular for remote sensing applications, and is defined as:

$$k(\boldsymbol{x}_i, \boldsymbol{x}_j) = e^{-\gamma||\boldsymbol{x}_i - \boldsymbol{x}_j||^2} \tag{3.6}$$

where γ is a parameter that controls the width of the kernel, and $||\cdot||$ denotes the Euclidean distance between the feature vectors.

To avoid overfitting, the SVM-RBF algorithm introduces a regularization parameter C that trades off the margin size and the training error. The SVM-RBF algorithm tries to find the optimal hyperplane that maximizes the margin subject to the constraint that the sum of the slack variables is less than or equal to C. The slack variables are introduced to allow for some misclassifications in the training data. The optimization problem can be formulated as:

$$\begin{aligned} \text{minimize} \quad & \frac{1}{2}||\boldsymbol{w}||^2 + C\sum_{i=1}^{n}\xi_i \\ \text{subject to} \quad & y_i(\boldsymbol{w}^T\boldsymbol{\phi}(\boldsymbol{x}_i) + b) \geq 1 - \xi_i, \quad i = 1, \ldots, n \\ & \xi_i \geq 0, \quad i = 1, \ldots, n \end{aligned} \tag{3.7}$$

where $\boldsymbol{\phi}(\boldsymbol{x}_i)$ is the feature map of the input vector $\boldsymbol{x}_i$ in the transformed feature space, y_i is the class label of sample i, and ξ_i are slack variables that allow for some misclassifications in the training data.

The SVM-RBF algorithm finds the optimal hyperplane in the transformed feature space that maximizes the margin between the positive and negative classes, which corresponds to a nonlinear decision boundary in the original feature space.

- **RF** random forest is a popular ensemble machine learning algorithm that improves prediction accuracy and robustness by combining multiple individual models. Introduced in 2001 by Leo Breiman and Adele Cutler as an extension of decision trees, Random Forest is suitable for classification and regression tasks, including large datasets, high-dimensional feature spaces, and non-linear input feature-target variable relationships.

  Random Forest creates T decision trees, where each tree is trained on a different subset of the data and features to reduce overfitting and improve the generalization ability of the model. The final prediction is the majority vote of all the trees in the forest. The algorithm can be described mathematically as follows:

  Given a training set $(x_i, y_i)_{i=1}^N$ where $x_i \in \mathbb{R}^d$ and $y_i \in 1, 2, ..., K$, the goal is to learn a function $f(x)$ that maps input features to output labels.

  Random Forest constructs T decision trees $T_1, T_2, ..., T_T$ using a bootstrapped sample of the training data, where each tree is trained on a random subset of the features. The bootstrapped sample is created by randomly sampling N data points from the training set with replacement. For each tree T_i, a random subset of m features is selected from the d features in the training set. The value of m is typically set to $\sqrt{d}$ for classification problems and $d/3$ for regression problems.

Each decision tree is trained using the standard algorithm for decision tree induction, such as ID3, C4.5, or CART. The tree splits the data based on the best feature and threshold according to an impurity measure, such as the Gini index or entropy. The tree continues to split the data until the leaves contain only one class or a pre-defined stopp criterion is met.

To make a prediction for a new input feature vector x, the algorithm takes the majority vote of the predictions made by all the decision trees in the forest:

$$f(x) = \text{argmax}k \in 1, 2, ..., K \sum i = 1^T \mathbb{I}(T_i(x) = k)$$

where $T_i(x)$ is the predicted class label of the i-th decision tree for input vector x, and $\mathbb{I}(T_i(x) = k)$ is the indicator function that returns 1 if $T_i(x) = k$ and 0 otherwise.

In summary, Random Forest combines multiple decision trees trained on bootstrapped samples of the data and subsets of the features to create a powerful machine learning algorithm.

3.2.3 Convolutional Neural Networks

CNN are highly effective for image classification tasks due to their hierarchical representation learning and spatial correlation handling capabilities. These networks consist of multiple layers, including convolutional, pooling, and fully connected layers, that extract features, reduce spatial dimensionality, and make predictions. The use of skip connections promotes identical mappings and allows for deeper layers to extract discriminative semantic features, which are crucial for understanding image content. In this section, some popular CNN architectures that are commonly used as a baseline are introduced to gain an understanding of CNNs.

GoogLeNet, also called Inception, was introduced as a deep convolutional neural network architecture in 2015 with the aim to reduce the computational complexity of deep neural networks (Szegedy et al., 2015). It achieves this by incorporating inception modules, which include multiple convolutional filters of different sizes, to learn hierarchical representations of the image by extracting information from multiple scales. The architecture of the Inception module in GoogLeNet is illustrated in Figure 3.1, where 1×1, 3×3, and 5×5 convolutions, and 3×3 max-pooling are applied to inputs. The parallel use of filters reduces the number of parameters and computation time compared to traditional CNN that use sequential layers.

VGGNet is a deep neural network architecture that was developed by the Visual Geometry Group at the University of Oxford, specifically for image classification tasks (Simonyan and Zisserman, 2014). VGGNet arranges convolutional layers in a block-wise manner and consists of five convolutional blocks and three fully-connected layers, and after each block, a max-pooling layer is added to downsample feature maps. All convolutional filters have a size of 3×3, and each convolutional layer in a block has the same number of filters. For example, in the VGGNet-13, each layer in the five blocks has 64, 128, 256, 512, and 512 convolutional filters, respectively (Figure 3.2). A feature of the VGGNet is that reducing the size of the convolutional filter and increasing the number of layers can achieve a similar deep perceptual field while using fewer parameters. This approach can also enhance the nonlinearity of the model. After the success of the VGGNet, this

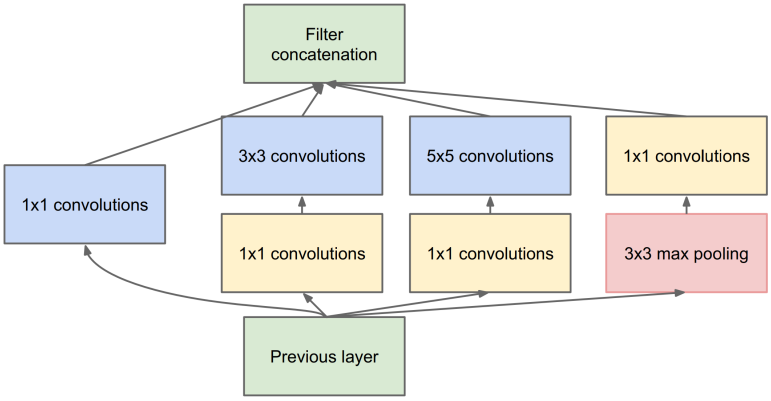

Figure 3.1: Inception module in the GoogLeNet. Source: Szegedy et al. (2014)

strategy of designing convolutional neural networks in a block-like manner has become a mainstream trend in deep learning research.

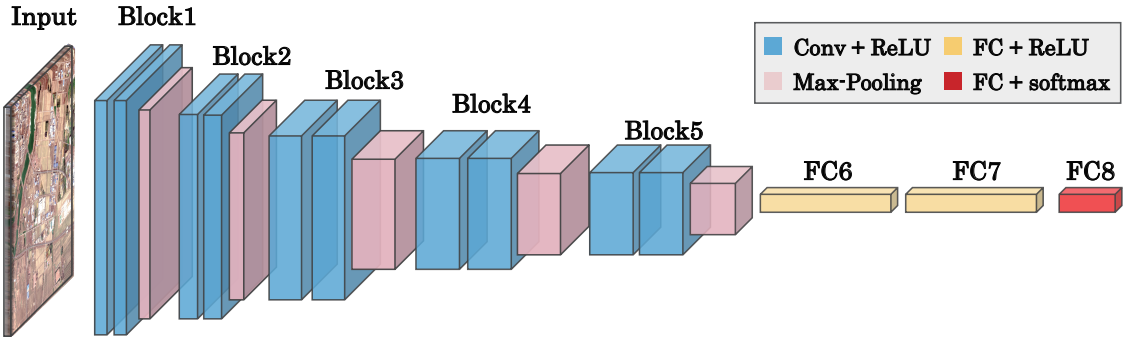

Figure 3.2: Architecture of the VGGNet-13. Conv: convolutional layer, FC: fully-connected layer. Modified from: Simonyan and Zisserman (2014)

ResNet is a deep Convolutional Neural Network (CNN) created by Microsoft Research (He et al., 2016) that addresses the degradation problem typically encountered in deep networks. The unique feature of ResNet's architecture is the incorporation of identity shortcuts, which are also known as skip connections. These shortcuts enable information to be directly transmitted from lower to higher layers of the network, preventing the issue of vanishing gradients and allowing the network to learn even deeper architectures with up to 152 weight layers (as shown in Figure 3.3). The use of identity shortcuts improves the stability and convergence of training, as well as reducing the need for careful weight initialization. This innovative ResNet structure has been widely implemented in vision tasks and continues to achieve state-of-the-art performance on various benchmark datasets.

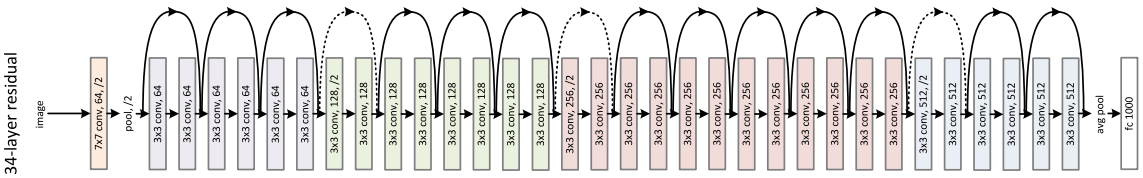

Figure 3.3: Architecture of the ResNet-34. Source: He et al. (2016)

4 Plastic detection using lab.-, airborne data and superspectral WorldView-3 satellite data

This chapter was published as:
Zhou, S., Kuester, T., Bochow, M., Bohn, N., Brell, M., & Kaufmann, H. (2021). A knowledge-based, validated classifier for the identification of aliphatic and aromatic plastics by WorldView-3 satellite data. *Remote Sensing of Environment*, 264, 112598.

4.1 Abstract

Although the C-H chains of petroleum derivatives display unique absorption features in the short-wave infrared (SWIR), it is a challenge to identify plastics on terrestrial surfaces. The diverse reflectance spectra caused by chemically varying polymer types and their different kinds of brightness and transparencies, which are, moreover, influenced further by the respective surface backgrounds. This paper investigates the capability of WorldView-3 (WV-3) satellite data, characterized by a high spatial resolution and equipped with eight distinct and relatively narrow SWIR bands suitable for global monitoring of different types of plastic materials. To meet the objective, hyperspectral measurements and simulations were conducted in the laboratory and by aircraft campaigns, based on the JPL-ECOSTRESS, USGS, and inhouse hyperspectral libraries, all of which are convolved to the spectral response functions of the WV-3 system. Experiments further supported the analyses wherein different plastic materials were placed on different backgrounds, and scaled percentages of plastics per pixel were modeled to determine the minimum detectable fractions. To determine the detectability of plastics with various chemical and physical properties and different fractions against diverse backgrounds, a knowledge-based classifier was developed, the routines of which are based on diagnostic spectral features in the SWIR range. The classifier shows outstanding results on various background scenarios for lab experimental imagery as well as for airborne data and it is further able to mask non-plastic materials. Three clusters of plastic materials can clearly be identified, based on spectra and imagery: The first cluster identifies aliphatic compounds, comprising polyethylene (PE), polyvinylchloride (PVC), ethylene vinyl acetate copolymer (EVAC), polypropylene (PP), polyoxymethylene (POM), polymethyl methacrylate (PMMA), and polyamide (PA). The second and third clusters are diagnostic for aromatic hydrocarbons, including polyethylene terephthalate (PET), polystyrene (PS), polycarbonate (PC), and styrene-acrylonitrile (SAN), respectively separated from polybutylene adipate terephthalate (PBAT), acrylonitrile butadiene styrene (ABS), and polyurethane (PU). The robustness of the classifier is examined on the basis of simulated spectra derived from our HySimCaR model, which has been developed in-house. The model simulates radiation transfer by using virtual 3D scenarios and ray tracing, hence, enables the analysis of the influence of various factors, such as material brightness, transparency, and fractional coverage as well as different background materials. We validated our results by laboratory and simulated datasets and by tests using airborne data recorded at four distinct sites with different surface characteristics. The results of the classifier were further compared to results produced by another signature-based method, the spectral angle mapper (SAM) and a commonly used technique, the maximum likelihood estimation (MLE). Finally, we applied and successfully tested the classifier on WV-3 imagery of sites known for a high abundance of plastics in Almeria (Spain), Cairo (Egypt), and Accra, (Ghana, West Africa). Both airborne and WV-3 data were atmospherically corrected and transferred to "at-surface reflectances". The results prove the combination of WV-3 data and the newly designed classifier to be an efficient and reliable approach to globally monitor and identify three clusters of plastic materials at various fractions on different backgrounds.

4.2 Introduction

Plastic litter enters the environment through manifold pathways and has a major deleterious impact on our living space. This phenomenon is of growing concern, and has kindled the idea to investigate the possibilities of monitoring and identification of plastic litter in the terrestrial environment using remote sensing techniques. Plastic products - with the advantages of being lightweight, waterproof, and durable - have become increasingly dominant in the marketplace since their widespread introduction in the 1930s (Feldman, 2008). Global plastic production has quadrupled over the past four decades (Geyer et al., 2017). Improper disposal of plastic waste, along with its longevity and durability, have caused its extensive accumulation in terrestrial and aquatic ecosystems (Derraik, 2002). This has led to a severe damage to wildlife (Browne et al., 2008; Uhrin and Schellinger, 2011) and its habitats (Lebreton et al., 2017). Besides, many plastics can be chemically hazardous in some contexts. More than 50% of plastics are inherently toxic (Lithner et al., 2011). Even when not toxic, plastics can absorb and accumulate other pollutants (Teuten et al., 2009; Rochman et al., 2013). When plastic is exposed to ambient solar radiation, it slowly disintegrates into microplastics and releases greenhouse gases, methane and ethylene, contributing to climate change and global warming effects (Royer et al., 2018; Vishwakarma, 2020). People are, therefore, now paying more and more attention to the impact of plastics on the ecosystem and human health (Lithner et al., 2011; Rochman et al., 2013; Law and Thompson, 2014; Law, 2017). Consequently, it is a challenging future obligation to regularly monitor and detect plastic materials to better identify the sources and pathways of plastic litter and to assess its accumulation over time.

The unique inherent optical characteristics of different types of plastics in the near infrared (NIR) to shortwave infrared (SWIR) allow plastic litter to be sorted automatically by the recycling industry (Huth-Fehre et al., 1995; Masoumi et al., 2012; Moroni et al., 2015). With the development and improvement of the SWIR (1.3-2.5µm) imaging technology, remote sensing data with moderate to high temporal, spectral, and spatial resolution bear the potential to be a powerful tool for qualitative and quantitative mapping of plastic occurrences in the environment (Moller et al., 2016). Mapping and quantification of marine and coastal plastic litter based on remote sensing data (NIR, SWIR, TIR) have recently been investigated by a growing number of studies (Moy et al., 2018; Acuña-Ruz et al., 2018; Garaba et al., 2018; Martínez-Vicente et al., 2019; Goddijn-Murphy and Williamson, 2019; Fallati et al., 2019; Themistocleous et al., 2020; Biermann et al., 2020; El Mahrad et al., 2020; Topouzelis et al., 2020). Some authors investigated the detection of plastic greenhouses using statistical classification algorithms based on spectral and textural characteristics (Novelli et al., 2016; Aguilar et al., 2016; Lanorte et al., 2017; Aguilar et al., 2020). Others focused on the differentiation among various plastic types by lab measurement and near-real-time algorithms, which allow the sorting of harvested plastic waste on automated conveyor belts with infrared spectroscopy (Yan and Siesler, 2018; Rani et al., 2019; Cruz Sanchez et al., 2020). Most plastic litter ends up in the oceans through miscellaneous routes and is crushed by mechanical wave, forcing it up to nano-sized particles. Approximately 80 percent of ocean plastics originate from land-based sources; the remaining 20 percent are from marine sources (Li et al., 2016).

To prevent further contamination, regular global monitoring of terrestrial plastic debris is of increasing importance. So far, only a few studies have focused on the detection and identification of terrestrial plastics, mostly based on hyperspectral imagers aboard air-

planes (Hörig et al., 2001; Kühn et al., 2004; Heiden et al., 2007) and satellites (Wetherley et al., 2017). But airborne sensors are limited in terms of covering larger areas. On the contrary, hyperspectral recordings from space have the disadvantage of low Ground Sampling Distances (GSDs) $\leq$ 30 m on account of the limited quantum efficiencies of recent detectors. Therefore, a "super-spectral" instrument such as the DigitalGlobe WorldView-3 system is a suitable solution as tradeoff between spectral and spatial resolution. It can be advantageous to hyperspectral imagers as well as to very high spatial resolution satellite sensors where the latter usually suffer from low repetition rates and missing spectral capabilities. WV-3 data have already been investigated by Asadzadeh and de Souza Filho (2016), delineating the potential to detect hydrocarbon (HC) materials based on simulated imagery. They further proved the data to be capable to unambiguously detect HCs in varying background soils. Some researchers have already proposed knowledge-based indices, such as HI (Kühn et al., 2004), RBD (Asadzadeh and de Souza Filho, 2016), and NDPI, which can be used as one-class classifiers by applying a threshold on the index value, among which NDPI has been proven to have superior performance (Guo and Li, 2020). This index can highlight most of the plastics innovatively by amplifying the significant downward tendency of most plastics along 1570 to 1730 nm and 2165 to 2330 nm, however, it doesn't cover all the plastic types. Yet, these studies rarely provide a reliable identification of different plastic materials, although this is a major challenge in this context.

Concerning the evaluation of recorded air-, or spaceborne data, various supervised classifiers based on signatures have been reported in the literature. Conventional approaches to chemical agents and soil detection using spectroscopic techniques are discussed by Kruse et al. (1993) and Kwan et al. (2006). Moreover, popular deep learning algorithms are used for land cover classification (Kwan et al., 2020). All of these methods can be used to classify plastics. The most common household waste consists of five main polymers, including PE, PP, PS, PET, and PVC (Eisenreich and Rohe, 2006; Feldman, 2008; Editor, 2018). For cost-saving reasons, most plastics remain transparent or translucent and thin, introducing the quadratic term of transmittance and the reflectance of background directly below it. Hence, the background has great impact on the apparent reflectance (Kuester and Bochow, 2019). The varying fractions of plastics in relation to different backgrounds further introduce uncertainty into any kind of detection and identification algorithms. Hence, supervised classification methods would require a large number of training pixels, covering all the above-mentioned combinations and circumstances. Unsupervised classification algorithms like ISODATA (Tou and Gonzalez, 1974) and K-Means (Hartigan and Wong, 1979), require knowledge about the number of classes in the image to obtain good results; also, they cannot be used to automatically identify materials. Statistically machine learning methods became very popular but have a limited transfer-ability and often require adaption to specific areas and tasks.

The work presented in this paper focuses on the development of a knowledge-based algorithm, evaluating the spectral reflectance signal, which can identify different types or clusters of plastics on various terrestrial backgrounds by the use of the globally operating WV-3 satellite system. As mentioned before, WV-3 is characterized by eight well-placed SWIR bands and a sufficient high spatial resolution for this purpose. To initiate the classifier, we investigated three international spectral libraries, including around 3,600 samples, whereby all spectra were convolved to WV-3 band characteristics using its spectral response function. We iteratively improved the algorithm with lab measurements and

simulated spectra, covering a broad range of different, commonly used types of plastics, various levels of brightness and transparency, detailed fractional coverages of plastic material per pixel, and the interfering reflectance of 12 different background materials. Finally, the developed, signature-based, decision tree type classifier was applied to simulated data, four airborne images recorded in Germany and Spain, and three WV-3 scenes covering known areas of high plastic abundance in Spain (Almeria), West Africa (Accra, Ghana), and Egypt (Cairo) (Fig. 4.1).

4.3 Materials

4.3.1 Laboratory data

4.3.1.1 Existing spectral libraries

To investigate the potential for the detection and recognition of different plastic materials as well as to mask and separate all other materials from plastics, spectral libraries from JPL-ECOSTRESS (Baldridge et al., 2009; Meerdink et al., 2019), USGS (Kokaly et al., 2017) and our inhouse spectral library (GFZ), were investigated. Only diagnostic spectral signatures located in the NIR and SWIR ranges were selected to ensure credibility for the subsequent spectral resampling. Table 4.1 lists the details of spectral libraries and categories that were considered in this study. A synthetic scenery of 60-by-60 pixels was generated covering 3,547 spectra of natural surfaces, including 156 samples of different plastics materials. All reflectance data were rescaled into the range of 0 to 100% to facilitate joint analysis.

Table 4.1: Summary of the spectral libraries used for this study.

Spectral library	Number of spectra	Category
ECOSTRESS	1947	Artificial, water, minerals, rocks, soils, vegetation, non-photosynthetic vegetation
USGS	1436	Artificial, coatings, liquids, minerals, soils, vegetables
GFZ	164	ABS, EVAC, PE, PBAT, PC, PET, POM, PP, PS, PU, PVC, SAN, PMMA, PA and natural organic materials
Total	3547	

The USGS library (Version 7) contains hyperspectral reflectance data of various materials that cover the wavelength range from the ultraviolet to the far infrared (0.2 to 200 μm). It includes spectra measured in the laboratory, field, and by airborne imaging spectrometers. It contains reflectance spectra from samples of minerals, rocks, and soils as well as of vegetation, microorganisms, and man-made materials, which involves PE, PVC, PET, and PA. The category of organic chemical substances is excluded in this study as their molecular structures are similar to plastics, but rarely disperse in nature. The ECOSTRESS library provides a comprehensive collection of natural and man-made laboratory-derived high-resolution spectra, covering the wavelength range of 0.35–15.4 μm. It includes nearly 2,000 spectra of soils, rocks, minerals, meteorites, vegetation, non-photosynthetic vegetation (NPV), water/snow/ice, and man-made materials. There are two roofing rubbers in the man-made category, which are plastic samples. The PlaMAPP library is an in-house (GFZ) created collection of high-resolution spectra measured in the

Table 4.2: Different plastics sorted by their molecular structure. Materials used for household goods and packaging are marked in bold.

Type of Chemical Compound	Plastic types
Aliphatic	**PE**, **PVC**, EVAC, **PP**, POM, PMMA, PA
Aromatic	ABS, PBAT, PU, **PET**, **PS**, PC, SAN

near infrared and shortwave infrared range (0.97-2.5 μm). It includes five types of household plastics, which cover 95% of the global production of PE, PP, PVC, PET, and PS, as well as nine types of industrial plastics: ABS, EVAC, PA, PBAT, PC, PMMA, POM, PU, and SAN. These plastics - in accordance with the type of functional groups present in their molecular structure - can be divided into an aliphatic type (without a benzene ring) and an aromatic type (containing a benzene ring), and are listed in Table 4.2. In total, 3,547 spectral signatures were used to develop and evaluate the classifier.

4.3.1.2 Additional lab measurements

Additional measurements were conducted to derive high-resolution spectra of various plastic types placed on the surfaces of different backgrounds which is required for the development of the classifier. Measurements are conducted under laboratory conditions with an internal measurement protocol (Rogass et al., 2017) with a HySpex SWIR320m-e hyperspectral imager built by Norsk Elektro Optikk (NEO). A H25s light source by HEDLER was used, which is equipped with two 650 Watts tungsten halogen bulbs radiating a near solar-like spectrum. After calibrating the measured digital numbers to radiance using the software HySpex RAD, the conversion to reflectance was accomplished using spectra from a 3-color Zenith® reference panel (albedo: 90%, 50%, 20%), which was placed in every imaged scene. Two scenes were set up, including samples of six plastic materials (HDPE, PVC, PS, PP, PET, and PBAT), with different optical characteristics like transparent, translucent, opaque-bright, and opaque-dark. Samples were placed on two different soil types viz a bright sandy dry soil and a dark organic dry soil.

4.3.1.3 The HySimCaR model

To further consolidate the database, it was extended by simulated mixed spectra based on HySpex measurements, using a radiative transfer model HySimCaR (hyperspectral simulation of canopy reflectance (Kuester et al., 2014) that was developed in-house and modified. The model enables the simulation of realistic bidirectional reflectance spectra on the basis of virtual 3D scenarios with Monte Carlo ray-tracing (MCRT) techniques. The spectral reflectances of the mixed samples were calculated by a spectral modeling approach that couples virtual 3D plastic litter scenarios, the geometries of which are linked to the corresponding spectral information (reflectance spectra of background materials, reflectance, and transmittance spectra of plastic materials). Apart from the complexity of varying spectral backgrounds in the terrestrial environment, classification algorithms applied to satellite imagery face the dominance of mixed pixels, causing greater uncertainties in the results of classification approaches. Hence, the fractional cover of the plastic material for the analysis of the mixed pixel problem was calculated directly from the 3D geometry of the virtual littering scenarios. Subsequently, by using the Atmospheric and Topographic

Correction (ATCOR) model (Richter and Schläpfer, 2019), all the lab reflectance spectra derived are converted to surface reflectances, as seen by the WV-3 sensor, taking into consideration random noise and atmospheric effects.

4.3.2 Sensor systems

4.3.2.1 Airborne instruments

Data recorded by four push-broom hyperspectral sensors, including the HySpex-VNIR-1600, HySpex-SWIR-320m-e, HySpex Mjolnir S-620 (NEO), and the HyMap sensor (Cocks et al., 1998) were used in this study. The HySpex-VNIR-1600 covers 160 bands in the spectral range of 0.4-1.0 μm, with a spectral resolution of 3.6 nm, while the HySpex-SWIR320m-e operates in the 1.0-2.5 μm range, producing 256 bands with a spectral sampling of 6 nm. Both sensors were mounted on an aircraft with an across-track instantaneous field of view (IFOV) up to 0.185 mrad for the VNIR camera (1600 pixels) and 0.75 mrad for the SWIR camera (320 pixels). The HySpex Mjolnir S-620 is a UAV-based sensor, with an across-track IFOV of 0.54 mrad. It records lines with 620 pixels, covering a range of 1.0-2.5 μm in 300 bands, with a spectral resolution of 5.1 nm. The HyMap imager has an IFOV of 2.0 mrad with 512 pixels in across track direction, covering the range of 0.45-2.48 μm in 128 bands with intervals of 13-17 nm. This sensor can only be used in connection with an aircraft.

4.3.2.2 WorldView-3 sensor

The WorldView-3 is a high spatial resolution commercial satellite operating in a sun-synchronous orbit, carrying a sensor with moderately broad spectral bands in the VNIR-SWIR (visible, near infrared - short wave infrared) range. In the VNIR, it provides four standard color bands and four additional bands, named coastal, yellow, red edge, and near-IR2. The details of the spectral band configuration are shown in Table 4.3. The major advancement of the WV-3 system are eight SWIR bands in the 1195-2365 nm atmospheric window. Twelve additional CAVIS (Clouds, Aerosols, Vapors, Ice, and Snow) bands guarantee proper estimates of aerosols and water vapor for atmospheric compensation of the data. The platform operates at an altitude of 617 km. The GSDs at nadir are 0.31 m for the panchromatic band, 1.24 m for the VNIR bands, 3.7 m for the SWIR bands, and 30 m for the CAVIS bands. The swath width of the instrument is 13.1 km, with a descending node at 10:30. Owing to the onboard fast-reacting "Control Moment Gyros" (CMGs), the off-nadir revisit time is <1 day. Data provided are already geo-corrected.

4.4 Study areas

To ensure testing and validation of the classifier to be developed in this study for its potential to identify different plastic materials in a real-world environment under various conditions, several regions with miscellaneous surface characters were recorded by aircraft and satellite data.

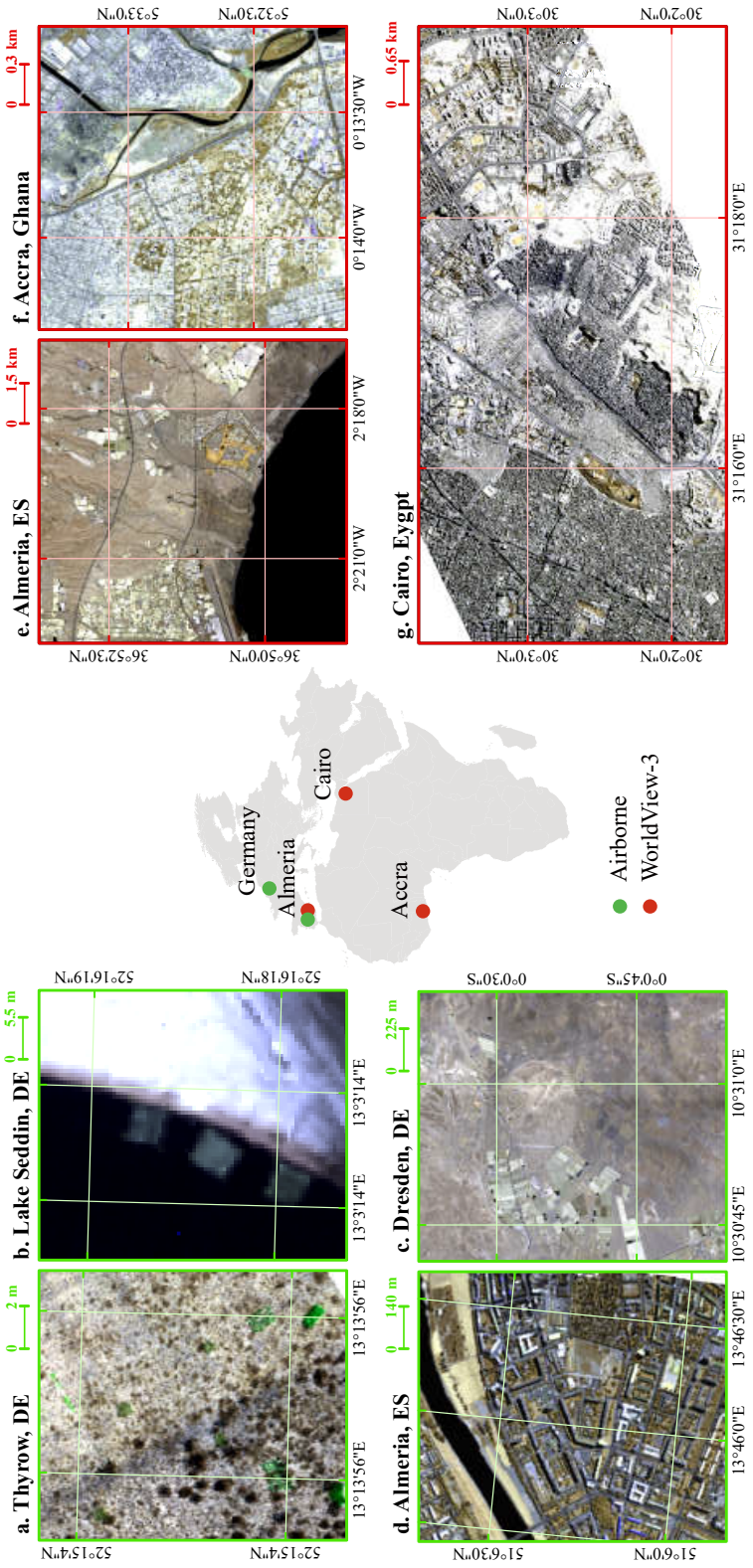

Figure 4.1: Sketch map and detailed coordinates of test sites recorded by aircraft scanners and the WV-3 satellite.

Table 4.3: Spectral band configuration of VNIR and SWIR bands of the WorldView-3 sensor.

Band number	Band name	Wavelength/nm	Band number	Band name	Wavelength/nm
1	coastal:	400-450	9	SWIR 1:	1195-1225
2	blue:	450-510	10	SWIR 2:	1550-1590
3	green:	510-580	11	SWIR 3:	1640-1680
4	yellow:	585-625	12	SWIR 4:	1710-1750
5	red:	630-690	13	SWIR 5:	2145-2185
6	red edge:	705-745	14	SWIR 6:	2185-2225
7	near IR 1:	770-895	15	SWIR 7:	2235-2285
8	near IR 2:	860-1040	16	SWIR 8:	2295-2365
GSD	1.2 m		GSD	3.7 m	

4.4.1 Sites recorded by airborne instruments

Four selected locations in Germany and Spain (Fig.4.1 a-d), each characterized by a different landscape, were recorded by the above mentioned airborne instruments. To ensure validity, plastic targets in the airborne data sets were not included in the spectral libraries used for the development of the classifier.

A location - dominated by grassland - was recorded by the HySpex Mjolnir S-620 imager mounted on an UAV on June 13, 2019, at Thyrow, Germany (52°15'04.6"N 13°13'55.7"E, Fig.4.1 a). The flight altitude was about 30 m, resulting in a GSD of about 3 cm. We placed well defined and spectrally measured materials on the ground like transparent PET plastic bottles of different size, and large foils made of PBAT, PET, and PE plastic. The geometric processing was conducted with the PARGE software (Schläpfer and Richter, 2002) and the atmospheric correction was done in-house using the SICOR software (Bohn et al., 2020).

The data of the lake location were recorded by the combined HySpex VNIR-1600 and SWIR-320m-e sensors aboard an airplane on February 16 in 2015 at Lake Seddin, Germany (52°16'21.4"N 13°03'12.3"E, Fig.4.1b). Data were collected at an altitude of 600 m, with a resultant GSD of about 40 cm. HySpex data preprocessing to orthorectified reflectance including co-registration and adaptation of the SWIR sensor to the VNIR was performed with the GFZ in-house processing chain HyPrepAir which is based on procedures described by Brell et al. (2016). Three arrays of white and opaque PS foam boards (fractional covers of 15%, 25%, and 40%) and one blue PE tarpaulin (100% fractional coverage) were set up over the shallow lake water and on its sandy bank. The above described two scenes represent fully controlled experiments and the ground truth map including all the samples is generated accordingly.

A third study area - characterized by an urban landscape - was recorded by the HyMap system from an aircraft. The urban scenery depicts the city of Dresden, Germany (51°6'17.5"N 13°46'6.8"E, Fig.4.1c), and was collected on July 7, 2004, with a GSD of 4 m. Ground control for places covered by distinct plastic materials in the resp. regions are maintained by field-works using portable spectrometers and GPS devices. Coverages by the respective plastic materials at individual city blocks were digitized manually on-screen using ortho-rectified aerial photographs of 0.25 m resolution. More than 40 different urban materials including various plastics were identified and mapped based on hyperspectral ground measurements (Behling et al., 2015). For this study, we merged all the found classes into the respective three plastic and one non-plastic cluster, each of them finally comprising more than 250 pixels.

A further area characterized by bare soils and greenhouse agriculture in Almeria, Spain (0°0'38.2"S 10°30'55.5"E, Fig.4.1d), was acquired in June 15 using the HyMap system onboard an airplane in 2005, with a GSD of 5 m. This site is dominated by PE plastic sheds utilized as greenhouses for agricultural purposes (Scarascia-Mugnozza et al., 2011). Similar to the Dresden dataset, the ground control is conducted by field measurements with portable spectrometers and GPS. However, due to the lack of diversity of plastics, only greenhouses made from PE were collected for the ground truth map with more than 10,000 pixels.

All these datasets are of L2 level, passing radiometric corrections, atmospheric corrections, and ortho-registration.

4.4.2 Sites recorded by the WorldView-3 satellite

Three WV-3 datasets (Fig4.1e-g) were selected from regions known for their high abundance of plastic material. One dataset was recorded over Europe (Almeria, Spain), one over West Africa (Accra, Ghana), and one over North Africa (Cairo, Egypt). They were collected in Ortho Ready Standard Level-2A (ORS2A) format, presenting both radiometric and geometric corrections. To retrieve the "at surface reflectance" characteristics of targeted areas, atmospheric corrections were applied using the ATCOR 2 software (Richter and Schläpfer, 2007).

4.4.2.1 Almeria, Spain

The imagery of Almeria, Spain (2°19'29.9"N 36°51'16.1"W, Fig.4.1e), depicts an agricultural region and was recorded on June 26, 2018. The economy of Almería is mostly dependent on agricultural products, cultivated mainly in the western part of the city. Numerous greenhouses constructed from plastic sheeting produce tons of fruits and vegetables; more than 70% of which are exported to other European countries. About 30,000 tons of plastic waste are created here per year. In places where the soil has become infertile, the greenhouses are abandoned after shredding; these are reported to enter the Mediterranean Ocean (Tremlett, 2013). PE is the preferred plastic type for greenhouses because of its affordability, flexibility, and ease of manufacturing (Scarascia-Mugnozza et al., 2011). In this plasticulture area, most targets - such as soils, trees, and the greenhouses - depict a homogeneous appearance. However, most of the plastics are transparent or translucent with vegetation below.

4.4.2.2 City of Accra, Ghana, West Africa

The data of Accra (5°32'43.3"N 0°13'4"W, Fig.4.1f) were acquired on March 3, 2018. In Accra, the area of interest is located at the electronic waste dump site in Agbogbloshie. E-waste has become the fastest growing waste disposal in the world, with an annual growth rate of 3–4%. More than 150,000 tons of electrical appliances consumed worldwide are shipped to Ghana per year (Schluep et al., 2012) via the Port of Tema, located 20 miles east of the Agbogbloshie dump. Furthermore, the urban areas of Accra release about 760,000 tons of municipal solid waste per year (US, 2002). About 80,000 people subsist on the Agbogbloshie dump, living locally or nearby, and suffer from the contaminated environment. Only 15% of e-waste is recycled, of which the most significant constituents are plastics, accounting for up to 20% (Sahajwalla and Gaikwad, 2018).

4.4.2.3 City of Cairo, Egypt

The imagery of Cairo (30°2'35.1"N 31°16'56.3"E, Fig.4.1g) was recorded on January 29, 2019. Cairo is a typical urban area, with a compact and heterogeneous distribution of land cover types. The region is covered with garbage from the city center to the countryside, and from the streets to the roofs of the houses. The largest settlement is Mokattam village, with a population of around 30,000 humans, located at the foot of the Mokattam Mountains, next to Manshiyat Naser. The people living here - the Zabbaleen - have served as Cairo's informal garbage collectors since the 1940s, and are a key element of Cairo's waste management system. Some 9,000 tons (Guénard, 2013) of waste are brought here for disposal every day, 80% of which are recycled and turned into sellable raw materials (Woods, 2011) (Woods, 2011). The Zabbaleen live in impoverished conditions, especially as they live among the village's sorted rubbish and with their livestock. However, they have formed a strong and close-knit community.

4.5 Methodology

In this study, a classifier was developed based on the physical principles of spectroscopy and tested to automatically identify and cluster different plastic materials in WV-3 data. The general schematic of the overall flowchart for this study is illustrated in Fig. 4.2.

The strategy of spectral resampling to the spectral resolution of WV-3 band filter paths, based on the spectral response functions of the sensor, is presented in Section 4.5.1.

The evaluation of different plastic materials in terms of their spectral characteristics and their molecular structures is discussed in Section 4.5.2.

The rules and routines for the classifier were accordingly developed in Section 4.5.3, based on the theoretical analyses of the available spectral libraries. Hence, the spectra were sorted into four major clusters consisting of aliphatic plastics and two subgroups of aromatic plastics and non-plastics.

Finally, the performance of the classifier to detect different kinds, types, and fractions of plastics was examined by the calculation of confusion matrices on lab, and experimental and airborne data convolved to the WV-3 spectral response in Section 4.5.4.

4.5.1 Spectral resampling

To obtain a theoretical insight into the capability of the WV-3 instrument for the detection of different plastic materials, all library spectra, all experimentally derived spectra, and all airborne hyperspectral datasets are convolved to the SWIR spectral filter characteristics of the WV-3 sensor. Data with lower spectral resolution are simulated from higher spectral resolution using Eq.4.1:

$$R_i = \frac{\int_{\lambda_0}^{\lambda_1} SRF_i(\lambda)\, R_{lab}(\lambda)\, d\lambda}{\int_{\lambda_0}^{\lambda_1} SRF_i(\lambda)\, d\lambda} \tag{4.1}$$

where
R_i is the i_{th} band of the lower resolution data,
$SRF_i(\lambda)$ is the measured spectral response of band i,
$R_{lab}(\lambda)$ is a measured radiance or reflectance of the higher spectral resolution data (van der Meer and De Jong., 2011).

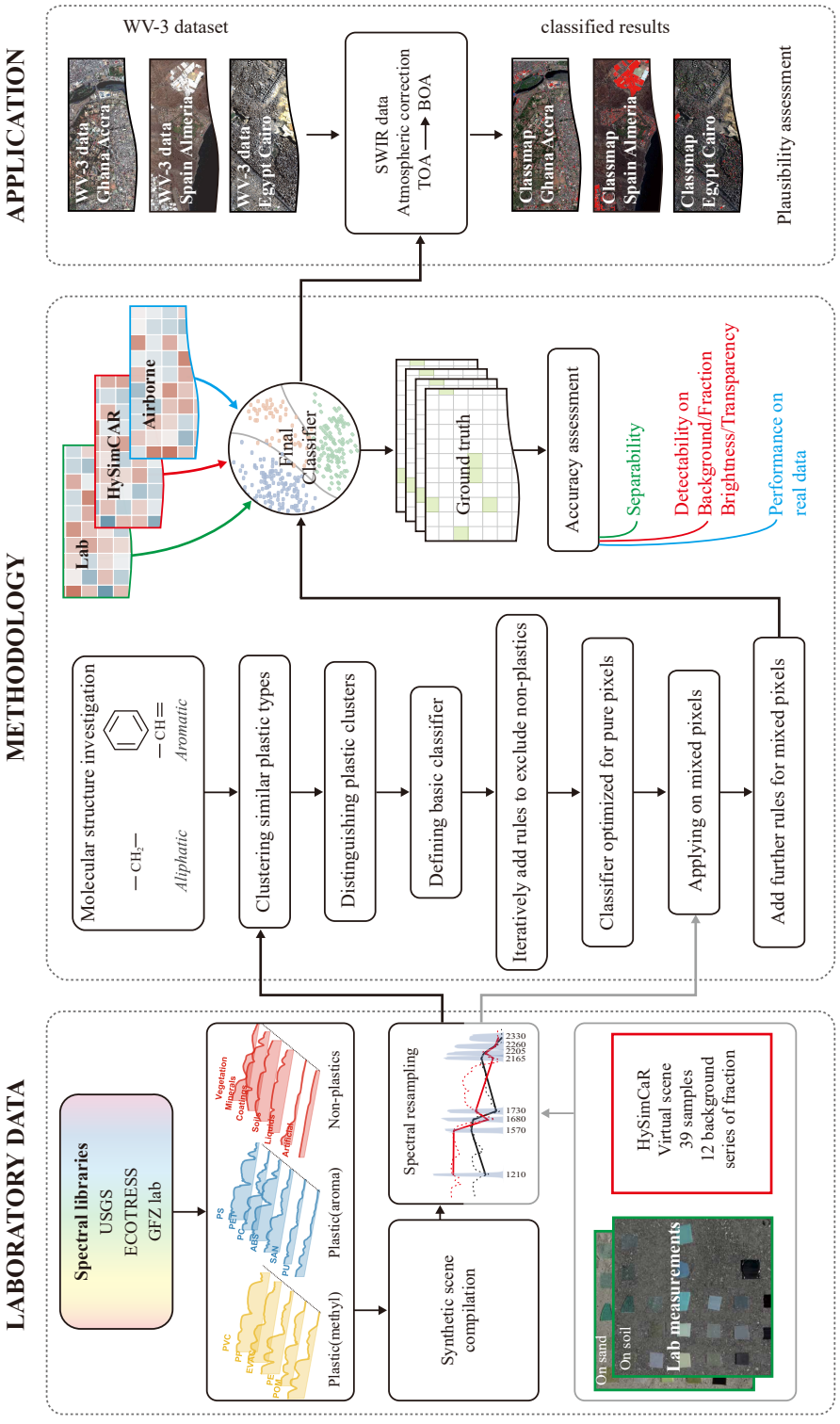

Figure 4.2: Schematic representation of the study design, including the data used, the data evaluation, the design of the classifier, and the application, TOA: top of atmosphere, BOA: bottom of atmosphere. See text for acronyms.

Fig. 4.3 shows the original high-resolution spectra of all plastic types investigated in this study combined with the resampled spectra.

4.5.2 Evaluation of the chemical bonds in plastics

Plastics are petroleum derivatives with the backbone of C-H chains and distinctive functional groups. Consequently, they display diagnostic spectral features in the SWIR range. There are further absorption features displayed in the VNIR range (400-1300 nm). However, most of these correspond to electronic transitions between pigment molecules and are excluded from the identification process for this reason. Plastics are polymerized with one-repeat units. Thus, due to their relatively simple molecular structure, their absorption features in the SWIR range are easier to explain than those of natural organic materials. Diagnostic absorption features displayed by plastics in the SWIR range are mainly controlled by the stretching vibration overtones and combination modes of C=O, C-C, and by hydrogen-containing functional groups (X-H), including O-H, N-H, C-H, and others (Schwanninger et al., 2011).

The general absorption features of the C-H bond in plastics (Fig.4.3) can be understood based on their mode assignments, including the 1^{st} and 2^{nd} orders of the overtone stretching modes (2ν: 1600-1800 nm, 3ν: 1100-1250 nm) and the combination modes ($1\nu_{Comb}$: 2150-2500 nm, $2\nu_{Comb}$: 1300-1450 nm). The 2^{nd} order of the combination mode is not contemplated in this study as it is masked by the overlay of the 1^{st} overtone of water (O-H) emerging at 1400 nm. This O-H band causes a lack of transparency in the atmosphere and generally prevents access by remote sensing techniques. All spectra of plastics depict a stair-like shape, with inflection points at the 1^{st} overtone and the combination band respectively. This is caused by a gradually decreasing absorptivity toward the higher order of overtones and combination tones.

The C-H bonds in plastics are not isolated but connected with distinct functional groups which have various masses and bond force constants. Due to the anharmonicity and Fermi resonance, vibration frequencies induced by C-H bonds do not fall within the same spectral band in all plastics. These spectral characteristics offer the potential to identify and distinguish between different types of plastic, based on their unambiguous spectral absorption features (Czarnecki et al., 2015; Beć et al., 2018). The correspondence of a spectrum and its vibration mode of C-H bonds is well investigated by both experiments and Density Functional Theory (DFT) simulations (Beć and Huck, 2019; Ma et al., 2019b).

Ma et al. (2019b) pointed out that the sp hybridization of CC bonds affects the diversity of absorptions for (C-H) substances. Sp hybridization can be described as an entanglement between s and p orbits of the outermost shell of the atom. Consequently, the plastic materials under investigation can be divided into two major clusters: aromatic polymers with benzene rings (sp2 hybridization, Fig.4.3a) and aliphatic polymers without benzene rings (sp3 hybridization, Fig.4.3b). The sp2 hybridization with a stronger bond force constant can induce a higher absorption frequency than the sp3 hybridization. The raw spectra of plastics without benzene rings produce second overtone absorptions at around 1210 nm and first overtone absorptions at 1730 nm. As far as plastics with benzene rings are concerned, absorptions emerge at higher frequencies in the second overtone range around 1140 nm, while the first overtone absorptions show a "blue shift" to around 1660 nm. In the range of the combination mode, a strong absorption feature appears around 2300 nm among aliphatic plastics, resulting from the combination mode of a C-H stretching and bending vibration. Plastics of the aromatic type have one more broad absorption

region related to C-H and C-C stretching vibrations in the combination mode, at around 2130 nm.

There are further explainable diagnostic features displaying in the highly resolving lab reflectance spectra sampled at 1 nm intervals like N-H (ν 2: 1517 nm) and C=O (νcomb: 2250 nm), but these are not unveiled in the simulated WorldView-3 spectra due to the diminished spectral resolution.

Yet, the spectral resolution in the range of the 1^{st} overtone and combination band is quite sufficient to distinguish aromatic plastics from aliphatic plastics, by clearly evaluating relevant absorptions and peaks as described. Looking further into the details of aromatic plastics, it is found that the position of the absorption peak of the 1^{st} overtone in PBAT, PU, and ABS shifts to longer wavelengths, along with a smoothing effect. The latter is caused by the low spectral resolution of spectra convolved to the WV-3 bandwidths, resulting in the disappearance of the absorption at 1660 nm. Hence, based on the variety of diagnostic absorption features studied, we are theoretically able to separate the investigated plastic materials into at least three different categories namely two clusters of aromatic and one cluster of aliphatic plastics.

4.5.3 Development of the classifier routines

A knowledge-based decision tree classification method, based on diagnostic absorption features of plastic materials caused by their molecular structure, is developed and applied. Although the basic features can accordingly be extracted, further constraints caused by the limited spectral resolution had to be researched empirically, based on the spectral libraries used.

The classifier works in several consecutive steps, which are presented in the following. Therefore, a "Normalized Hydrocarbon Index" (NHI) was developed in this study (Fig.4.4), based on the HI proposed by (Kühn et al., 2004), which gives the concavity or convexity of a curve at the point λ_B. The formula is provided in Eq.4.2. For NHI >0, the curve at λ_B is concave, the value indicating the relative absorption depth at the given wavelength.

$$NHI = 1 - \frac{R_B}{R_A + (\lambda_B - \lambda_A)\,\frac{R_C - R_A}{\lambda_C - \lambda_A}} \tag{4.2}$$

Fig.4.5 illustrates the entire routine of the algorithm and highlights the core theory-based steps in bold black fonts, while the additional empirical constraints are displayed in gray font types. The classifier starts with the separation of the aliphatic from the aromatic hydrocarbons, based on their opposite concavity at 2165 nm. Different routes for aliphatic and aromatic compounds are separated with dashed and solid frames. In the aliphatic group, only a single cluster is extracted while two routes are applied because of the influence of other materials in mixed pixels. Among the two routes, one has stricter requirement on the minimum at 1730 nm while the other gives tolerance to mixed pixels and applies a threshold (d1) of NHI at 1730 nm. Two clusters can be isolated in the aromatic group, based on their distinctive absorption features, such as the minimum at 1660 nm and the maximum at 2165 nm or 2205 nm. For these two clusters, the respective thresholds are introduced to give tolerance to mixed pixels.

To determine suitable threshold values, the evolution of balanced values for the "user's accuracy" (UAc) and "producer's accuracy" (PAc), namely the F1-score, was calculated along with the respective thresholds from 0 to 1 in steps of 0.01 (Fig.4.6).

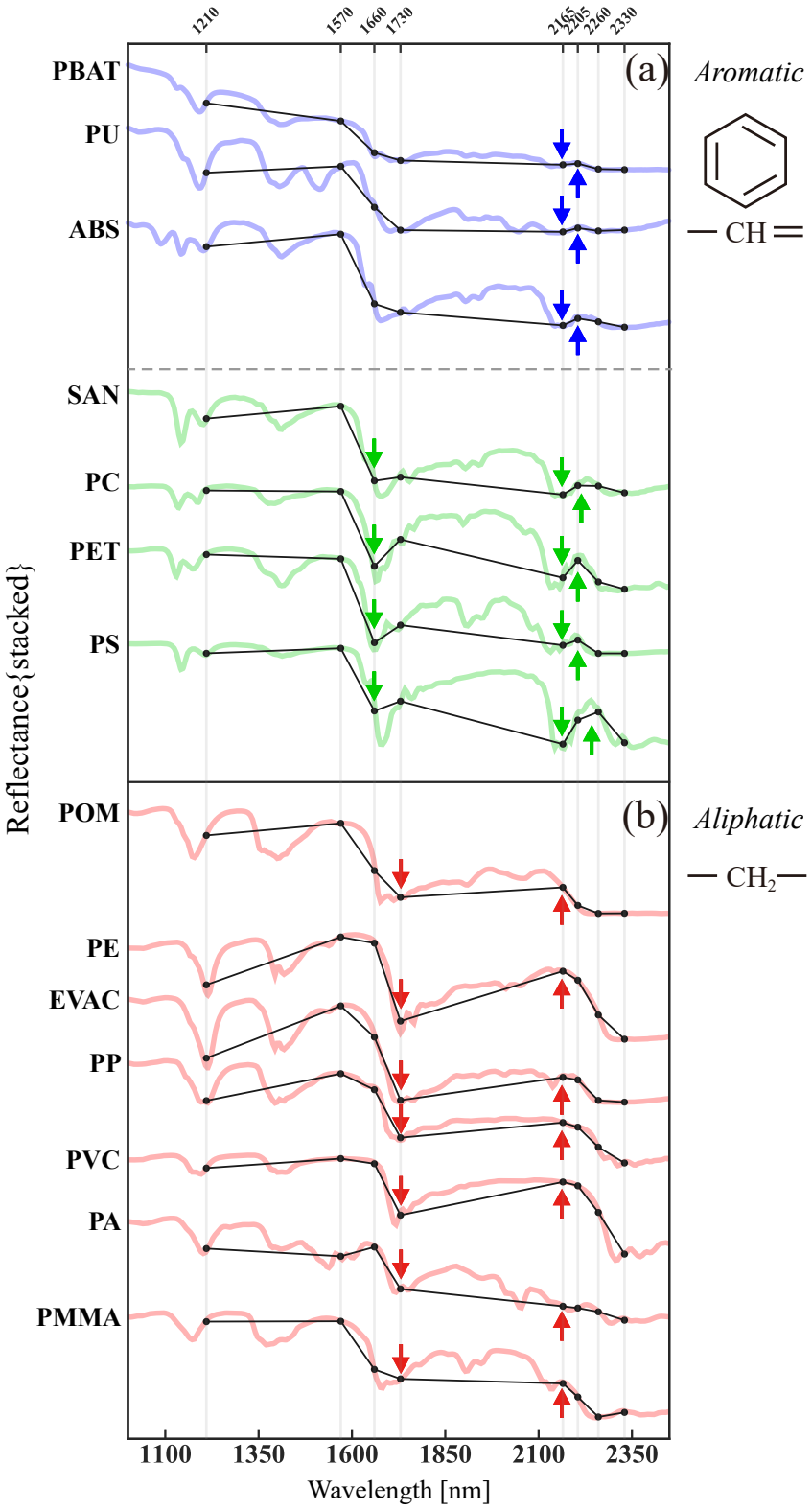

Figure 4.3: Stacked plot of reflectance spectra of various plastic materials investigated in this study. Laboratory-derived spectra (1 nm res.) are combined with their respective versions resampled to WV-3 band design. Upward pointing arrows mark bands with diagnostic peaks and downward pointing arrows indicate diagnostic absorption bands. Curves are offset and highlighted in three different colors for clarity.

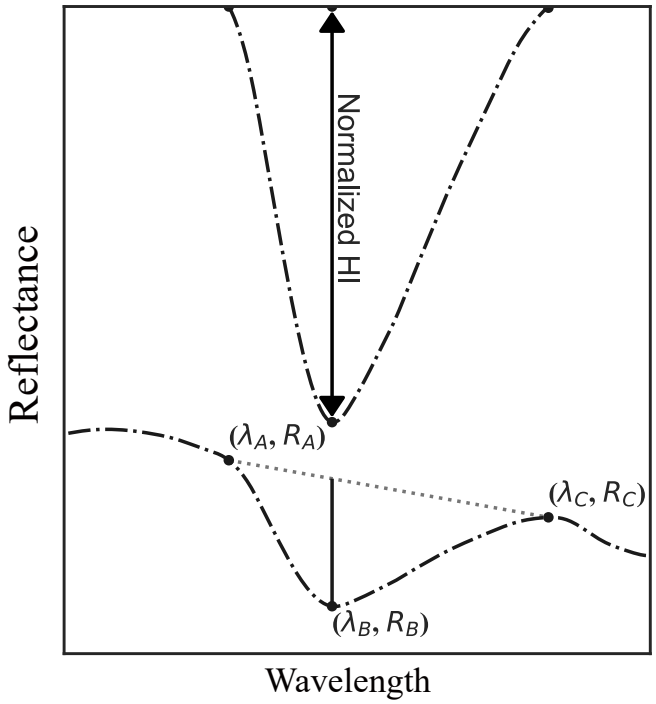

Figure 4.4: Schematic illustration of the Normalized Hydrocarbon Index (NHI) calculation by computing the absorption depth using a convex hull.

The figure illustrates that the classifier shows sufficient robustness in clusters 1 and 2, with F1-scores reaching the peak when the threshold is set to 0.02 and 0.05 respectively. For cluster 1, all possible thresholds result in a balanced accuracy of more than 80%, while, for cluster 2, a threshold lower than 0.5 is required to reach such a score. The robustness of the classifier on cluster 3 is relatively less desirable than that of the other two, with the F1-score peaking when the threshold of the classifier is set to 0.02. The F1-score surpasses the 80% level only when the threshold is set to 0.02 and 0.03. A low threshold value makes the classifier more sensitive for spectra, displaying only minor absorption band depth; however, vice versa, it becomes less robust against noise.

In this study, the threshold values for clusters 1, 2, and 3 are chosen as tradeoffs between sensitivity and noise to 0.1, 0.05, and 0.02 respectively. Nevertheless, the threshold values for clusters 1 and 2 can be adapted flexibly.

4.5.4 Evaluation of lab and airborne data

The sensitivity of the proposed classifier in respect of varying abundances/fractions of plastics and the respective background materials is assessed on datasets produced by the HySimCaR model (Kuester and Bochow, 2019). In total, the detectability of 39 samples with the most-used plastic types (HDPE, PVC, PS, PP, PET, PBAT) in different physical properties are examined on 12 backgrounds with fractional covers of 0 to 100% in 42 steps. The background materials for the simulation were asphalt, concrete, bright sand, dry soil, wet soil, peat soil, dry grasslands, vital grasslands, vegetated areas, Baltic Sea, River Po, and River Elbe. Confusion matrices were calculated in accordance with ground truth maps

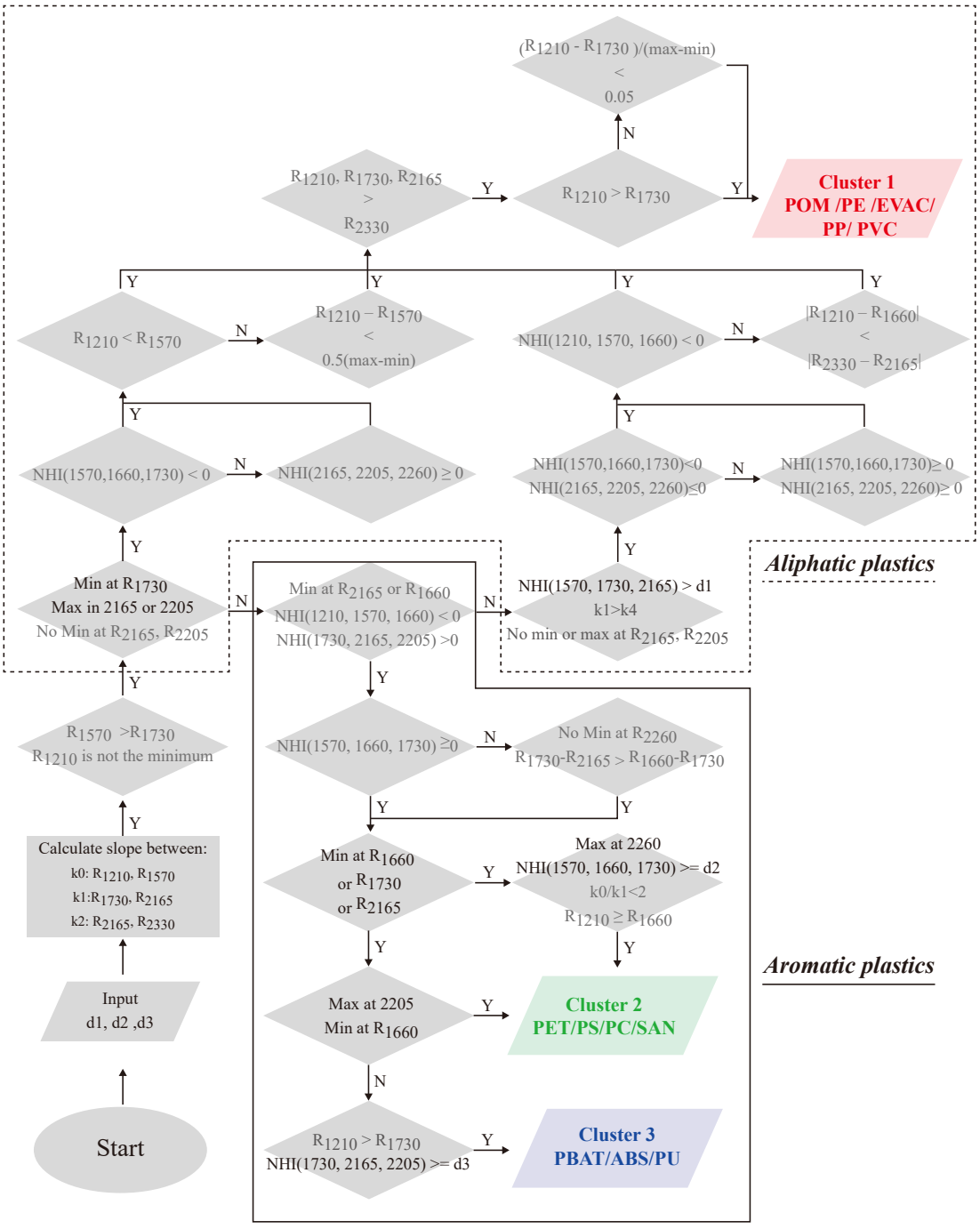

Figure 4.5: Flowchart of the developed knowledge-based classifier routine. k: slope; d: input thresholds.

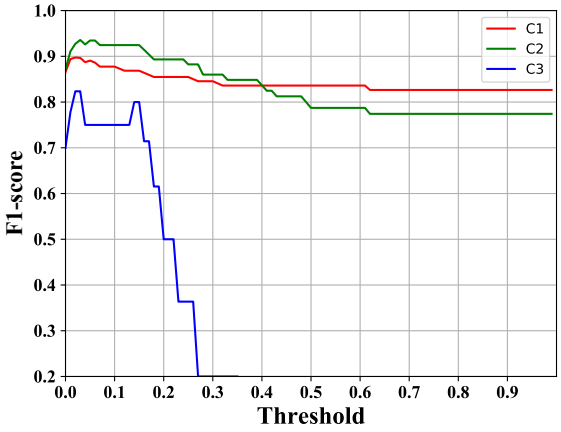

Figure 4.6: F1-score versus threshold curves for the three detectable clusters. Red = cluster 1, green = cluster 2, and blue = cluster 3.

(see details in Section 4.4.1) to evaluate the potential of the classifier to detect plastics in the lab and airborne datasets. The performance of the classifier is demonstrated using producer's accuracy (PAc, i.e. precision), user's accuracy (UAc, i.e., recall) as well as the overall accuracy (OAc). To assess the level of agreement and reliability of the classifier, Cohen's kappa coefficient was computed. In addition, the F1-score - which calculates the harmonic balance of UAc and PAc - was used to avoid bias from imbalanced ground truth. Due to the problematic of ground truthing concerned with the totally inhomogeneous substance of the (plastic) garbage at the Accra and Cairo sites recorded by the WV-3, the plausibility of results derived from WV-3 imagery is assessed via ground images instead of mathematical accuracy.

4.6 Results and discussion

4.6.1 Classifier performance for spectral libraries and measured lab data

Table 4.4 shows the confusion matrix and accuracy metrics for the classification of the spectral libraries (Section 4.3.1.1) In general, the PAc exceeds 80% for all classes, and the UAc exceeds 85% for non-plastic and for clusters 1 and 2. The F1-score is above 85% for all classes. More than 99% of the non-plastics can be excluded by the developed classifier, which means on the basis of 3,391 non-plastic samples in total, only 14 samples are falsely recognized as plastics. It is, therefore, noteworthy that the errors arise almost only as false negatives, which are almost equally distributed among the three plastic clusters (10 to 15%). There are only minor misclassifications among the three plastic clusters, which leads to the conclusion that the classifier can separate these three clusters based on lab spectra very well.

Fig. 4.7 illustrates the setup of the lab experiments that were conducted. Several plastic materials of different chemical and physical properties were placed on (a) bright sand -, and (b) dark soil backgrounds and measured by the HySpex sensor. The top row shows SWIR color composites (a, b) of the setup, while the bottom row depicts the results derived by the developed classifier (c, d). Each column represents a series of samples of one/two type(s) of plastic material with different physical properties. Those selected (PE, PP, PS, PET, and PBAT) represent the three clusters discussed in Section 4.5.1, and

Table 4.4: Confusion matrix based on all spectra in all libraries (see Table 4.1). The values of the producer's accuracy are highlighted in bold. N: non-plastic cluster; C1, C2, C3: plastic clusters; UAc: user accuracy; F1: F1-score; OAc: overall accuracy; κ: Kappa coefficient.

Spectral library		**Ground truth (% accuracy)**				**UAc**	**F1**	**OAc**	κ
		N	**C1**	**C2**	**C3**				
Classes	**N**	99.59	15.27	4.55	0	99.44	99.52	99.07%	0.89
	C1	0.32	83.96	0	0	89	86.41		
	C2	0.03	0	95.45	0	97.67	96.54		
	C3	0.06	0	0	100	75	85.71		
Total		3391	106	44	6	-	-		

are marked as C1, C2, and C3. The white dashed grid lines are introduced to separate samples with individual parameters. Each row contains materials with the same physical properties like transparency, translucency, and bright/median/dark opacities.

The results of the classification clearly show that the black-colored samples in this experiment with average reflectances below 10% cannot be detected. This is on account of the too low reflectivity of the target, leading to an insufficient signal to noise ratio (SNR) and a severe quenching of the respective absorption features. All other plastic materials are clearly identified at the bright sand background as well as on the dark soil, regardless of their physical properties. There were only a few pixels found omitted within the transparent PP, PET, and PBAT materials, or misclassified when placed on black soil backgrounds. The calculated confusion matrices of the classification results on both backgrounds are given in Table 4.5. The producer's accuracy of all classes is over 99% on both backgrounds, except for C3 on dark soils. C1 reached 100% on both backgrounds as well as non-plastic on sand. As expected, all accuracy indicators (PAc, UAc, OAc, and F1) yields better results on bright sand than on dark soil, especially C3 with some omitted pixels. In general, both the Cohen's kappa coefficients (κ) are greater than 90%, proving that the classifier is very reliable.

The omission of transparent samples results from the low reflectance of the dark soil with averages of around 25%. According to Miller et al., 1992, the apparent reflectances of non-opaque materials over background substances can be derived from Eq. 4.3, where A is the apparent reflectance, r and t are the real reflectance and transmittance of the target, and r_b is the reflectance of the background.

$$A = r + t^2 r_b \tag{4.3}$$

Only the light that is not absorbed by an object can be reflected or transmitted. Hence, both transmittance and reflectance spectra of an object show the same absorption band positions and can be used to identify and ideally quantify the respective material. For highly transparent or translucent samples, the reflectance is very low; the identification of an object is mainly dependent on its transmittance, given by the second term of Eq. 4.3. Since the transmittance is less than 1, its square will be much smaller, and the magnitude of the background reflectance will determine whether the object will have enough

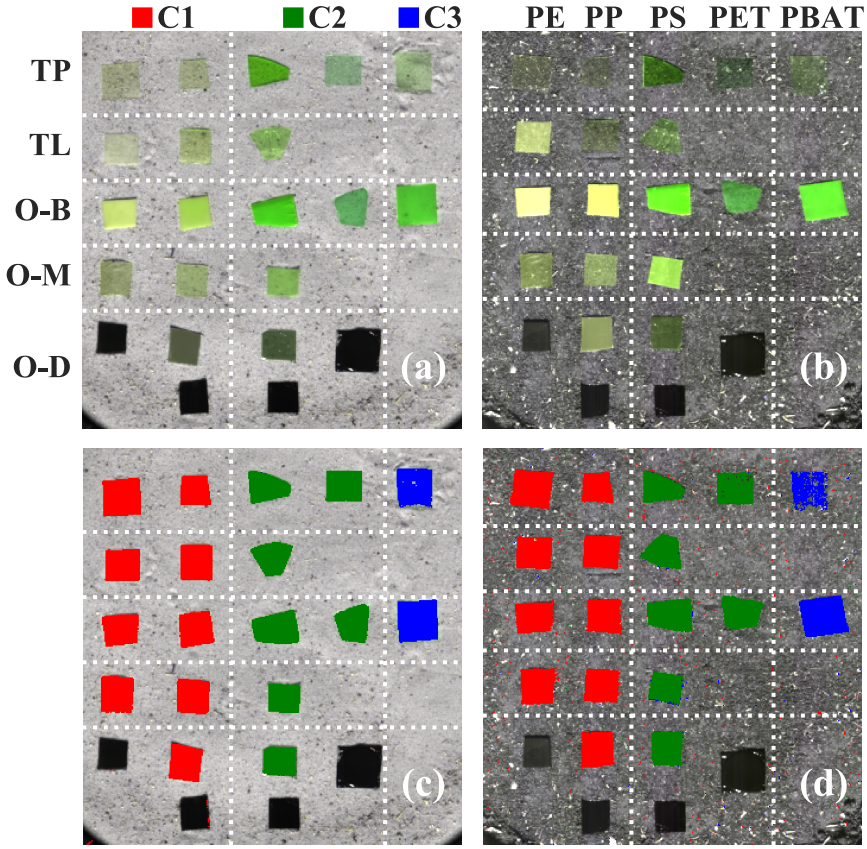

Figure 4.7: Images of the laboratory experiment. Various plastic materials of different physical properties were measured by the HySpex sensor placed on bright sand (a) and dark soil (b) backgrounds. Results of the classification for (a) are shown in (c), and for (b) depicted in (d). C1=PE/PP; C2=PS/PET; C3=PBAT. TP: transparent; TL: translucent; O-B: opaque bright; O-M: opaque medium; O-D: opaque dark. Measured SWIR-bands of the HySpex sensor were convolved to spectral characteristics of the WV-3 spectral bands. Bands 1730 nm, 1570 nm, and 2205 nm coded RGB.

Table 4.5: Confusion matrices of classified plastic materials measured during a lab experiment on bright sand and dark soil backgrounds. The values of the producer's accuracy are highlighted in bold. N: non-plastic cluster; C1, C2, C3: plastic clusters; UAc: user accuracy; F1: F1-score; OAc: overall accuracy; κ: Kappa coefficient.

a. Sand		**Ground truth (% accuracy)**				**UAc**	**F1**	**OAc**	κ
		N	**C1**	**C2**	**C3**				
Classes	**N**	100	2.87	2.55	5.06	99.98	99.99	99.98%	0.99
	C1	0	100	0	0	100	100		
	C2	0	0	99.9	0	100	99.94		
	C3	0	0	0	99.27	100	99.63		
Total		62905	4844	3086	1653	-	-		
b. Soil		**Ground truth (% accuracy)**				**UAc**	**F1**	**OAc**	κ
		N	**C1**	**C2**	**C3**				
Classes	**N**	99.21	2.87	2.55	5.06	99.88	99.54	99.20%	0.96
	C1	0	100	0	0	93.24	96.5		
	C2	0	0	99.1	0	97.82	98.46		
	C3	0	0	0	94.85	89.03	91.84		
Total		69146	4857	2994	1087	-	-		

apparent reflectance to be recognized. Besides, the shape of the background reflectance also influences the apparent reflectance.

In summary, a material with a higher transparency will have a greater transmittance in the wavelength range with low absorption, and its apparent reflectance is proportional to the background reflectance. Hence, backgrounds have notable influences on the apparent reflectance, especially for transparent and translucent plastics, which are the most common plastics on the market. The analyses in relation to the lab experiments demonstrate that all three clusters of plastics can be differentiated well and separated from non-plastic materials, indicating that the classifier designed shows the expected performance. As for the classification of the spectral libraries, the only errors represent false negatives, which can be attributed to the low apparent albedo of the dark samples.

4.6.2 Classifier performance for simulated HySimCaR datasets

As a next step, the classifier was applied to simulated datasets, which include 39 samples on 12 different backgrounds, with 42 steps of surface cover fractions in the range of 0-100%. Based on the conclusions drawn in Section 4.6.1, no black opaque sample is considered in this assessment. To better visualize the results, a heatmap was generated (Fig. 4.8). The x and y axes represent different types of backgrounds and various samples of plastic materials. The backgrounds include two artificial materials (asphalt and concrete), four bare soils sorted from bright to dark and wet, three surfaces covered with vital and dry vegetation, and three water bodies.

Plastic materials are grouped in accordance with their optical behavior, as transparent, translucent, and opaque. The translucent and opaque samples are further grouped into bright, median, and dark species. The names of the samples are labeled in three col-

ors, where red, green, and blue respectively represent clusters 1, 2, and 3. The heatmap depicts the detectable fractional covers of the respective materials by the level of saturation of the blue color and guided by a color bar. I.e., the value on row i and column j indicates that from this fractional cover, the classifier is able to identify the i_{th} sample on the j_{th} background. According to the color bar, the less saturated the blue color, the lower the detectable fraction per pixel, and the higher the detectability of the particular plastic material on the respective backgrounds. The cross x implies that the i_{th} sample on the j_{th} background is not detectable.

On asphalt and concrete, almost all the translucent plastics can be identified at a relatively low fractional coverage. Among the transparent and opaque plastics, the transparent PBAT and PET samples and the two opaque dark PET samples could not be detected. The classifier exhibits a similar performance for most plastics on dry bright sands and dry soils. In contrast to other backgrounds, the detectability for all transparent plastics decreases when placed on darker soils or wet and peat soils, while it does not vary much for translucent and opaque plastic materials. On vegetated backgrounds, the classifier's detection ability is generally lower for nearly all types of plastic materials, where some remain completely unidentifiable.

For transparent plastics, there is a significant increase in the detectability at dry grass as compared to vital grass and vegetated canopies. Translucent and opaque plastics are also difficult to detect on areas covered by vital vegetation, which is especially obvious for medium and dark samples as well as for the white opaque PVC. As for the three bodies of water, most of the transparent plastics could not be identified because of the strong absorption of water in the SWIR wavelength range. Surprisingly, most translucent and opaque plastics can be identified, especially cluster 1 materials, even at very low abundances.

It is also of interest to note that the brightness of the samples on the water surface has a relatively large influence on the detectability, as the minimum abundance to identify bright and medium samples is generally lower than that of dark ones. However, in this simulation study, it was assumed that the plastic objects float on the water surface and are not covered by water at all.

Overall, the classifier is able to detect plastics at relatively low abundances below 10% when located on top of artificial materials, bright sand, and water, while a higher fractional cover is required for successful identification over dark soil and vegetated surfaces. For those samples with similar optical properties, more fractional coverage is usually expected to recognize the second and third clusters of plastics as compared to the first cluster. In summary, the classifier shows a robust performance for the recognition of a majority of plastic materials at various fractional covers on most backgrounds, but also depicts inadequacy in recognizing transparent plastics on top of water bodies.

4.6.3 Classifier performance for airborne and WorldView-3 imagery

A further test for the developed classifier to detect plastics is carried out on four airborne hyperspectral datasets convolved to WV-3 spectral properties, acquired in Germany and Spain. The ground truth map and the classification results are highlighted in Fig. 4.9.

The non-plastics, and the plastic clusters 1, 2, and 3, are represented as patches in yellow, red, green, and blue. Table 4.6 presents the confusion matrices of the classification results for an urban site (Dresden), a grassland area (Thyrow), a lake and its shore (Seddin), and a greenhouse farming region (Almeria).

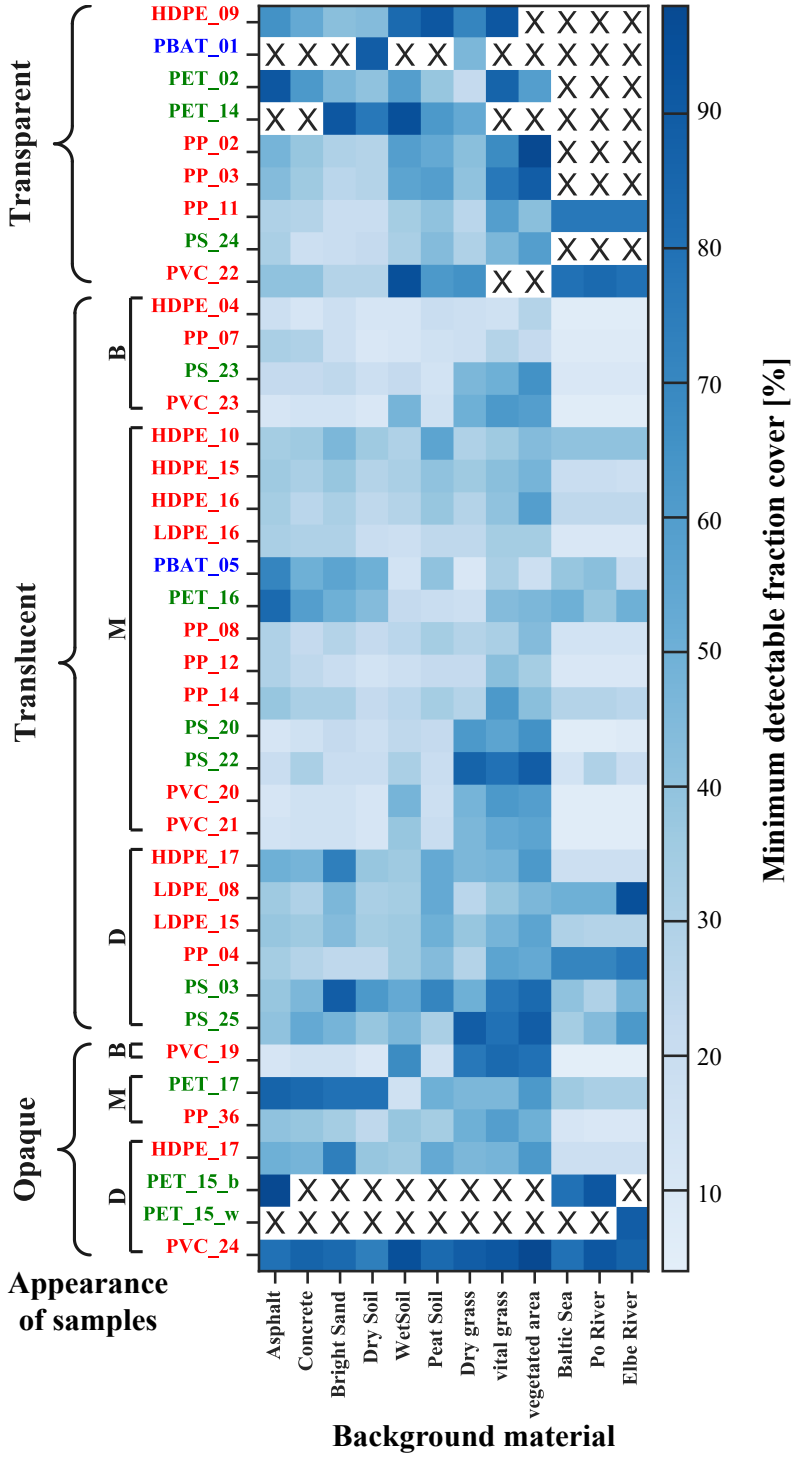

Figure 4.8: Display of detectable fractional covers of 39 individual plastic materials with different physical properties on 12 different backgrounds. The strength of saturation of the respective blue color marks the percentage of plastic parts per pixel that is detectable. The less saturated the blue color, the lower the detectable fraction per pixel and the higher the detectability of the particular plastic material on the respective backgrounds. X: Undetectable. Abbreviations of plastic materials belonging to cluster 1=red, cluster 2=green, and cluster 3=blue.

Table 4.6: a-d. Confusion matrices of four classified airborne data sets. The values of the producer's accuracy are highlighted in bold. N: non-plastic cluster; C1, C2, C3: plastic clusters; UAc: user accuracy; F1: F1-score; OAc: overall accuracy; κ: Kappa coefficient.

a. City of Dresden, DE		**Ground truth (% accuracy)**				**UAc**	**F1**	**OAc**	κ
		N	**C1**	**C2**	**C3**				
Classes	**N**	99.97	3.59	11.38	7.56	99.65	99.81	99.71%	0.96
	C1	0.02	96.41	0	0	98.92	97.65		
	C2	0	0	88.62	1.26	97.32	92.77		
	C3	0.01	0	0	91.18	99.45	95.14		
Total		29452	474	206	397	-	-		
b. Thyrow area, DE		**Ground truth (% accuracy)**				**UAc**	**F1**	**OAc**	κ
		N	**C1**	**C2**	**C3**				
Classes	**N**	100	2.87	2.55	4.67	97.62	98.80	98.67%	0.98
	C1	0	97.13	0	0	100	98.54		
	C2	0	0	97.45	0	100	98.71		
	C3	0	0	0	95.33	100	97.61		
Total		1679	348	705	257	-	-		
c. Lake Seddin, DE		**Ground truth (% accuracy)**				**UAc**	**F1**	**OAc**	κ
		N	**C1**	**C2**	**C3**				
Classes	**N**	99.98	0	6.71	-	99.84	99.91	99.83%	0.97
	C1	0	100	0	-	100	100		
	C2	0	0	93.29	-	99.29	96.2		
	C3	-	-	-	-	-	-		
Total		6360	30	149	-	-	-		
d. Almeria, ES		**Ground truth (% accuracy)**				**UAc**	**F1**	**OAc**	κ
		N	**C1**	**C2**	**C3**				
Classes	**N**	100	10.24	-	-	99.64	99.82	99.65%	0.94
	C1	0	89.76	-	-	100	94.6		
	C2	-	-	-	-	-	-		
	C3	-	-	-	-	-	-		
Total		449989	15884	-	-	-	-		

The urban and grassland sites contain all three clusters of plastics while in the remaining two sites, only two clusters of plastics are present. The user accuracies of all classes exceeded 97% in the urban and grassland areas, and the producer's accuracy reaches more than 95% for all classes except the second cluster of plastics in Dresden.

For the first cluster of plastics, present in all scenes, the classifier performs best in the Thyrow area - with a F1-score over 98% - and worst for the Almeria site (with a F1-score of 94.6%). This is in accordance with the conclusions obtained in the previous section, based on the simulated data. The plastic covers of the greenhouses in Almeria are mostly translucent and on top of vegetation, where the classifier performs in a less robust manner at low fractional covers.

Another reason for the less good result in identifying the plastic sheds of the Almeria site may be found in whitewashing procedures taking place in June where greenhouses are not necessarily cultivated. This procedure, done to prepare for the next season by reducing the radiation penetrating the plastic sheds, can mask the optical properties of the plastic.

The producer's accuracies of the classification results for the second cluster of plastics are 97%, 93%, and 88% respectively for grassland, lake, and urban areas. It is further noticeable that the kappa coefficients of all four scenes exceed 0.9, illustrating the performance quality of the classifier. The results also depict that there is no omission for the three plastic clusters, and the user's accuracies of the backgrounds all reach more than 95%, while the producer's accuracies all achieve 99%. The accurate identification of the second cluster of plastics over the lake surface suggests that the classifier also holds great potential to be applied to monitor floating non-transparent litter in the ocean. In summary, the classifier is well capable of identifying defined clusters of plastic in both homogeneous and heterogeneous areas, even when the used hyperspectral airborne data are resampled to the moderate spectral resolution of the WV-3 satellite.

Finally, the classifier was applied to three WV-3 datasets to examine its potential for identification of the three plastic clusters and their separation from different background materials. The three recorded WV-3 scenes are displayed as color composites and as panchromatic bands both superimposed by the results of the classifier (Fig. 4.10). In the first column the sites of Almeria (Fig. 4.10a), Accra (Fig. 4.10d), and Cairo (Fig. 4.10g) are displayed in overview mode based on SWIR bands, while the second column (Fig. 4.10b, e, h) shows enlarged sections of the respective imagery merged with the panchromatic band of WV-3 (0.31 m GSD) for a more detailed inspection. For plausibility assessment, photographs of the sceneries are displayed in the third column.

As expected, plastic materials of cluster 1 are most widely distributed in the three regions, especially in the area of Almeria, where PE or PVC plastics are generally used for greenhouse sheds (Scarascia-Mugnozza et al., 2011). The classification layer reproduces nearly exactly the shapes of the greenhouse sheds and depicts no to minor misclassifications for soils and vegetated areas in the surrounding (Fig. 4.10a, b). The classification result of the Accra site (Fig. 4.10d, e) shows mainly plastic materials of clusters 1 and 2. The local waste mainly consists of worldwide discarded electronic devices, which contain a wide variety of plastic materials (Guénard, 2013). The enlarged view focuses on the Korle Lagoon fed by the Odaw river, where the dumped, floating trash is dammed by a levee, located in the middle at the bottom of the image (Fig. 4.10e). Further visual verification can be made comparing the situation depicted by the imagery with a corresponding local photograph of the levee in a southerly direction (Fig. 4.10f, `http://marikeenimages`

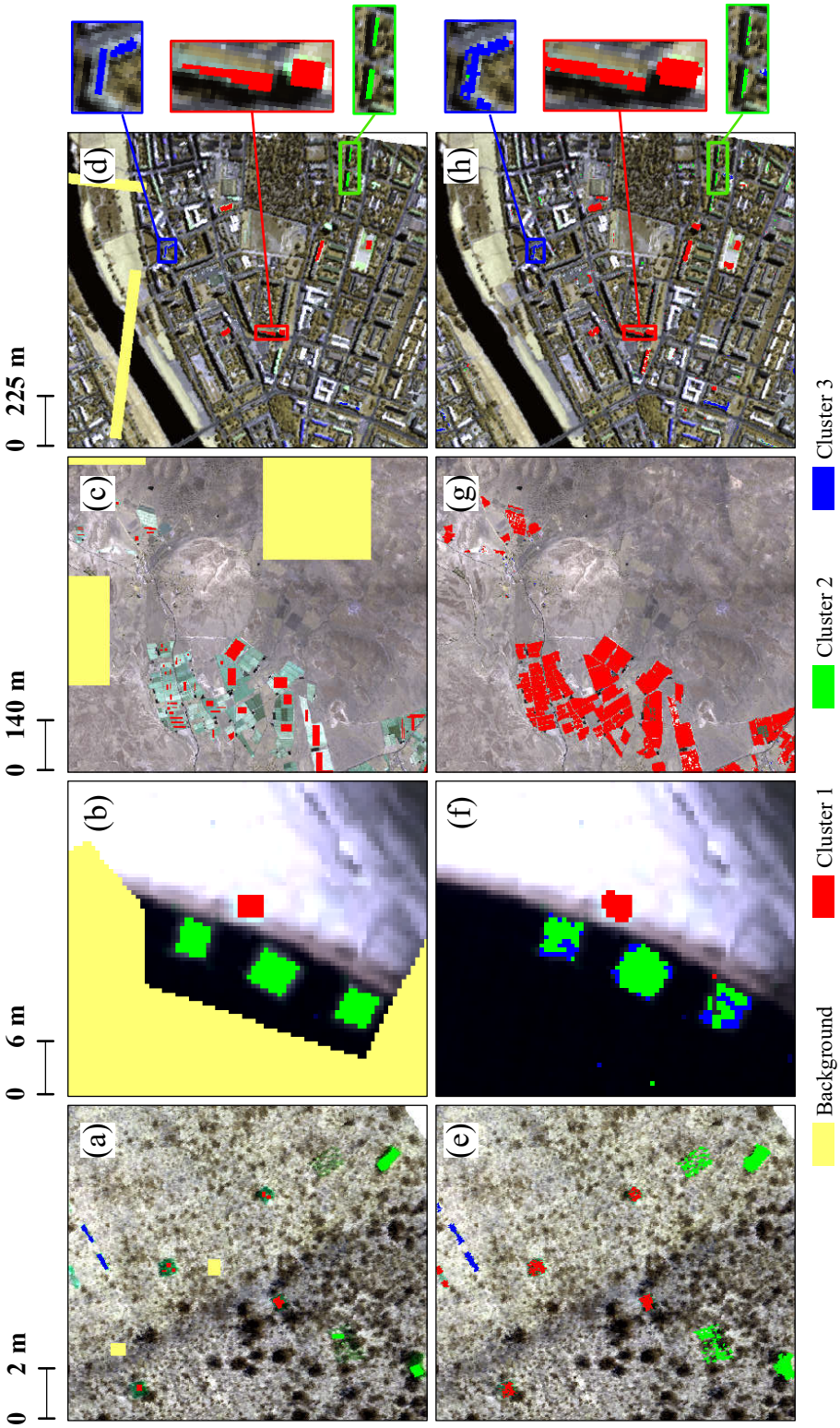

Figure 4.9: Color composites of convolved SWIR bands recorded by the airborne hyperspectral instruments HySpex (a, b) and HyMap (c, d), displaying various plastic materials on four different background surfaces. a: Grasslands (Thyrow, DE); b: Lake and shore (Seddin, DE); c: Soils (Almeria, ES); d: Urban surfaces (Dresden, DE). Ground truth targets marked with the resp. cluster materials and non-plastics are depicted in (a, b, c, and d). Classified clusters are displayed in (e, f, g, and h) underlain by color composites of SWIR bands convolved to WV-3 spectral response. Bands 1730 nm, 1570 nm, and 2205 nm coded RGB.

.blogspot.com/2014/03/14_17.html). The photograph of the inhomogeneous waste also illustrates the difficulty of collecting meaningful ground truth data for validating the result of the classification. For further inspection, Google Maps (https://goo.gl/maps/XiUWK7HiWyyf38yT7), and photos uploaded by people to the Web can be consulted.

The classification result of the vicinity of Mansheya Nasir in Cairo (Fig. 4.10h), displays plastic materials belonging to all clusters with greater emphasis on cluster 1. The area - known as "garbage city" - is home of the Zabbaleen people who recycle 80% of the waste in Cairo. They sort the gathered plastic materials and usually store the plastic garbage in residential areas on the roof of their houses as illustrated by the ground photograph (Fig. 4.10i, https://www.flickr.com/photos/pegmcglinch/4260237601/). Inspection of the panchromatic image superimposed with the classification result already reveals this situation (Fig. 4.10h). The classification layer marks all three clusters of plastic mainly on the top of the resolved houses, further marks the artificial lawn of two larger soccer fields (https://goo.gl/maps/9nK4SkkcYBpMyXHK7) in the top-middle of the image and shows no or only minor misclassifications in the areas of the vegetated park in the image center nor on the shoulder of the rocks in the east. For further inspection use Google Street View images (https://goo.gl/maps/gPCWNgsN76uRtGVz9) and media reports (e.g., https://www.atlasobscura.com/places/garbage-city). The results further indicate the potential of the developed classification routine for the detection of different plastic materials at lower spatial resolutions, as provided by satellite recordings.

4.6.4 Comparison to commonly used algorithms

There is an increasing high number of various algorithms used for supervised or unsupervised classification of remotely sensed data. Although all the different methods are not comparable, we like to demonstrate how other commonly used algorithms perform in comparison to our spectra-based approach. Therefore, we chose two supervised classifiers embedded within the ENVI/IDL environment. One is the Spectral Angle Mapper (SAM) developed by Kruse et al. (1993), another the Maximum Likelihood Estimation (MLE) published by Richards (2021).

Three of our scenes were used for the testing, including the lab experiment on the sandy background (Fig. 4.7a), and the airborne recordings of Thyrow and Dresden (Fig. 4.9a, d). In each of these scenarios all three clusters of plastics are present, and all sites are fully controlled by ground truthing. The ground truth maps were divided into two parts for training and testing respectively. Pixels of non-plastics are not included in the training datasets due to the huge interclass variation. We did not apply the algorithms to the real WorldView-3 datasets on account of already discussed ground truth issues.

SAM is a signal-based spectral classification method that matches pixels to reference spectra using an n-D angle. The algorithm determines the spectral similarity between two vectorized spectra (reference and unknown) by calculating the angle between them. Pixels with smaller angles are more likely to match the reference spectrum while pixels further away than the specified maximum angle threshold in radians are not classified. A primary advantage of this method is the insensitivity to illumination conditions. It is further notable that reference spectra used by SAM can come from spectral libraries or need to be extracted directly from the respective image. Using spectra of libraries as training data is more comparable to our classifier, but to understand the optimal performance of SAM, we also used the training part of the images as reference data set.

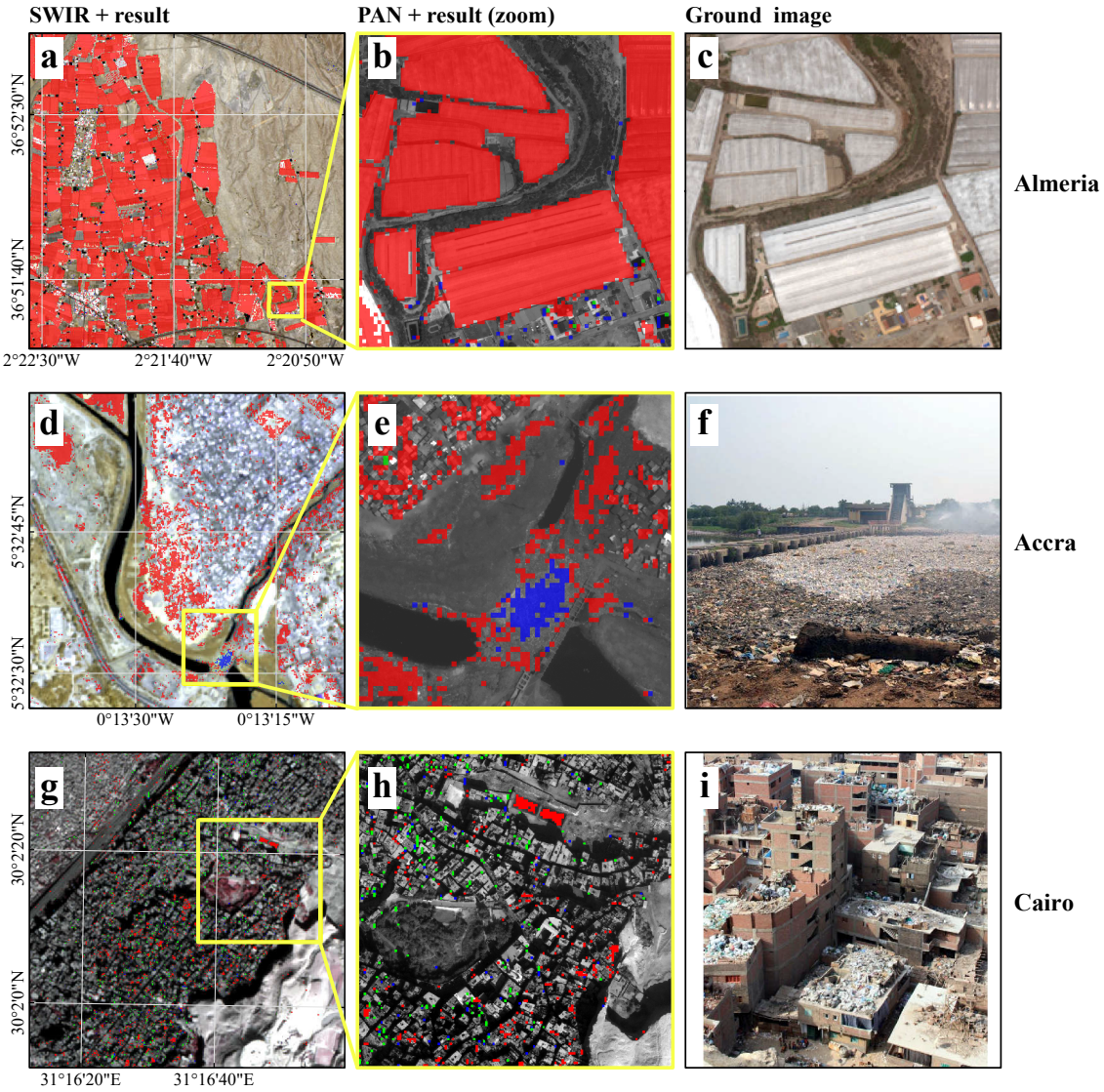

Figure 4.10: Classification of plastic materials in WorldView-3 data of (a-c) Almeria, Spain, (d-f) Accra, Ghana, West Africa and (g-i) Cairo, Egypt. Left column (a, d, g): SWIR color composites with superimposed classification result; SWIR-bands 1730 nm, 1570 nm, 2205 nm coded RGB. Middle column (b, e, h): Panchromatic images with superimposed classification results. Right column (c): high-resolution real color merge; (f, i): Local photographs. Classification result: Red = c1 - aliphatic group, green = c2 - aromatic group (PET, PS, PC, SAN), blue = c3 - aromatic group (PBAT, ABS, PU).

The performance was evaluated by calculating the F1-score of the classification result at a series of maximum angle thresholds in steps of 0.01 ranging from 0 to $\pi/2$ ($\approx$1.5). Fig. 4.11a-c show the F1-scores of the three sites versus threshold curves obtained from the classification results using the spectral library as training data. The three plastic classes and the one non-plastic class are represented by graphs in different colors. It demonstrates that the performance of SAM is highly influenced by the threshold value. When a proper threshold is selected, the F1-score of non-plastics and cluster 1 plastics can be higher than 90%, whereas cluster 2 and cluster 3 plastics score lower than 80% in any case. Especially in the Dresden scene, the cluster 3 plastic cannot be identified. Fig. 11d-f depict the results using spectral samples generated from image data based on our ground truth maps. The results are dissimilar to those in Fig. 11a-c, which illustrates that the choice of training data also has a significant impact on the results. Both approaches of SAM calculations indicate that the optimal threshold value varies with the respective scenarios and classes.

The MLE assumes that the statistics for each class in each band are normally distributed and calculates the probability of a given pixel belonging to a specific class. Each pixel is assigned to the class that has the highest probability, namely, the maximum likelihood. If the highest probability is smaller than the specified threshold, the pixel remains unclassified. Due to the necessity of distributed information, only spectra derived from the image data could be used as training data. Similarly, we examined the performance of MLE by calculating the F1-score of the classification result at a series of probabilities ranging from 0% to 100%. Fig. 4.11g-i display the result based on the same ground truth maps used for the SAM calculations. It implies that the performance of the MLE does not meet the demand at all three scenarios.

Comparing the results derived from these three scenes with our knowledge-based classifier (Lab-sand: Table 4.5a; Thyrow: Table 4.6b; and Dresden: Table 4.6a), the F1-scores for each class is above 0.9 when using the same ground truth maps, thus, indicating a superior performance. The evaluation of our classifier also demonstrates its robustness, i.e., the scenario and classes have little effect on the results and no training data is needed. The SAM performs moderately by the use of spectral library data but unsatisfactory like the MLE approach if image data is to be used as a reference. In the latter case, the accuracy of the classification is highly dependent on ground truthing, but this was very carefully accomplished for the selected scenes. The field check becomes all the more complicated when the focus is on plastic waste where a meaningful mapping is almost unfeasible (see photographs of Fig. 4.10). This is to some extent also true for popular algorithms like machine learning and deep learning as they also rely on training datasets and require parameter tuning.

Certainly, statistically based classifiers provide a convenient and general option for nearly every material once reliable training data are available. As for the here developed classifier, one has to carefully examine the spectral behavior of the targeted material with its physical background, which may take some efforts. But once the classifier is designed, it's trustful and robust and no pre-knowledge of the areas under consideration is needed.

4.6.5 Final assessment of the developed classifier routine

The performance of the classifier in detecting different plastic materials was evaluated on various backgrounds, including grasslands, water bodies, farming regions, and urban areas, which are common scenarios in terrestrial remote sensing. The classifier obtained decent results at relatively low fractions of plastics on all background materials and, so, provided

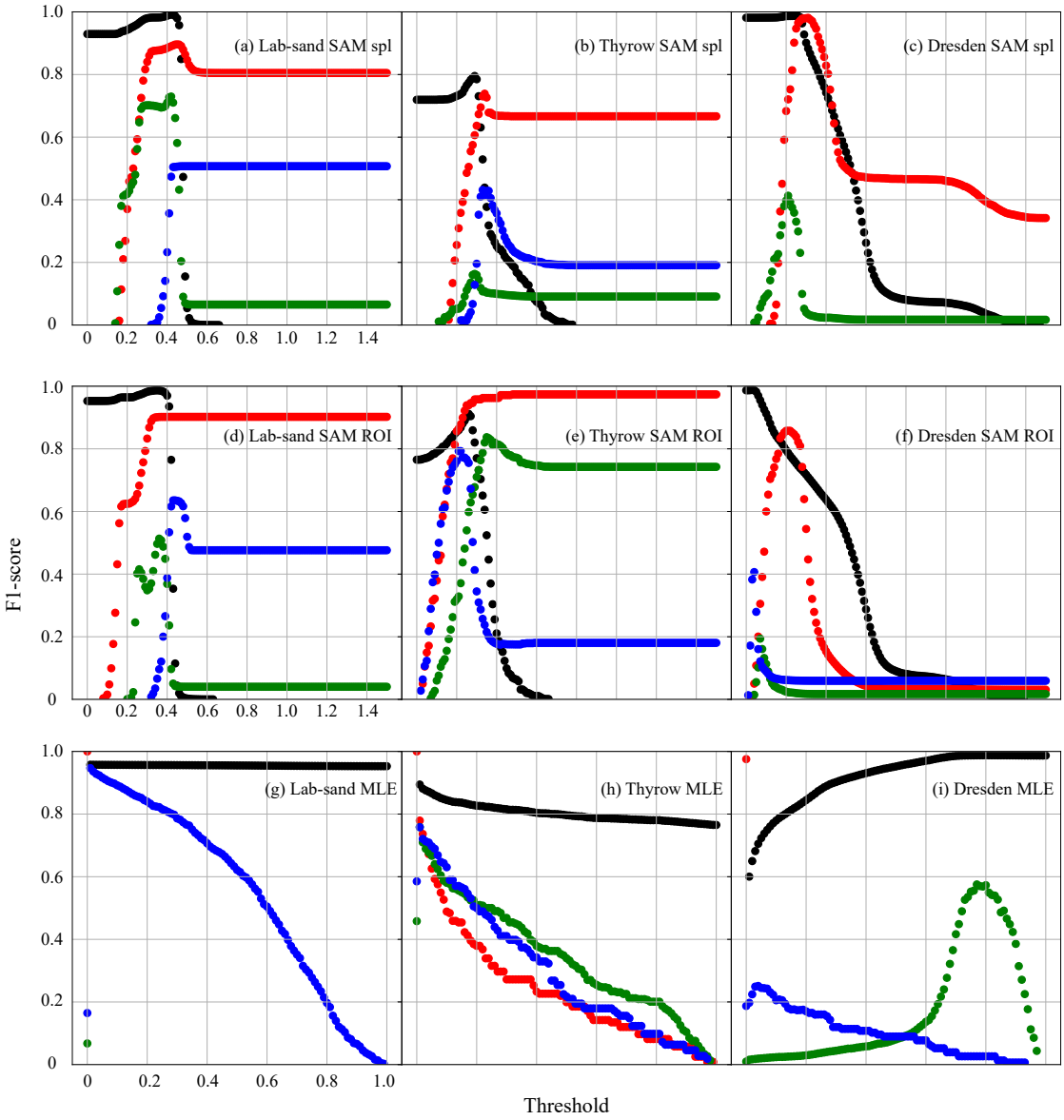

Figure 4.11: F1-score versus threshold curves for three selected test sites. SAM classification results based on training data from the spectral library (a-c); and from ROIs (d-f). MLE classification results using training data from ROIs (g-i). Black = non-plastics, red = cluster 1, green = cluster 2, blue = cluster 3.

an efficient and transferable concept for the global detection of plastics. Once set up by the respective spectral properties of the targeted material, it operates in an autonomous mode, and can be further combined with other exogenous data. All the requisite thresholds for the classifier are applied to indices or ratios and never directly to the reflectance values. This contributes to the transferability and robustness of the classifier and its results, and makes it unsusceptible to Bidirectional reflectance distribution function (BRDF) effects and artifacts introduced by atmospheric corrections.

However, with all advantages of the newly developed classifier, there are also a few limitations to be mentioned. In the present form it is dedicated to detect different types of plastic with a high accuracy and cannot detect any other materials. The principle scheme can be adapted to nearly any other materials, but with a different setup based on the respective spectral properties. Concerning the detectability of plastics, it is not sensitive enough to reveal black plastics with an averaged reflectance below 10%. In this case, hyperspectral thermal sensors are the first choice, since the fundamental vibrations of C–H bonds are located in the thermal infrared range (TIR), providing better preconditions for diagnosis as the emission of dark materials is generally high in this wavelength region. Furthermore, organic polymers with chemical compositions similar to plastics may be misclassified. For example, asphalt - as a type of methyl petroleum derivative - displays very similar reflectance spectra to that of plastic cluster 1. Although asphalt can be excluded by increasing the threshold value, pixels containing lower abundances of plastic would then not be identified as such. Therefore, the choice of threshold values needs to be balanced properly. Moreover, PBAT transparent samples of the simulated data could not be identified on the surface of the bright sand, which seems to be not quite consistent with the results obtained from our laboratory data. However, one possible influencing factor that we have not yet considered is the thickness. For thin plastics, the light travels a rather short distance inside the material, which reduces the spectral absorption depth and, so, makes them unrecognizable for the classifier.

The spectral absorption depth is positively proportional to the thickness, and, thus, it is important to consider the effect of thickness for quantitative studies of plastics with transparent or even translucent materials. We have also not explicitly considered the degradation of plastics, which is usually accompanied by the breakage of chemical bonds, although a part of the samples used for the lab experiments and simulation study has been collected in the environment. This may lead to classification failure, although the developed classifier is constructed on the absorption features of the C–H bonds. For future research, it is planned to explore the quantification ability as well as further improvements of the classifier after considering the thickness and degradation phenomena of plastics, to broaden its application to other targets, and utilize the classifier to fuse with multi-source data to achieve additional intelligent recognition functions.

4.7 Conclusion

The results of this study clearly demonstrate that a worldwide identification and separability of terrestrial plastics with different chemical and physical properties is feasible by the use of WorldView-3 satellite imagery. The core element of this study is the newlydeveloped, decision tree style, knowledge-based classifier which was exclusively built to detect and identify most common plastics materials of the aliphatic and aromatic groups. The detectability of three distinct plastic clusters is totally based on theoretical considerations

concerning the detailed spectral characteristics of plastic materials in connection with their molecular structure. No training data is needed and no statistical approaches have to be accomplished. The algorithm can be adapted to further specific targets, but needs a new setup according to the spectral characteristics of the respective materials. The first cluster to be identified is the aliphatic group, comprising PE, PVC, EVAC, PP, POM, PMMA, and PA. The second and third clusters are diagnostic for the aromatic group, including PET, PS, PC, and SAN, separated from PBAT, ABS, and PU respectively. The non-plastic cluster comprising nearly all other natural and man-made materials is defined by the majority of spectra in the databases used. The hit ratio of the classifier is significantly high, and its robustness is proven by comparative analyses to SAM and MLE approaches and by our HySimCaR radiative transfer model which was used to calculate the influence of different factors like material characteristics, backgrounds, and fractional covers. The validation of the results based on spectra, the experiments conducted, and the modeled data was accomplished by the calculation of various error measures using confusion matrices. Concerning the airborne data, the validation is based on controlled field experiments and intensive field checks. But ground truth for plastics, especially for plastic waste cannot always be conducted in detail due to its nature and fast temporal relocation. However, when finally applying our classification scheme to the WorldView-3 datasets, the results appear reasonable and of similar significance to those of laboratory experiments and airborne investigations.

5 Plastic detection using GaoFen-5 and PRISMA hyperspectral satellite data

This chapter was published as:
Zhou, S., Kaufmann, H., Bohn, N., Bochow, M., Kuester, T., & Segl, K. (2022). Identifying distinct plastics in hyperspectral experimental lab-, aircraft-, and satellite data using machine/deep learning methods trained with synthetically mixed spectral data. *Remote Sensing of Environment*, 281, 113263.

5.1 Abstract

The growing production and use of plastics are becoming a serious progressive issue and people pay increasing attention to the effects of plastics on ecosystems and human health. The availability of hyperspectral data from space sensors inspired us to study the feasibility to detect and identify different types of plastics in aircraft -, Goafen-5 (GF-5) and PRISMA satellite data by means of deep -, and machine learning models trained with spectral signatures. In this context, various inhouse and public spectral libraries are used to create a comprehensive database with mixed pixels of different plastic and non-plastic materials. The endmembers of plastic types involved in this study are polyethylene (PE), polypropylene (PP), polyvinyl chloride (PVC), polyethylene terephthalate (PET) and polystyrene (PS), covering 95% of the global production. Additionally, some important varieties of industrial plastics types such as acrylonitrile butadiene styrene (ABS), ethylene vinyl acetate (EVA), polyamide (PA), polycarbonate (PC), and polymethyl methacrylate (PMMA) were included in the investigations. Different samples with varying optical properties (color, brightness, transmissivity) have been selected for each plastic type. As non-plastic materials we have chosen spectra of vegetation, rocks, soils and minerals contained in the public US libraries (ECOSTRESS and USGS). The number of spectra for the training of the deep learning and machine learning models was enlarged by a random linear mixing method and the resulting database was separated into a training and a test group for subsequent multi-label classification. Algorithms selected are a convolutional neural network (CNN), random forest (RF) and support vector machine (SVM). To investigate the transferability to any hyperspectral image data obtained by air-, and spacecraft sensors, we opted for a unification of the spectral response functions (SRF) and the spectral sampling intervals of all data. Validation is accomplished based on the test group of the spectral database, and tested by controlled laboratory and aircraft experiments recorded over surfaces with varying background materials. Results are further analyzed for the influence of different noise quantities and abundance levels. The performance of the three models is roughly balanced for the validation of the spectral data with an overall accuracy of 97%, 96%, and 95% for the CNN, RF, and SVM, models respectively. In the controlled lab experiments, various accuracy indicators, such as the recall rates and the comprehensive metrics F1-score, OA, and Kappa suggest the RF classifier as the most robust one, followed by the SVM and CNN models. As for the evaluation of the aircraft data from controlled experiments, the RF further outperforms the other two models, behaving most robustly and reliably against conditions with unknown plastics and unknown background surfaces. Thus, the RF was used to classify the ten types of plastics mentioned above in one GF-5 and two PRISMA satellite recordings of the same area. In comparison of both sensor systems, the RF produced high quality and transferable results for detecting plastic mainly related to greenhouses, sport fields, photovoltaic constructions and industrial sites that are discussed in detail in this paper.

5.2 Introduction

Since their widespread introduction in the 1930s, plastic products are increasingly dominating the market, due to their low weight, waterproofness, and durability characteristics (**?**). Over the past four decades, global plastic production has quadrupled (Geyer et al., 2017). However, its durability and longevity, as well as the improper disposal of plastics,

contributed to a considerable amount of accumulation in terrestrial and aquatic ecosystems (Derraik, 2002). This resulted in an extensive damage to wildlife (Uhrin and Schellinger, 2011) and its habitats (Madhvee et al., 2022). Further, more than 50% of plastics are intrinsically toxic (Lithner et al., 2011). Even when not toxic, plastic can absorb and accumulate other pollutants (Teuten et al., 2009; Rochman et al., 2013). The disintegration of plastic in the presence of ambient solar radiation releases the greenhouse gases methane and ethylene, contributing to climate change and global warming (Royer et al., 2018; Vishwakarma, 2020). Thus, the use of plastic and its pollution is becoming a more prominent issue as people pay more attention to the effects of plastics on ecosystems and human health (Rochman et al., 2013; Law, 2017).

Plastics, as petroleum derived products, are polymerized with single repeating units and have a backbone of C-H chains and unique functional groups. Their diagnostic absorption features in the optical wavelengths range are primarily controlled by stretching vibration overtones and combination modes of the C-H bond, which are mainly observed in the short-wave infrared (SWIR) (Schwanninger et al., 2011). By advancing the technology of hyperspectral imaging sensors in the SWIR range, recorded data with a variety of temporal, spectral, and spatial resolutions can be used to map the distribution of plastics in the environment in a qualitative and even quantitative manner (Moller et al., 2016).

Although the majority of plastic litter ends up in the oceans via miscellaneous routes, the sources of the marine plastic waste are found to about 80% at land and 20% are directly introduced into the oceans (Li et al., 2016). Therefore, regular global monitoring of terrestrial plastic debris is becoming increasingly important in order to prevent further pollution. Yet most studies focused on the differentiation of a variety of plastic types through infrared spectroscopy based on lab-measurements (Moroni et al., 2015; Knaeps et al., 2021; Moshtaghi et al., 2021; Topouzelis et al., 2021). Only a few studies have been conducted on the detection and identification of plastics on terrestrial surfaces by remote sensed data, mainly using hyperspectral imagers aboard aircrafts at a limited scale (Kühn et al., 2004; Heiden et al., 2007; Wetherley et al., 2017). Some researchers investigated the detection of plastic greenhouses using statistical classification algorithms based on multispectral data recorded by the Landsat-8 OLI sensor (Lanorte et al., 2017; Aguilar et al., 2020) or by the Sentinel-2 MSI system (Sun et al., 2021). Others utilized super-spectral images recorded by the spatially high-resolution Worldview-3 satellite sensor (SWIR ground sampling distance (GSD) 3.7 m) and proposed methods for one-class index-based plastic detection, such as the relative absorption band depth (RBD) (Asadzadeh and de Souza Filho, 2016) or for the identification of certain chemical groups of plastic (Zhou et al., 2021). However, the limited number of wavebands offered by multi-, and super-spectral satellite sensors can hardly distinguish between each single plastic type.

The recent development and employment of hyperspectral satellite sensors is a further step ahead in this context. For example, the Chinese meteorological satellite GAOFEN-5 (GF-5) was launched in 2018 and provided data at the same wavelength range and spectral resolution as Hyperion but at a swath of 60 km (Liu et al., 2019)(Liu et al., 2019). A second GF-5 system with the same specifications was launched in September 2021. A further hyperspectral system, the PRecursore IperSpettrale della Missione Applicativa (PRISMA, Cogliati et al., 2021) was launched in 2019 by the Italian Space Agency. It carries a hyperspectral imager covering the same wavelength range at a similar spectral resolution as Gaofen-5, providing a swath width of 30 km and is additionally equipped with a panchromatic camera offering a spatial resolution of 5m x 5m. Future upcom-

ing instruments providing hyperspectral data from space are Germany's Environmental Mapping and Analysis Program (EnMAP) launched April 1, 2022 with comparable technical specifications to PRISMA (Guanter et al., 2015) followed by the Surface Biology and Geology (SBG) system from the US (Cawse-Nicholson et al., 2021), the European (ESA) built Copernicus Hyperspectral Imaging Mission for the Environment (CHIME, Rast et al., 2019), and the Spaceborne Hyperspectral Applicative Land and Ocean Mission (SHALOM, Israel/Italy, Feingersh and Dor, 2015) with some varying technical specifications.

This recent increasing availability of hyperspectral satellite data provides the potential to differentiate plastic targets on a larger scale in multitemporal mode, and allows the identification of more types of plastics due to its sensitivity to the subtle variations in their absorption features, especially in the SWIR wavelength range. However, the recently operating hyperspectral space sensors can only provide data at a GSD of 30 m. Therefore, especially in terms of plastics, even larger congregations of plastic waste might not be detectable from space as they generally exhibit a sparse and small-scale distribution. Plastic garbage has been detectable in detail by WorldView-3 data with a GSD of 3.7 m, but due to the limited number of bands and the broader band widths, only chemical groups of aromatic and aliphatic plastics could be identified (Zhou et al., 2021). Therefore, the focus concerned with hyperspectral satellite data has to be synthetics with a larger spatial extent, such as greenhouses, photovoltaic modules, roof materials and materials commonly to be found in industrial sites. A further constraint and challenge in identifying plastics from satellite data is that there are diverse optical characteristics within the same type. Especially, most plastics remain transparent or translucent and thin to save cost, introducing the quadratic term of transmittance and the reflectance of the background directly below it. Hence, the background has strong influence on the apparent reflectance (Kuester and Bochow, 2019).

Varying abundances of plastic in different contexts further introduces uncertainties in the development of detection algorithms. Supervised classification methods require numerous training pixels covering all the above-mentioned conditions, optical properties and combinations, which makes their generation very demanding for plastics. Thus, usually deep learning or machine learning algorithms are used for such applications with larger datasets. In particular, 'Support Vector Machines' (SVM, (Melgani and Bruzzone, 2004; Fauvel et al., 2008)), 'Random Forest' (RF, (Ham et al., 2005; Belgiu and Drăgu, 2016)), and 'Convolutional Neural Networks' (CNN, (Yu et al., 2017; Zhu et al., 2017)) are the most widely employed machine learning algorithms for hyperspectral imagers (HSI) that classify pixels depending on the spectral similarity of the unknown and the training samples (Lu et al., 2017).

Our general focus in this study aims to assess the capability of hyperspectral data measured in the laboratory, or acquired by aircraft and satellite sensors to classify and identify plastics of different chemical compositions and varying optical properties based on spectral libraries and machine learning methods. To meet the objective, a spectral library is set up and a validated model is constructed, which is transferable within different hyperspectral sensors and datasets and reliable under various ground conditions. We collected the spectra from three spectral libraries and proposed a routine of mixing strategy to randomly generate a training and a test dataset using the spectra of ten distinct plastic types and numerous non-plastic materials of five different material groups. Three widely used deep -, and machine learning algorithms, CNN, RF, and SVM are applied to build different classifiers using a synthetic training dataset. The three trained models were

validated and compared by assessing their performance on test datasets, lab measurements, and three airborne images referring to various surface types recorded in Germany by two different sensors. The most robust and reliable classifier is then applied to datasets recorded by the GF-5 and the PRISMA satellites over Weifang (China) to evaluate the respective performance and transferability among both sensors.

5.3 Materials

This section presents the baseline data deployed for training, validation and evaluation. It describes the spectral libraries used, the spectral experiments in the laboratory and the specifications of the air-, and spacecraft sensors involved for recording of the respective data.

5.3.1 Spectral libraries for training and testing

In this study, we used plastic and non-plastic samples for the setup of our training and test datasets. Spectra of non-plastic samples were obtained from two publicly available spectral libraries, a USGS generated one (Kokaly et al., 2017) and the ECOSTRESS library (Baldridge et al., 2009; Meerdink et al., 2019).

The USGS spectral library (version 7) encompasses spectra measured in the laboratory, field, and by airborne imaging spectrometers covering a wide wavelength range from 0.2 to 200 μm. It comprises spectra of a variety of ground material categories including minerals, rocks and soils as well as vegetation, microorganisms and man-made materials (including plastics).

The ECOSTRESS library also provides a comprehensive range of high-resolution laboratory-derived spectra covering the wavelength range of 0.35–15.4 μm. It contains nearly 2000 spectral curves, where the main types are soils, rocks, minerals, meteorites, vegetation, water-snow-ice and manmade materials. After screening, these two spectral libraries were consolidated and regrouped into five non-plastic subgroups, as listed in Table 5.1.

Table 5.1: Spectral library. Italics: Plastics of the aromatic group; Regular: plastics of the aliphatic group. Bold: most commonly used plastic.

Non-plastic		**Plastic**			
Subgroup	Amount	Subgroup	Amount	Subgroup	Amount
Vegetation	687	*ABS*	4	PE	14
Soil	206	*PC*	4	PA	5
Rock	380	***PET***	12	PMMA	5
Mineral	1730	***PS***	6	**PP**	22
Artificial	263	EVA	4	**PVC**	9

Of these two US libraries, the plastic samples (mostly PE and PVC) were excluded from the category of artificial materials to avoid accidently mixed plastic from different databases. The plastic spectra taken and used as basis for the later mixing procedure to produce the training dataset are from our home-made PlaMAPP library (Table 5.1). The PlaMAPP library is an in-house (GFZ) developed set of high-resolution spectra containing predominantly plastics measured in the nearinfrared (NIR) and SWIR range (0.97–2.5

μm) at a spectral resolution of 1 nm. A wide range of plastics, both commonly used and uncommon, are included here. Five types of household plastics, namely polyethylene (PE), polypropylene (PP), polyvinyl chloride (PVC), polyethylene terephthalate (PET) and polystyrene (PS) covering 95% of the global production as well as a variety of industrial plastics types such as acrylonitrile butadiene styrene (ABS), ethylene vinyl acetate (EVA), polyamide (PA), polycarbonate (PC), and polymethyl methacrylate (PMMA) were selected as basis to construct the training data. While there are more types of plastic in the library, most are too rare with a sample size below four, and hence are not included. Spectra of the respective plastic materials and non-plastic materials are depicted in Figure 5.1.

Plastics are petroleum derivatives with a backbone of C–H chains and distinctive functional groups. Diagnostic absorptions features displayed by plastics in the SWIR range are mainly controlled by the stretching vibration overtones and combination modes of C=O, C–C, and by hydrogen-containing functional groups (X-H), including O–H, N–H, C–H, and others (Schwanninger et al., 2011). The strength of the respective absorptions in the SWIR wavelengths range and the impact of the different groups vary on account of anharmonicity and Fermi resonance. These spectral characteristics offer the potential to identify and distinguish between different types of plastic, based on their unambiguous spectral absorption features (Czarnecki et al., 2015; Beć et al., 2018).

As already comprised in our previous study (Zhou et al., 2021), the general absorption features of the C–H bond in plastics (Fig. 5.1) can be understood based on their mode assignments, including the 1_{st} and 2_{nd} orders of the overtone stretching modes (2ν: 1600–1800 nm, 3ν: 1100–1250 nm) and the combination modes (1νcomb: 2150–2500 nm, $2\nu_{comb}$: 1300–1450 nm). The 2_{nd} order of the combination mode is not included in this study as it is superimposed by a water (O–H) absorption at 1400 nm. The C–H bonds in plastics are linked to functional groups with different masses and bonding constants. These functional groups cause a shift in the position of the C–H absorption peaks. One of the functional groups that has the most influence on the spectrum is the benzene ring. Compared to plastics without benzene rings (aliphatic group: EVA, PA, PE, PMMA, PP, PVC), the absorption peaks of plastics with benzene rings (aromatic group: ABS, PC, PET, PS) are shifted to shorter wavelengths in both 2ν and 3ν, and an additional absorption occurs in $1\nu_{comb}$ around 2150 nm.

Apparently, the spectral features are similar in the same groups of plastic, with only subtle variations in the position of absorption peaks, which poses a great challenge for differentiating them. In comparison, the spectra of the five subgroups of non-plastics show quite strong variations to each other and also differ to the spectra of plastics. We focused on classifying the ten plastic types mentioned above, while all non-plastic materials are clustered as one class. The sub-grouping of non-plastic materials is only useful to reduce the covariance when performing the mixing of non-plastic spectra with plastic spectra.

The pre-processing strategies and the details of the mixing procedure of the reflectance data are introduced below in section 5.5.1. All selected plastic samples used in the following experimental setups were not included in the training dataset for effective validation.

5.3.2 Lab measurement setup

Samples of the five most common plastic materials (PE, PET, PP, PS, and PVC) with different optical properties, such as transparent, translucent, opaque-bright and opaque-dark, were selected for the laboratory measurements. Samples were placed on two different

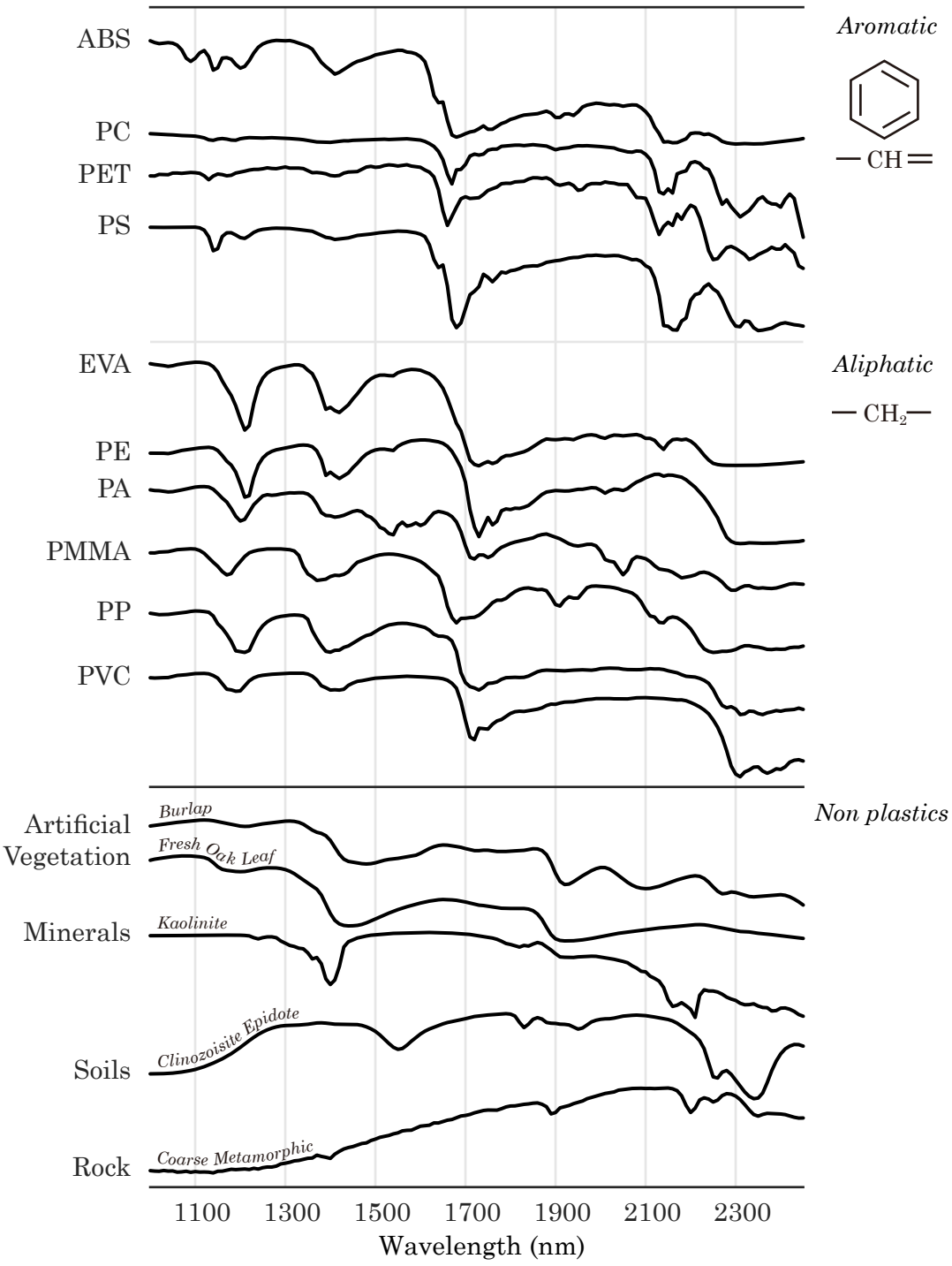

Figure 5.1: Stacked plot of lab-measured reflectance spectra resampled to the resolution of PRISMA and GF-5 (10 nm). Spectra are offset for clarity.

soil types, a dry bright sandy soil and a dry dark organic soil. The measurements were performed with a HySpex SWIR320m-e hyperspectral imager built by Norsk Elektro Optikk (NEO) using an in-house measurement protocol (Rogass et al., 2017) under laboratory conditions. A HEDLER H25s light source, equipped with two 650 W tungsten-halogen bulbs, was used to replicate the solar spectrum. Reflectance was calculated by the empirical line correction method (Conel et al., 1987)(Conel et al., 1987), using the spectrum of a three-color Zenith® reference plate (albedo: 90%, 50%, 20%) placed in each scene.

5.3.3 Sensors used for data recording

5.3.3.1 Airborne

Primarily, three hyperspectral imagers were used to record the airborne dataset, including the HyMap whisk-broom sensor (Cocks et al., 1998), and two push-broom scanners, the HySpex Mjolnir S-620 (NEO) and HySpex-SWIR-320m-e.

The HyMap imager with an instantaneous field of view (IFOV) of 2.0 mrad can only be used in conjunction with an aircraft and acquires 512 pixels in across track direction covering the wavelength range of 0.45-2.48 μm with 128 bands at 13-17 nm intervals. The HySpex Mjolnir S-620 is mounted on a UAV, covering the 1.0-2.5 μm wavelength range with up to 300 bands at 5.1 nm intervals. It records lines with 620 pixels with an across-track IFOV of 0.54 mrad.

The HySpexSWIR320m-e used also for lab measurements was operated from an aircraft platform with an across-track IFOV of 0.75 mrad, recording lines with 320 pixels. It operates in the 1.0-2.5 μm range, producing 256 bands with a spectral interval of 6 nm.

HyMap data loaded were recorded and fully processed by the German Aerospace Center (DLR). The atmospheric correction of the HySpex Mjolnir S-620 data was accomplished using the SICOR software (Bohn et al., 2020) and the geometric processing was performed with the PARGE software (Schläpfer and Richter, 2002).

The data recorded by the HySpex SWIR-320m-e sensor were preprocessed including co-registration and sensor adaptation using HyPrepAir, an internal GFZ processing procedures described by Brell et al. (2016). Thus, all airborne datasets have been processed to level 2 including radiometric, atmospheric and orthometric corrections.

5.3.3.2 Satellite

To evaluate the capability for generalization of the models, we collected data recordings from two different spaceborne hyperspectral push-broom scanners, including one set of the GF-5 Advanced Hyperspectral Imager (AHSI) data, and two sets of PRISMA imagery. The main specifications of both satellite sensors are listed in Table 5.2.

The Chinese meteorological satellite GF-5 was launched in May 2018, orbiting in a sun-synchronous orbit at an altitude of 705 km. The ground processor produced level 1 (L1) radiance products, which include radiometric corrections and system geocoding (`https://www.cheosgrid.org.cn/index.htm`). The GF-5 image was downloaded and the transformation to radiance data was calculated according to the provided gain and offset values. Subsequently, atmospheric correction was applied using the SICOR software (Bohn et al., 2020) to retrieve 'at surface reflectance' of the targeted areas. The satellite stopped operating in 2020 but a second generation of the GF-5 was launched in September 2021.

Table 5.2: Nominal parameters of spaceborne hyperspectral sensors aboard the Gaofen-5 and Prisma satelites. In brackets = in orbit measured values

Parameters	**GF-5 (AHSI)**	**PRISMA**
Light dispersion	convex grating	prism
GSD (m)	30 (29.7)	30 (∼38)
Swath (km)	60	30
Wavelength (μm)	0.4 – 2.5	0.4 – 2.5
Number of bands	330	237
Spectral Resolution (nm)	VNIR: 5 (4.3)	VNIR: <12 (13)
	SWIR: 10 (7.9)	SWIR: <12 (11)
Spectral Sampling Interval (nm)	VNIR: –	VNIR: 9.4
	SWIR: –	SWIR: 9.3
SNR (non-dimensional)	VNIR: 300-700 : 1	VNIR: >200 : 1
	SWIR: >200 : 1	SWIR: >100 : 1
Quantization (bit)	12	12

PRISMA is a satellite mission launched by the Italian Space Agency (ASI) in 2019 (Cogliati et al., 2021). It also operates in a sun-synchronous low Earth orbit at an altitude of 615 km. PRISMA's ground processor produces a number of standard products, which are made available to users. Details are available in the PRISMA Products Specification Document. We downloaded two sets of PRISMA data in L2D format (geolocated surface reflectance), with radiometric, atmospheric and geometric corrections accomplished, and ready for evaluation (Guarini et al., 2018).

5.3.4 Spectral comparison between various sensors

Fig. 5.2 shows our lab-derived spectra resampled to the spectral configurations of the above-mentioned sensors, where PE/PP and PET/PS represent the aliphatic and aromatic plastic group, respectively. The spectral resolution (FWHM) and the respective band centering were used to implement the resampling. The HyMap sensor with a spectral resolution of 15 nm shows the coarsest distribution of bands (points) and some spectral information is lost, especially for the serrated feature of PET at around 2200 nm. The HySpex sensor with a spectral resolution of 6 nm in the SWIR shows most details among all the sensors, although, there is not much loss on information for both satellite sensors that sample data at 10–11 nm FWHM.

5.4 Study area

5.4.1 Airborne sites and experimental setups

The airborne instruments described above recorded three selected sites in Germany (Fig. 5.3A-C), each characterized by different landscape features. To ensure validity, the plastic panels placed for the analysis within the airborne target sites were not included in the spectral libraries used to develop the classifier.

One study area, located in the city of Dresden, Germany (N 51°5′17.5″ E 13°45′6.8″), has been recorded by the HyMap system from an aircraft. The image was acquired on July 7, 2004 with a GSD of 4 m (Fig. 5.3A). The area is characterized by an urban landscape.

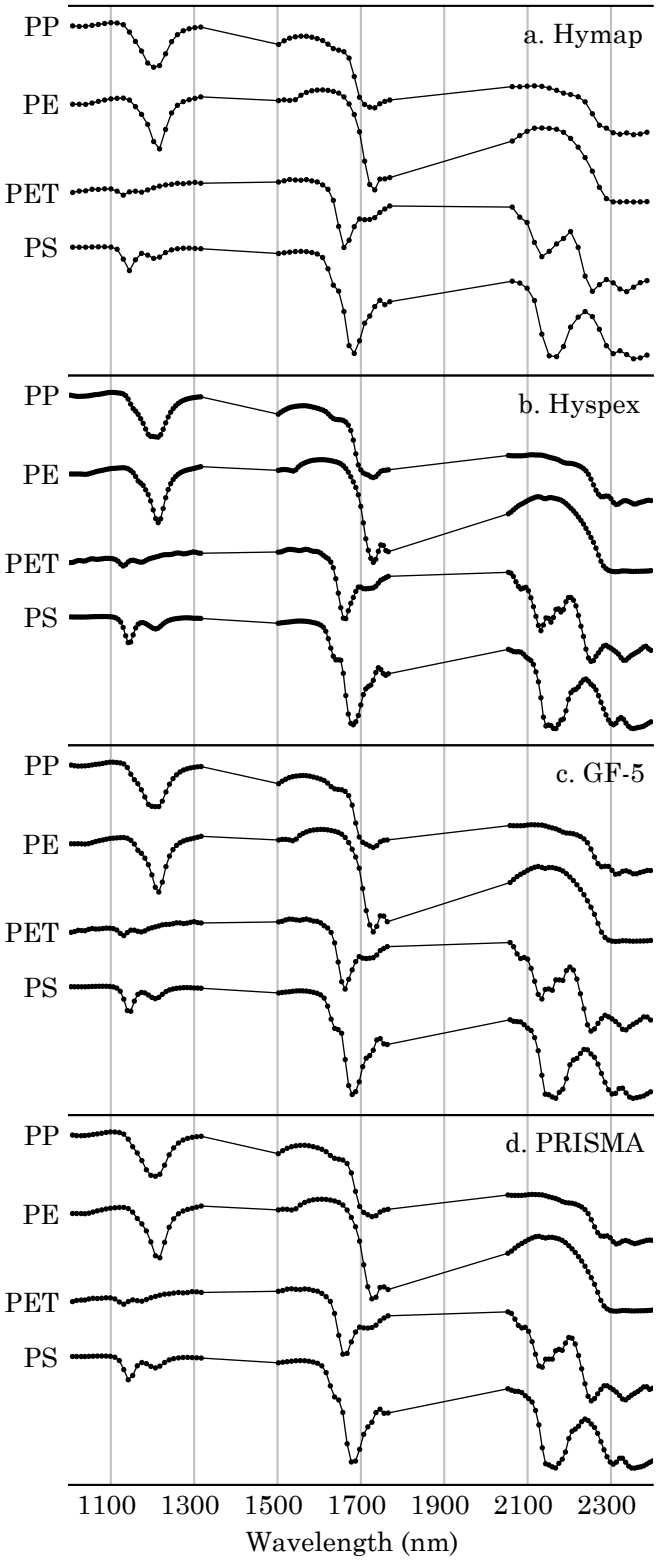

Figure 5.2: Stacked plot of selected plastic spectra resampled to the spectral resolution of (a) HyMap (FWHM: 15 nm), (b) HySpex: 6 nm (FWHM-SWIR), (c) GF-5 (FWHM: 10 nm) and (d) PRISMA (FMHM: 11 nm). Atmospheric water absorption bands at 1320-1500 nm and 1770-2050 nm are masked out.

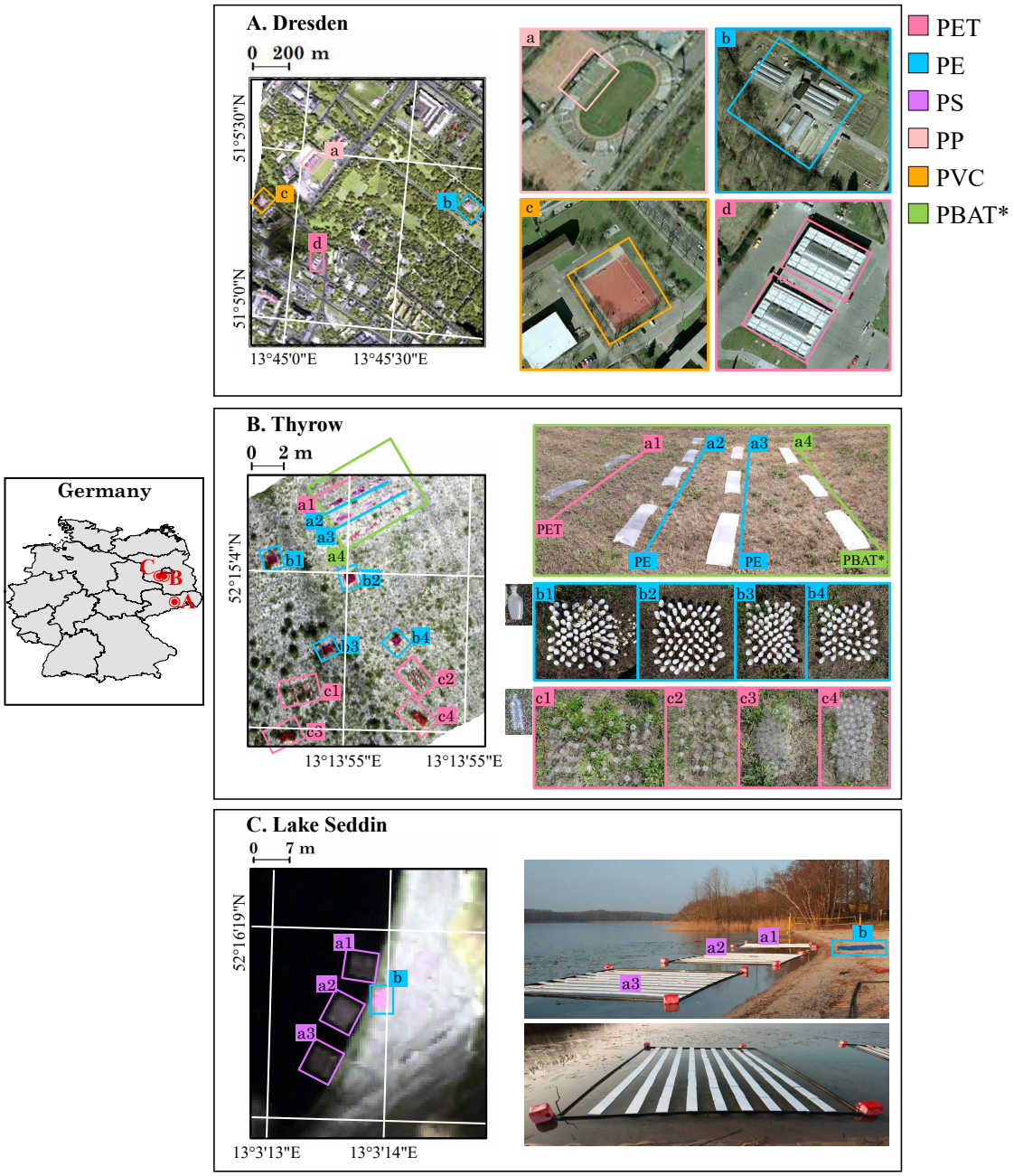

Figure 5.3: Sketch map and detailed coordinates of the test sites in Germany recorded by aircraft scanners and the respective experimental ground configurations with selected plastic materials placed in (A) Dresden, (B) Thyrow and (C) Lake Seddin, *PBAT material is not included in the training data.

Ground control of locations covered by distinct plastic materials was maintained through field work using portable spectrometers and GPS equipment. Among a total of more than 40 different urban materials, four plastic materials (PE, PET, PP and PVC) were identified and mapped based on hyperspectral ground measurements (Heiden et al., 2007; Behling et al., 2015). The ground truth map of the respective plastic materials at individual city blocks were digitized manually on-screen using orthorectified aerial photographs of 0.25 m resolution.

A grassland-dominated study area with a GSD of 3 cm was recorded by the HySpex Mjolnir S-620 imager mounted on an UAV at Thyrow, Germany (N 52°15′4.6″ E 13°13′55.7″) on June 13, 2019. Transparent PET bottles of different sizes as well as large foils made of PET, PE and PBAT plastics were placed on the ground (Fig. 5.3B). As PBAT was not included in the training sample, it allowed us to measure the generalization capability of the classifier by observing how the model handled this unknown plastic.

The third study area included a large water body and was recorded by the HySpex SWIR-320 m-e sensor aboard an airplane with a GSD of 40 cm at Lake Seddin, Germany (N 52°16′21.4″ E 13°3′12.3″) on February 16 in 2015. Lake Seddin is a lime-rich, unstratified lake with a relatively large catchment area (`https://www.berlin.de/tourismus/brandenburg/1169413-1098592-seddinersee.html`). The average of the depth at shoreline is around 20 60 cm. Three arrays of white and opaque PS foam sheets (15%, 25%, and 40% partial coverage) and a blue PE tarpaulin (100% partial coverage) were placed on the shallow lake and its sandy shore (Fig. 5.3C). The grassland and lake scenarios described above were fully controlled experimental sites, with ground truthing maps generated accordingly, including all samples.

5.4.2 Satellite site

The study area selected for analysis of the hyperspectral satellite data is located in the north of Weifang City (N 37°5′20.4″ E 119°7′30″), Shandong Province, China (Fig. 5.4). In this context, one dataset of GF-5 and two datasets of PRISMA could be acquired on demand. The scene of GF-5 was recorded in November 14 in 2019. To record the same area with PRISMA, several demands for recordings were submitted to ASI and successfully completed for December 21, 2019 and November 27, 2021.

The chosen area in China depicts agricultural, residential and industrial regions. Greenhouses have grown very prevalent over the last few decades, covering about 20% of the gross cropland area marked by plastics of the PE, PP and PC class (**?**). While the investment in green energy increased, especially the number of photovoltaic panels (PVs) emerged. These are merged and covered by different plastic materials such as PP, EVA, PE and others (Oreski et al., 2021). The high coverage and diversity of plastics and PVs in the landscape, on roofs and industrial buildings make Weifang an interesting research area to assess the respective classification algorithms.

5.5 Methodology

This section focuses on a linear mixed model for the building of a suitable spectral database for the training of different classifiers namely CNN, RF and SVM and their validation based on unified test data considering different noise and abundance levels.

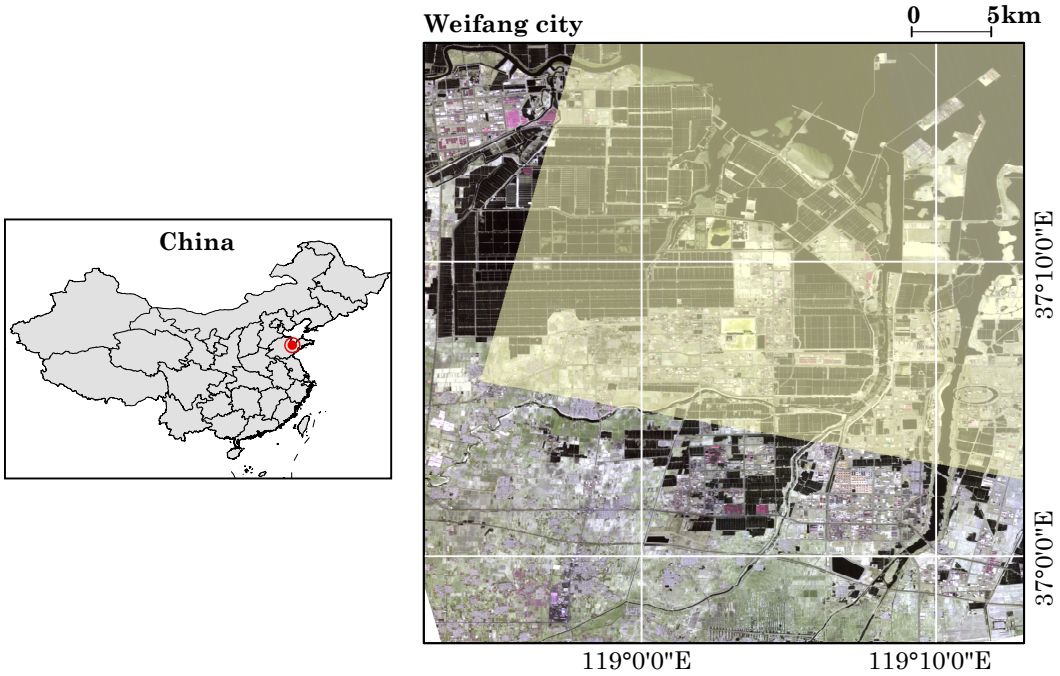

Figure 5.4: Sketch map and detailed coordinates of the test site Weifang City recorded by two satellite sensors (GF-5 and PRIMA). The yellow translucent polygon is the footprint area of the PRISMA 2019 recording.

5.5.1 Generation of training and test dataset by random creation of linear mixed spectra

The major task for any classification procedure is the building of relevant sets of training and test data. The inhomogeneous, sparse, and random distribution of plastic on land surfaces poses difficulties in collecting suitable training and test data by ROIs (regions of interest) in recorded air -, and spaceborne imagery. This applies in particular to datasets from unknown study areas or regions where ground truth is problematic to execute. To overcome this constraint, a feasible approach for classification of hyperspectral data is to rely on spectra of various plastics measured accurately in the laboratory. For this purpose, published and in-house measured spectral libraries (Table 5.1), including thousands of spectra from different materials, were utilized in this study to build an adequate amount of training data. To describe the majority of real-world surface conditions, additional spectra have to be generated. In view of the relatively low spatial resolution provided by the existing hyperspectral satellite sensors, the detection of plastics inevitably requires the consideration of mixed spectra.

5.5.1.1 Linear mixed model (LMM)

The concept of mixed modeling is that each surface can be dominated by a certain number of substances with varying spectral properties. Pure substances are called endmembers and are referred to as fractional abundances. Consequently, the combinations of their spectral properties can be used to simulate the spectral variability observed by remote sensing systems. The linear mixed model (LMM) has been widely used because of its

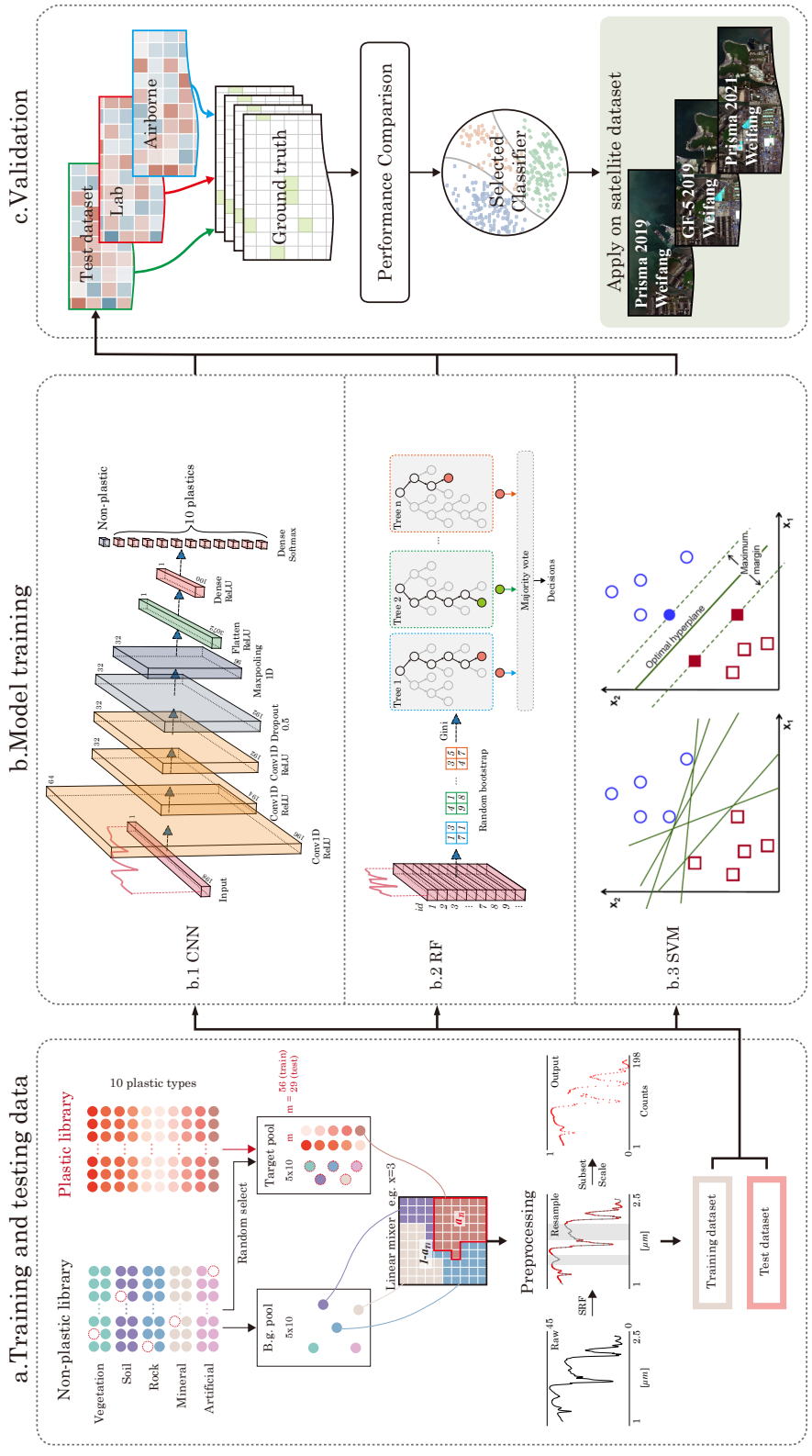

Figure 5.5: Sketch map of the evaluation concept and the respective work flow. See text for acronym definitions.

clear physical relevance and simplicity (Keshava and Mustard, 2002). Besides, it is not necessary to consider all secondary scattering interactions between endmembers. Since the focus is not on an accurate spectral unmixing but on the classification, a simple and practical linear mixed model is applied to generate virtual datasets. An LMM including n endmembers is expressed as follows (Eq. 5.1-5.3):

$$M = \sum_{i=1}^{n} a_i R_i + \varepsilon \tag{5.1}$$

$$\text{s.t.} \quad \sum_{i=1}^{n} a_i = 1 \tag{5.2}$$

$$0 \leq a_i \leq 1 \tag{5.3}$$

where:

M is the received mixed reflectance spectra,
a_i is the abundance of the i^{th} endmember,
R_i is the reflectance spectral of the i^{th} endmember,
ϵ is the error term. To simplify, $\epsilon = 0$ in this study

To be physically meaningful, the LMM is subject to two constraints (Shimabukuro and Smith, 1991) on the entries of a_i : Abundance Sum-to-one Constraint (ASC, Eq. 5.2) and Abundance Non-negativity Constraint (ANC, Eq. 5.3).

5.5.1.2 Random creation of mixed spectra

In nature, plastics are not as widespread or concentrated as other surface materials. They appear in a wide variety of shapes and are generally dispersed in small and fragmented areas. The plastic abundance per pixel is usually low, especially for the current hyperspectral satellites with their relatively low spatial resolution of 30m x 30m. For feasibility reasons, the simulation of mixed spectra was limited to the inclusion of only one plastic type per pixel.

Separating plastics from non-plastics is a critical consideration for practical applications, so we have included a broad category of non-plastics materials in addition to the ten plastic types mentioned previously (Table 5.1). Over 3000 samples were collected within the three former mentioned spectral libraries. If all possible combinations of mixtures were put together using all spectral samples, the size of the generated dataset would exceed our computing capacity, so we performed a random sample process (Fig. 5.5a). According to Table 5.1, the spectral library samples are first divided into non-plastics and plastics, which are further subdivided into five and ten classes, respectively.

In the linear mixing procedure, only two components are considered, i. e., pure target spectra, and background spectra, which can be a single sample or a mixture of different samples. Thus, we constructed the two pools of spectral candidates for our **training dataset** according to the following routines:

- R1. In total, 56 plastic training samples were entered into the **target pool**, which are randomly selected from individual types of plastics at a sampling rate of 0.6. At least 2 samples per plastic types were selected

- R2. A total of 50 non-plastic training samples were added to expand the **target pool** by randomly selecting 10 samples from each subgroup of the entire non-plastic collection.

- R3. Finally, further 50 samples are selected to construct the **background pool** by randomly taken ten samples of every type from the remaining non-plastic samples after step 2.

After the spectral pool for linear mixing is completed, the corresponding abundances need to be set. Each of the target samples m_{Ti} in the target pool will enter the linear mixing procedure sequentially at different abundances. To cover as many combinations as possible, the abundance of the target spectra a_{Ti} was set to increments from 0.1 to 1 in steps of 0.1. For each abundance step of every target spectrum, the background spectra are carefully calculated. The backgrounds comprise up to five different subgroups, ensuring a diverse mixing of backgrounds. The number of subgroups that entered the calculation of background x is set from 0 to 5 in steps of 1. Note that x is 0 only when a_{Ti} equals 1, implying that only pure target spectra exist. The total number of combinations of subgroups is determined by the value of x, which equals C_5^x. For instance, when x equals 3, the possible combinations of choosing 3 subgroups out of all 5 subgroups will be 10 (C_5^3). Since there are 10 samples per subgroup, the possible combinations c_x equals $10^x \times C_5^x, x \in [0, 5]$.

As traversing all possibilities would produce too much data, a random subset with a maximum of 100 different combinations for each value of x is applied. After the random screening procedure, the total amount of combinations of various background samples generated for one target sample at each abundance step is calculated by $\sum_{x=0}^{5} C_{c_x}^{min(100,c_x)}$, and equals 450. The abundance vector ax is randomly generated under the two basic constraints of the 'non-negative' and the 'sum-to-(1-a_{Ti})' rule. Ultimately, 4,050 simulated mixed spectra were generated based on i^{th} target samples calculated by the following equation after iterating all abundance steps a_{Ti}. The LMM is shown in Eq. 5.4:

$$M_S i = a_{Ti} R_{Ti} + \sum_{min(x), x \in [0,5]}^{max(x)} a_x R_x \tag{5.4}$$

After finishing the above routine, the original training dataset containing 56 plastic samples and 50 non-plastics samples is enlarged more than four thousand times. Once the plastic spectra entered the mixing procedure, the output mixed spectra are labeled as the type of plastic, otherwise, it is labeled as non-plastic.

The generation of the **test dataset** follows the same mixing routine but with the remaining 29 plastic samples that are excluded from the above mixing procedure, as well as the different background pools which are newly randomized. With this strategy, the generated training and test datasets are independent of each other, ensuring a valid and reasonable measure of each model's performance. At this point, we have obtained a sufficient training and test dataset, totaling 429,300 and 319,950 spectra, respectively.

5.5.1.3 Unification of the band configuration

To obtain the optimum classification results per sensor, the methods described need to be adapted to each individual sensor, which is extremely time-consuming. In this study,

we opted for a unification of the band configuration to investigate the transferability of the methods to any image data obtained by hyperspectral air-, and spacecraft sensors with different spectral alignments. Thus, a virtual sensor with a distinct spectral response function (SRF) was defined. The SRF describes the sensor's relative sensitivity to energy of different wavelengths and is determined by the center wavelength λ_c and the bandwidth $\Delta\lambda$ (also referred to as band pass or spectral resolution) (Strobl, 2000). The bandwidth corresponds to the full width half maximum (FWHM) of each function. For hyperspectral sensors, the SRF can be approximated by a Gaussian function (Eq. 5.53, (Küster, 2011)) for each wavelength.

$$SRF(\lambda) = e^{-2\frac{\sqrt{ln4}(\lambda-\lambda_c)}{\Delta\lambda}^2} \tag{5.5}$$

In this study, the FWHM ($\Delta\lambda$) was set to 5 nm with wavelengths ranging from 1,000 to 2,435 nm. A spectral sampling interval of 5 nm has been chosen that equals the FWHM. This selection fits with the spectral resolution of the GF-5 and PRISMA sensors without creating too much redundant data and further issues with computing capacities. A similar band pass and FWHM is an optimum configuration in spectroscopy and used in GF-5, PRISMA and other spectrometers, e.g., the airborne AVIRIS (Swayze et al., 2003). As shown in Fig. 5.22, the water absorption bands ranging from 1320-1500 and 1770-2050 were removed. Finally, an SRF with 198 bands was generated. Next, all hybrid spectra (training and test dataset), all experimentally derived datasets, and all airborne hyperspectral datasets as well as the satellite dataset were convolved to the SWIR spectral configuration of the virtual sensor using Eq. 5.6:

$$R_i = \frac{\int_{\lambda_0}^{\lambda_1} SRF_i(\lambda)\, R_{origin}(\lambda)\, d\lambda}{\int_{\lambda_0}^{\lambda_1} SRF_i(\lambda)\, d\lambda} \tag{5.6}$$

where R_i is the reflectance value of the i_{th} band of the target spectra, $SRF_i(\lambda)$ is the simulated spectral response in band i, and $R_origin(\lambda)$ is the reflectance of the original spectra (Van der Meer and de Jong, 2011). After the resampling, the reflectance data were further normalized within the range of 0-100%.

5.5.2 Machine learning algorithms

Three widely used deep learning and machine learning algorithms CNN, RF, and SVM are used for classification and compared to each other in the frame of this study (Fig. 5.5b). Using the Python package, the CNN was implemented with TensorFlow version 2.5.0 (Abadi et al., 2016). The SVM and RF models were implemented with the scikit-learn version 0.22.1 (Pedregosa et al., 2011), and with the GridSearch function to find the best hyperparameters. To train and validate the selected three models, the spectral datasets generated and unified in Section 5.5.1 were applied and used for tuning the hyperparameters.

5.5.2.1 Convolutional Neural Network (CNN)

The CNN model described here (Fig. 5.5b.1) is fairly simple, consisting of three convolutional layers (1D), a dropout layer, one max pooling layer and one flatten layer, followed by two fully connected dense layers. Convolutional layers were used for extracting spectral

features from the input data with kernel sizes set to 3. We used the rectified linear unit ($ReLU, ReLU\,(x) = max\,(0, x)$) as the activation function in all convolutional layers, flatten layer, and the first dense layer. In the last fully connected classification layer, we used a softmax activation function which models the input data to the probability of belonging to each considered class. The categorical cross-entropy is used as loss function. The CNN model was trained with the AdamW optimizer (Loshchilov and Hutter, 2019). During the training of the model, the weights and biases of each neuron are adjusted using a back-propagation criterion, while the error is minimized by a gradient descent (Schmidhuber, 2015).

5.5.2.2 Random Forest (RF)

The Random Forest (RF) is a machine learning method built on Classification and Regression Trees (CART), shown in Fig. 5.5b.2. A random sample of the predictor space is used to avoid overfitting. At each node of the decision tree that needs to be split, x features are randomly selected from the entire feature collection of the sample. Here, the Gini index is used to calculate the criterion (Breiman, 2001) and determine the optimal split feature.

5.5.2.3 Support Vector Machine (SVM)

The Support Vector Machine (SVM) is also widely used for the classification of hyperspectral images (Fig. 5.5b.3). This study utilizes a Gaussian radial basis function (RBF) kernel. The two important parameters, including C (the parameter that controls the amount of penalty during SVM optimization) and γ (the spread of the RBF kernel), are tuned by the GridSearch function in scikit-learn (Chapelle et al., 2002).

5.5.3 Validation

5.5.3.1 Indicators (F1, recall, precision, kappa)

For evaluation and comparison of the performance of each model, confusion matrices based on ground truth maps (see Section 5.4.1 for details) were derived. Statistical indices were employed to determine the reliability and generalizability of the classifier in identifying plastics when applied to both laboratory and airborne datasets. The basic criteria include recall, precision, and overall accuracy (OA). The F1-scores were obtained by calculating the harmonic mean of recall and precision to avoid bias from unbalanced ground truth. The higher the F1 value the better the performance. Additionally, Cohen's kappa coefficient was considered to estimate the consistency and robustness of the classifier.

5.5.3.2 Introduction of noise

In practice, satellite hyperspectral images contain inevitable noise, so validation is further conducted by introducing different noise levels in the test data to compare the performances of the three models used. The Gaussian additive noise is chosen for the inclusion of noise to simulate real-world hyperspectral images, where the signal-to-noise ratio (SNR) in dB is defined as Eq. 5.7:

$$SNR = 10log_{10}\frac{E\left[S^T S\right]}{E\left[N^T N\right]} \tag{5.7}$$

where S and N denote the signal and noise, respectively, and the symbol $E[\bullet]$ represents the expected value. We analyzed a wide range of SNR ranging from 10 to 106, which covers the common SNR range (100 1000) of existing satellite sensors (Table 5.2).

5.6 Results and discussion

5.6.1 Performance comparison on a randomly generated test dataset

Fig. 5.6 depicts a heatmap of three confusion matrices and the precision and F1-scores, indicating the classification performance of (a) CNN, (b) RF, and (c) SVM on the entire test dataset of plastic and mixed spectra. The overall accuracy is 97%, 96%, and 95% for CNN, RF, and SVM, respectively.

In terms of precision, the non-plastic classes were identified by more than 95% accuracy, regardless of the method used, where the CNN provided the best results (>99%). For plastics, the precision resulting from the CNN is over 95% for most classes except the ABS, PC, and PA. When using the RF, the precision is not as significant but is more stable among different plastics, fluctuating at around 95%. Similar to the results of the CNN, the use of the SVM provides high precision on most of the plastic types (>95%) but varies considerably, for example below 70% for PA and PVC. Considering the above two indicators together, the F1 score values indicate that the CNN delivers the best performance on the test dataset, with most classes reaching 95%. In contrast, both the RF and the SVM are flawed, where the RF, shows values below 95% in most classes, despite stable F1-score on all classes with little variations. The SVM gives F1-scores above 95% for some classes, but is very unstable, with PA and PVC only reaching around 80%.

The diagonal matrix values in the three confusion matrices reveal the recall rate. Collectively, recall rates exceeded 95% and 90% for all plastic classes when the CNN and SVM were used, and 85% for most plastics (apart from ABS, EVA, and PC) when the RF was used. Among the cases of misclassification in the three models, most of those spectra containing plastics are classified as non-plastics, especially for the RF model. Notably, more than 10% of the spectra containing ABS were mislabeled as PS, while >15% of spectra containing EVA were mislabeled as PE or PP. This follows a certain logic, since ABS/PS are both aromatic plastics and EVA/PE/PP are aliphatic plastics with rather similar spectra. For non-plastics, the RF gives the best recall rates of up to 99%.

In addition, we also examined the performance of the three models in identifying spectra at different abundances. Fig. 5.7 illustrates the variation of F1-scores using the three classifiers in relation to the increasing plastic abundances from 0.1 to 0.9 in steps of 0.1. The statistics show that the RF performs less good with respect to the F1-scores, especially when the abundance is lower than 0.3, and it is worst for the spectra containing ABS, PC, and EVA plastics. This is consistent with the confusion matrix, as most of these spectra were classified as non-plastics, which is plausible at low abundances. In contrast, the CNN and SVM have stable and high F1-scores, reaching 80%, starting from an abundance of 0.2 in all plastic classes. However, from another perspective, having such high F1 scores given by CNN and SVM implies a possible over fitting problem. Considering a real-world situation, the robustness of the three classifiers was further compared by introducing varying noise components to the test spectra. The respective SNRs are simulated using Eq. 5.7. The F1-scores estimated by the three algorithms at a noise level increasing from 5dB up to 60dB with steps of 5dB are demonstrated in Fig. 5.8. When the SNR is

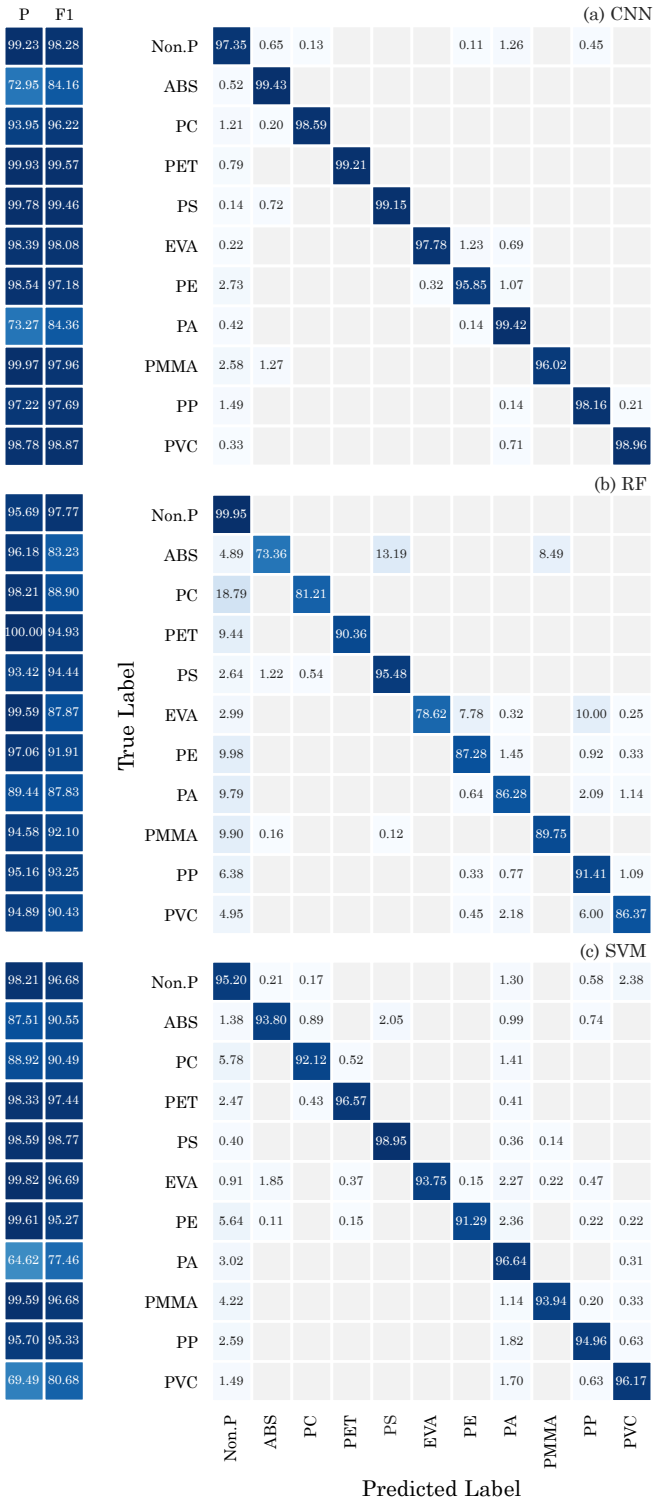

Figure 5.6: Heat map of precision (P), F1-scores (F1) and confusion matrices based on all spectra in the test dataset using the classifiers of (a) CNN, (b) RF and (c) SVM.

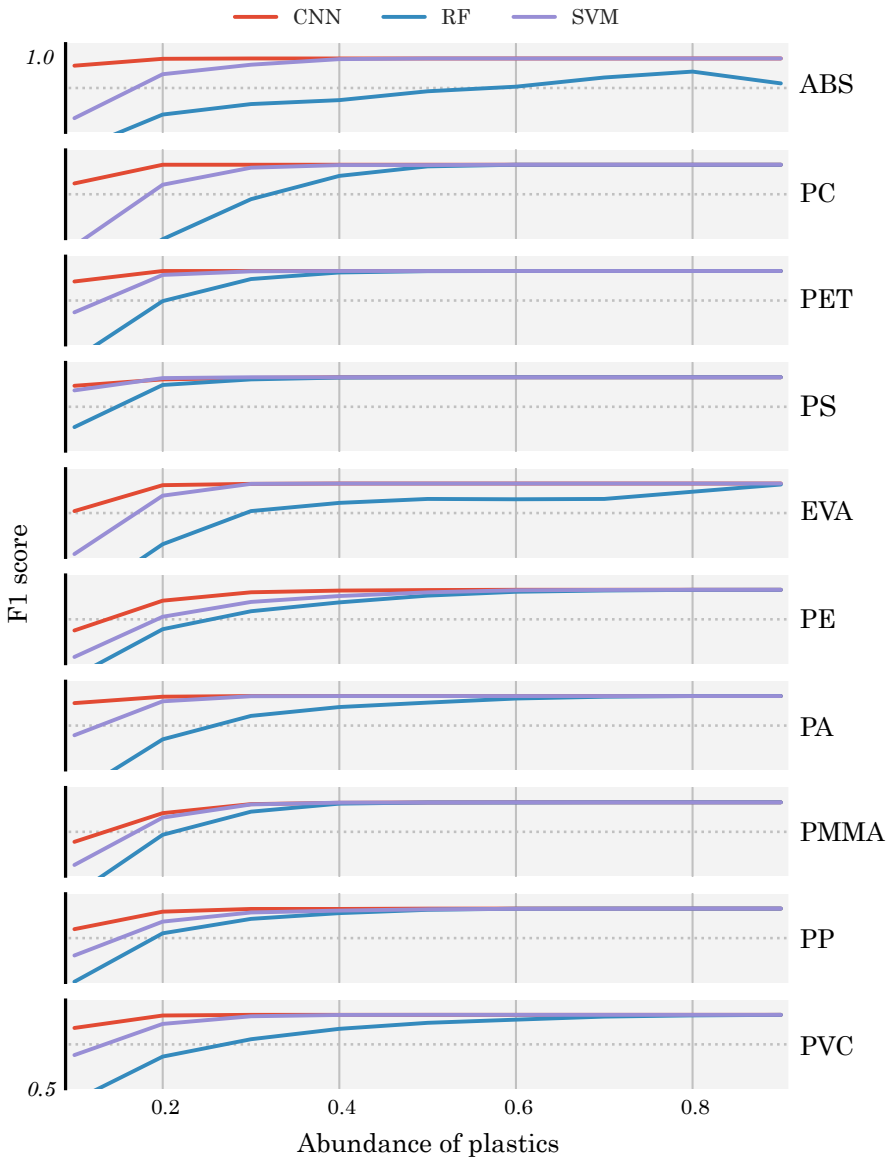

Figure 5.7: Line plot of the F1-scores versus an increasing plastic abundance based on all plastic spectra in the validation dataset using the CNN (red), RF (blue), and SVM (purple) classifiers.

relatively high, e.g., SNR = 40dB, the F1 values for each algorithm are relatively good (>90%). The disparities between the different algorithms become apparent as the noise interference increases. The trends of the SVM and RF graphs are almost identical, with F1 values reaching 80% from a SNR of 15dB. In contrast, the CNN reaches the 80% level from 25dB onwards. The F1 values obtained for both, the SVM and the RF at high noise levels are higher than those obtained for the CNN, but the CNN slightly outperforms the other two at low noise levels when the SNR equals 40dB. These results demonstrate that despite the better statistical performance obtained in the validation dataset using a CNN, the SVM and RF approaches are more robust and stable in the presence of noise interference.

5.6.2 Evaluation of laboratory experiments

Fig. 5.9 displays the laboratory setup comprising 5 most common types of plastics in 5 varying optical properties placed on a bright sand (a) and a dark soil (b) background. The assemblies were measured by our HySpex sensor and also classified by the three formerly used machine and deep learning algorithms. The top row shows SWIR color composites of the configuration, while the following rows depict the results derived by the CNN (a-1, b-1), RF (a-2, b-2), and SVM (a-3, b-3) classifiers. Each column in the individual scenes represents a collection of samples of the five most common plastic materials (PE, PET, PP, PS, and PVC) with different physical properties. Each row signifies materials with the same optical properties, such as transparency, translucency, bright/medium/dark opacity.

The results show that most materials are well classified in this experiment, apart from the black samples with an average reflectance of less than 10%. This can be explained by the low apparent albedo of the targets, resulting in an inadequate SNR and a severe extinction of the significant absorption features. The black samples were classified as 'other' not existing plastic types in the scene by the CNN and SVM, while the RF treated them as non-plastics. All other plastic materials were recognized correctly on both backgrounds by all three classifiers, independently of the optical properties.

The classification accuracy of plastics on the bright sandy background is very high, reaching >98% for each category. Therefore, the confusion matrix for the computed classification results is only provided for the dark soil background in Table 5.3. As the classifier, trained with 10 types of plastic in total, could incorrectly detect plastics that were not present in the scene, a nonexistent class (NE) has to be added to the matrices. All models performed well (recall >90%) when focusing only on the classification among different plastics, in which the recall rate reaches 99% using the CNN and SVM while only 6% of PVC is classified as non-plastics when using RF.

In contrast, the classification results of these methods for background (non-plastic) varied considerably. By using the CNN, only 58.88% of the backgrounds were recognized correctly, while over 40% were misclassified as plastic not even present in the scene. The SVM has a better recall rate than the CNN, but it still misclassified 10.89% of the background, of which 8.79% referred to non-existing plastics. The recall rate was 99% when using the RF, which is quite robust and consistent with the results of the previous section. The high precision rate (>90%) for all categories using both the CNN and RF suggest their capacity for accurate prediction over all positive observations while the SVM is less competent. However, the separation of plastics from other non-plastic materials is very critical. Yet the CNN gives higher precision, it didn't meet the basic expected performance. The comprehensive metrices (F1-score, OA, and Kappa) indicate the highest

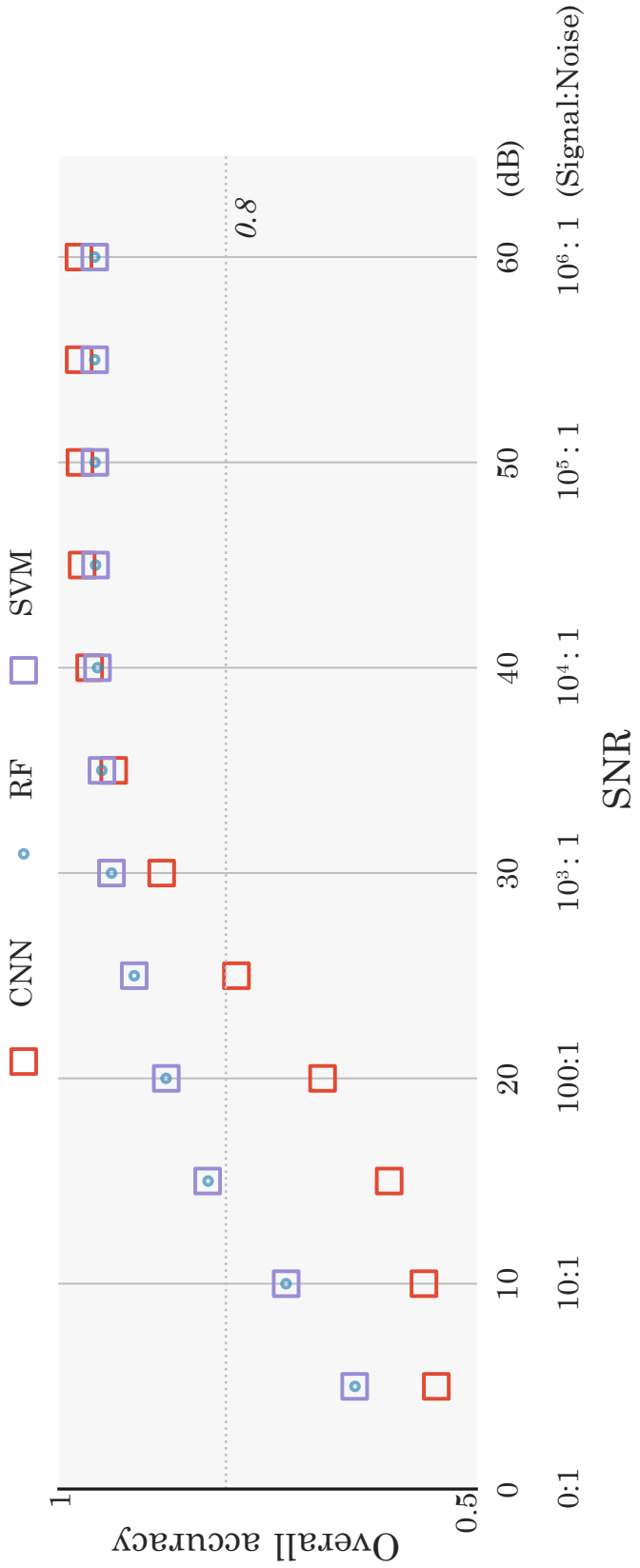

Figure 5.8: Scatter plot of F1-scores versus an increasing SNR (log and standard) based on all spectra in the validation dataset using the classifiers of CNN (red), RF (blue), and SVM (purple).

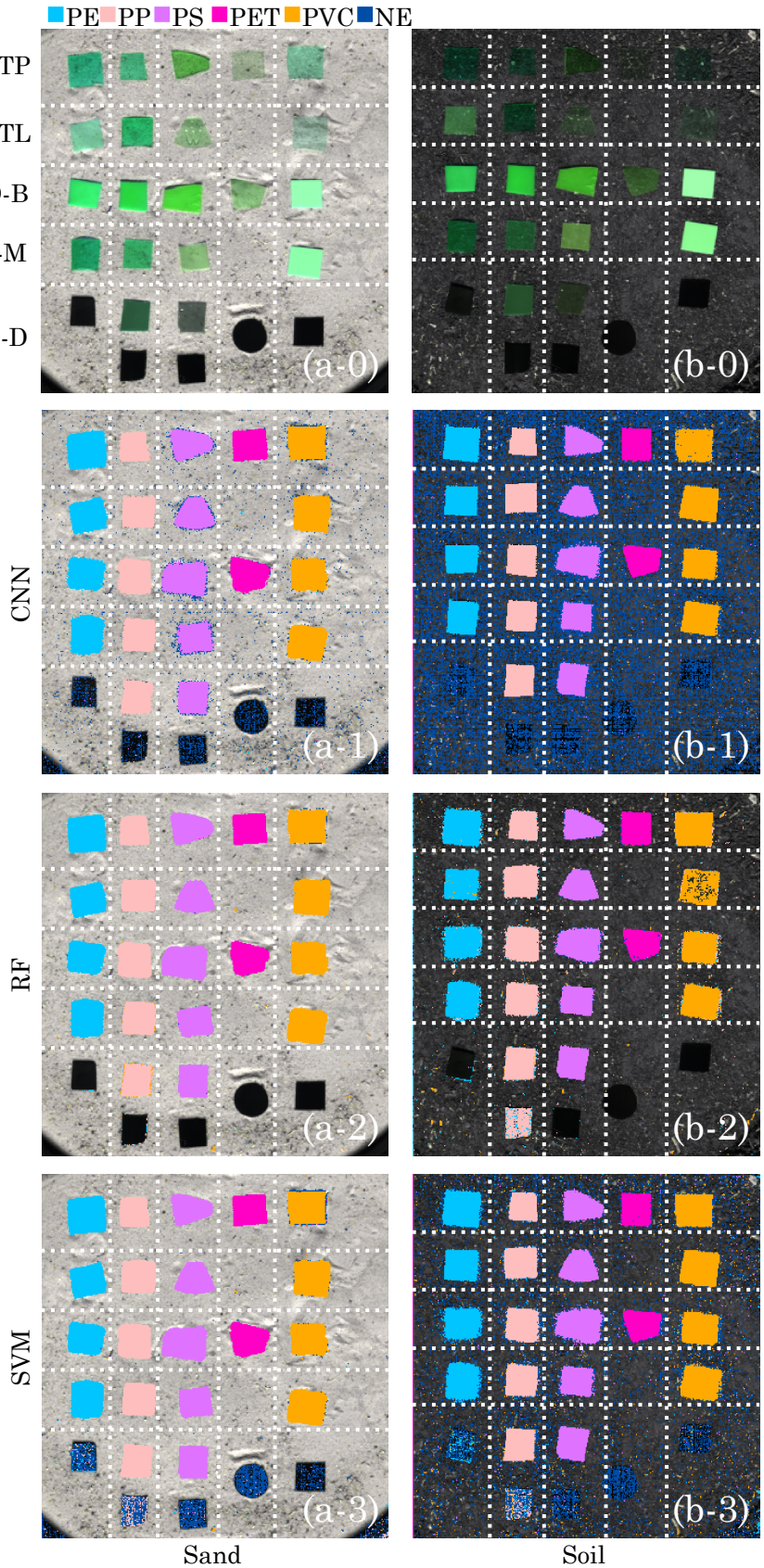

Figure 5.9: Classification results based on laboratory data measured by the HySpex sensor. Five different plastic materials of various optical properties are placed on (a) bright sand and (b) dark soil backgrounds. The two top panels (0) depict color composites using wavebands 1730 nm, 1570 nm and 2200 nm coded RGB. Results of the classification using (1) CNN, (2) RF, and (3) SVM are shown from the second row to the bottom. TP: transparent; TL: translucent; O-B: opaque bright; O-M: opaque medium; O-D: opaque dark. NE: plastic types not existing in the scene. *The non-plastic class in the results is displayed as transparent to show the background image.

general accuracy for the RF, followed by the SVM, and the lowest value for the CNN due to its low recognition of backgrounds.

5.6.3 Evaluation of hyperspectral airborne datasets

To estimate the performance of the three classifiers to identify plastic in a real-world scenario, we validated them further on three airborne datasets with different surface properties. Fig. 10 displays the results from the airborne data with various plastic materials on three background surfaces recorded by two airborne hyperspectral instruments. The results derived by the CNN, RF, and SVM classifiers are displayed from the second row to the bottom. Table 4-6 presents the confusion matrices of the classification results for each site. Similar to the strategy in the previous section, an NE class is introduced to signify those plastics that are either not present or not included in the ground truth map.

For the urban scene (Fig. 5.10a-0,1,2,3), four types of plastic are selected and identified for the ground truth map for validation. According to Table 5.4, all classifiers showed a good performance in detecting PP, with both recall and precision exceeding 95% when using the CNN and SVM, and 90% when using the RF. Concerning the identification of PE and PVC, the CNN indicated a poor performance with recall rates below 80%, while the values were above 90% when applying the other two models. Still, the accuracy obtained with the CNN is over 95%, which is the same as achieved by the SVM, whilst RF gives a precision ranging from 90% to 95%. All classifiers had the poorest results in correctly identifying PETs, with recalls below 60%. It can be seen that more than 70% of false negatives went to the NE category, which are the types of plastics not included in the validation map, of which, the majority were classified as PS. Based on our study in 2021 (Zhou et al., 2021), both PET and PS contain aromatic rings, belonging to the same cluster with similar absorption characteristics.

In addition, it can be assumed that the presence of remaining atmospheric influences or the unification process further contributed to the non-discriminability between the spectra of the two types of plastics in this image. The accuracy obtained when using the RF is surprisingly high, indicating that even when it fails to thoroughly discover PET, the determination is deemed to be highly plausible when it detects the class. By contrast, the precision values given by the CNN and SVM were below 60%, suggesting a low confidence level in their detection results for this class. As for the non-plastic category, the use of the RF gave a promising result with recall and precision values over 95%. Yet, when using the CNN and SVM, more than 15% of the non-plastics were misclassified as plastics, implying that more plastics would be detected than effectively present, which is not conducive to practical applications. The general indicators F1-score, OA and kappa coefficient also proved that the RF produced superior results in the urban scene.

The middle column in Fig. 5.10 shows an artificially arranged experimental grassland on which three types of plastics were placed, including PE, PET, and PBAT. Unlike the results for the urban area, all classifiers gave very high recall and precision rates beyond 99% in detecting PET as shown in Table 5.5. Both the RF and SVM also performed well in classifying PE but the CNN failed to distinguish it from the background in this scene. With regards to the classification results for the background, it is expectable that the SVM mislabeled the background as plastic. PBAT was not involved in the training dataset. With the advent of an increasing number of new types of plastic, it is necessary to examine the responses of these classifiers when encountering new types of plastics. Therefore, this scenario can be used to estimate the generalization ability of the respective

Table 5.3: Confusion matrices of the 5 lab-measured plastic materials on dark soil backgrounds using the (a) CNN, (b) RF, and (c) SVM classifiers. The recall values are highlighted in bold. Non.P: non-plastics, NE: other plastics not existing in the scene, P: precision, F1: F1-score, OA: overall accuracy, κ: Kappa coefficient.

a. CNN		**Predicted label (% Recall)**							**P**	**F1**	**OA**	κ
		Non.P	**PET**	**PS**	**PE**	**PP**	**PVC**	**NE**				
True label	**Non.P**	58.88	0	0.26	0.04	0	0.18	40.64	100.	74.12	0.65	0.4
	PET	0	100	0	0	0	0	0	100.	100.		
	PS	0	0	100	0	0	0	0	94.17	97.		
	PE	0	0	0	100	0	0	0	98.99	99.49		
	PP	0	0	0	0	100	0	0	99.89	99.94		
	PVC	0	0	0	0	0	99.56	0.44	96.2	97.85		
b. RF		**Non.P**	**PET**	**PS**	**PE**	**PP**	**PVC**	**NE**	**P**	**F1**	**OA**	κ
True label	**Non.P**	99.22	0	0	0.19	0.23	0.34	0.02	99.74	99.48	0.99	0.97
	PET	0	99.65	0	0	0	0	0.35	95.27	97.28		
	PS	0	0	100	0	0	0	0	100	99.82		
	PE	0	0	0	99.36	0	0.64	0	94.74	97.3		
	PP	0	0	0	0	100	0	0	99.96	99.98		
	PVC	5.69	0	0	0	0.4	93.91	0	92.04	92.97		
c. SVM		**Non.P**	**PET**	**PS**	**PE**	**PP**	**PVC**	**NE**	**P**	**F1**	**OA**	κ
True label	**Non.P**	89.11	0	0.58	0.48	0.03	1.01	8.79	100	94.24	0.91	0.75
	PET	0	99.82	0	0	0	0	0.18	89	94.18		
	PS	0	0	100	0	0	0	0	100	99.91		
	PE	0	0	0	100	0	0	0	99.37	99.68		
	PP	0	0	0	0	100	0	0	87.77	93.49		
	PVC	0	0	0	0	0	100	0	81.74	89.95		
Total		60,469	1,136	2,504	2,354	2,666	2,744	-				

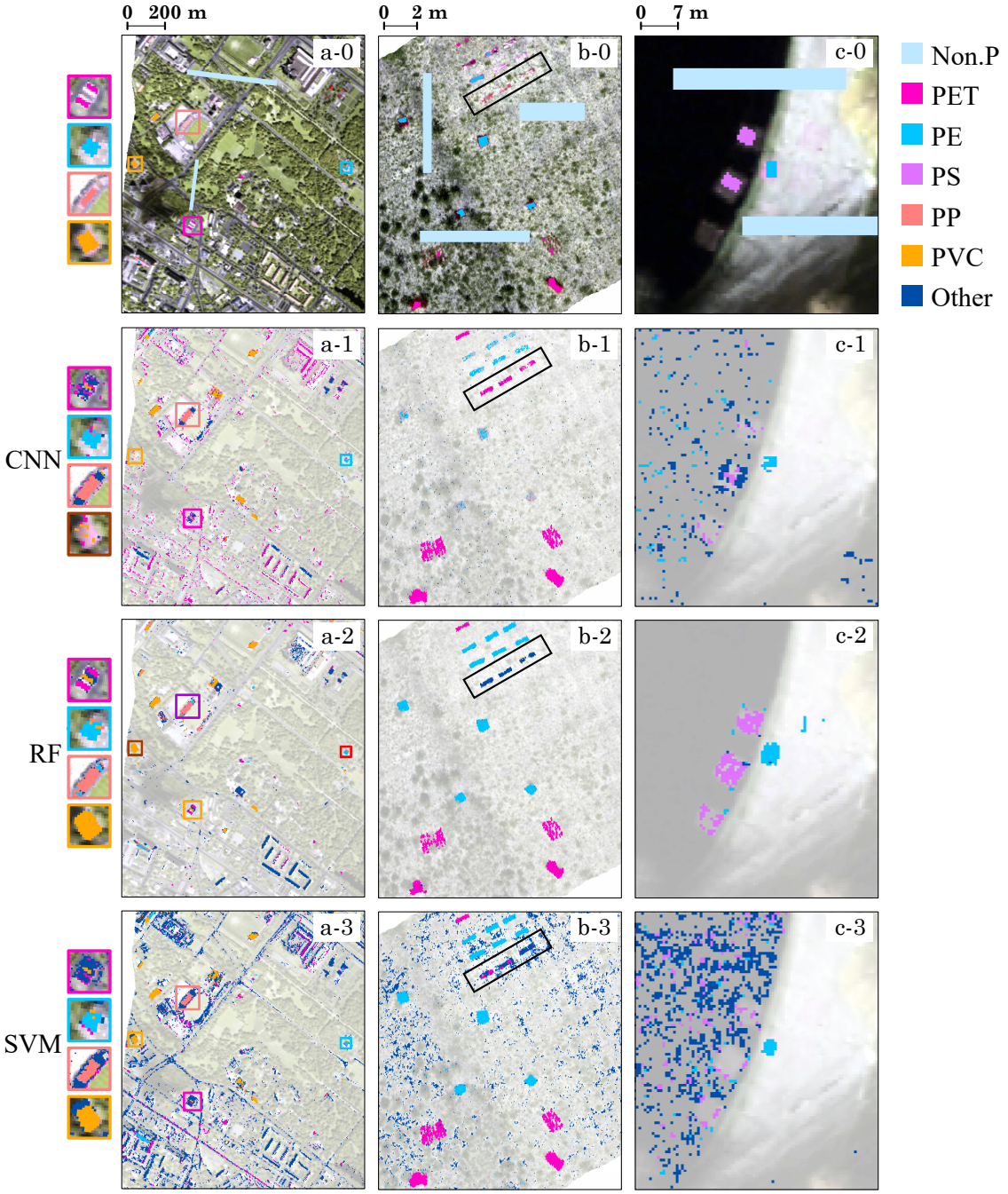

Figure 5.10: Classification results of various plastic materials on three background surfaces based on airborne data recorded by the hyperspectral instruments (a) HyMap and (b, c) HySpex. From left to right, a: urban surfaces (Dresden, DE); b: grasslands (Thyrow, DE); c: lake and shore (Seddin, DE). The top row (0) depicts the ground truth targets of various plastics and non-plastics superimposed on color composites using wavebands 1730 nm, 1570 nm and 2200 nm coded RGB. Non.P: Non-plastic materials, Other: other plastics, not validated in the ground truth map. *The non-plastic class in the results is displayed as transparent to avoid masking of the background image.

model. The sites where PBAT is placed are flagged with black frames in Fig. 5.10b. All the classifiers managed to categorize PBAT into plastics instead of background. One reason is that plastics are synthetic materials polymerized with one-repeat unit, which gives a relatively simple molecular structure. Thus, their absorption features in the SWIR range are easier to explain than those of natural organic materials. This fact reveals that all the models successfully learned this fundamental feature of plastics from the generated training dataset.

The third airborne scenario also represents a controlled experimental site with PS and PE types of plastic included, in which the PS targets were placed over water. Noteworthy, plastics over water are also not included in the training dataset. Thus, this scene is used to estimate the robustness of the classifier over unforeseeable noise. In this context, the RF again showed the best performance according to Table 5.6, while the SVM totally failed and the CNN failed to identify the right class. These results clearly indicate that the RF is the most stable and transferable classifier and will be finally applied to the satellite datasets.

5.6.4 Evaluation of hyperspectral satellite data

The trained RF classifier was applied to three sets of satellite data recorded from Weifang City by GF-5 (Nov. 2019) and PRISMA (Dec. 2019 and Nov. 2021). This allows to examine the classification results in the context of time as well as in relation to the technical differences between the two sensors. Fig. 5.11 shows the classification results of the three scenes, superimposed on a single band of the SWIR range. The top row depicts the same target segment covered by the three recordings with five marked representative sub-scenes a) to e) for more detailed inspection. To support the validation, color composites of the multispectral MSI imager of ESA's Sentinel-2 satellite with a higher spatial resolution and nearly fitting acquisition times were selected and complement the evaluation. Among these five sites, three sites are comparable in all three scenes while two target areas are only covered by two recordings.

In image section a, locations 1 to 4 are classified as PE plastics. This is plausible as these can be recognized as soccer fields (Sentinel-2) that are usually covered with artificial grass made of PE fibers (Sassi et al., 2011). Site 5 was newly constructed after 2019, and thus, is only detected in the PRISMA '21 data. Another discrepancy is to be found in site 6, where the classifier labels a larger area in the GF-5 imagery than in the PRISMA recordings of the same year. According to the Sentinel-2 images of this area, two soccer fields on top are unchanged over the observed time period while the fields to the bottom are under construction in the later stage and the soils are temporarily covered by plastic tarpaulins (a common practice in China), which are also mostly made of PE (Han et al., 2012). The nonconformity concerned with the reduced PE area detected in the PRISMA '19 imagery at site a-2, 5 can only be explained as misclassification due to haze in the PRISMA scene. When examining the VNIR range of PRISMA '19 data, the presence of the tarpaulins can be identified visually but under hazy conditions. A final appearance of PE in this area can be recognized by two indicating pixels at the top left of all three records that is a floating landing bridge reaching into the water.

Image section b covers a residential area surrounded by fish farms and agricultural fields. Three interesting regions are marked in this figure. Area 1 shows a mixture of PE and PP, where most of them are classified as PE in GF-5 '19 data but the percentage of PP increases in PRISMA '21 data. Similar targets with this characteristic PE-PP mixture are

Table 5.4: Confusion matrices of the airborne dataset of Dresden (HyMap) using (a) CNN, (b) RF, and (c) SVM classifiers. The recall values are highlighted in bold. Non.P: non-plastics, Other: other plastics, not existing or not validated in the scene, P: precision, F1: F1-score, OA: overall accuracy, κ: Kappa coefficient.

a. CNN		**Predicted labels (%Recall)**						**P**	**F1**	**OA**	κ
		Non.P	**PET**	**PE**	**PP**	**PVC**	**Other**				
	Non.P	85.37	10.85	0	0	0	3.78	92.83	88.94	0.83	0.7
	PET	13.97	55.31	0	0	0.56	30.17	30.94	39.68		
True label	**PE**	8.7	9.78	64.13	1.09	3.26	13.04	100.	78.15		
	PP	2.8	0	0	97.2	0	0	96.81	97.01		
	PVC	18.14	1.73	0	1.51	78.4	0.22	98.91	87.47		
b. RF		**Non.P**	**PET**	**PE**	**PP**	**PVC**	**Other**	**P**	**F1**	**OA**	κ
	Non.P	99.36	0	0.27	0	0	0.37	98.58	98.97	0.95	0.9
	PET	9.5	57.54	0	0.56	0	32.4	100.	73.05		
True label	**PE**	1.09	0	91.3	0	2.17	5.43	93.33	92.31		
	PP	0.8	0	0.4	91.6	6.8	0.4	90.51	91.05		
	PVC	1.51	0	0	4.97	93.52	0	95.8	94.64		
c. SVM		**Non.P**	**PET**	**PE**	**PP**	**PVC**	**Other**	**P**	**F1**	**OA**	κ
	Non.P	80.43	3.88	0.11	0.21	0	15.37	99.02	88.76	0.83	0.72
	PET	7.26	51.4	0	0	0	41.34	55.42	53.33		
True label	**PE**	0	1.09	94.57	0	1.09	3.26	97.75	96.13		
	PP	0	0	0	96.8	1.6	1.6	98.37	97.58		
	PVC	0.43	0	0	0	96.33	3.24	98.89	97.59		
Total		1,880	179	92	250	463					

Table 5.5: Confusion matrices of the airborne dataset of Thyrow (HySpex) using (a) CNN, (b) RF, and (c) SVM classifiers. The recall values are highlighted in bold. Non.P: non-plastics, Other: other plastics, not existing in the scene, P: precision, F1: F1-score, OA: overall accuracy, κ: Kappa coefficient

a. CNN		**Predicted labels (%Recall)**				**P**	**F1**	**OA**	κ
		Non.P	**PET**	**PE**	**Other**				
True label	**Non.P**	99.53	0.01	0	0.46	95.73	97.59	0.96	0.76
	PET	0.13	99.87	0	0	99.87	99.87		
	PE	57.06	0	42.09	0.85	100	59.24		
b. RF		**Non.P**	**PET**	**PE**	**Other**	**P**	**F1**	**OA**	κ
True label	**Non.P**	99.99	0.01	0	0	99.99	99.99	1	1
	PET	0.13	99.2	0	0.67	99.87	99.53		
	PE	0	0	100	0	100	100		
c. SVM		**Non.P**	**PET**	**PE**	**Other**	**P**	**F1**	**OA**	κ
True label	**Non.P**	94.2	0.01	0.03	5.76	100	97.01	0.95	0.8
	PET	0	100	0	0	99.87	99.93		
	PE	0	0	100	0	99.62	99.81		
Total		13,662	748	1,062	-				

Table 5.6: Confusion matrices of the airborne dataset of Seddin lake (HySpex) using (a) CNN, (b) RF, and (c) SVM classifiers. The recall values are highlighted in bold. Non.P: non-plastics, Other: other plastics, not existing in the scene, P: precision, F1: F1-score, OA: overall accuracy, κ: Kappa coefficient

a. CNN		**Predicted labels (%Recall)**				**P**	**F1**	**OA**	κ
		Non.P	**PS**	**PE**	**Other**				
True label	**Non.P**	99	0	0.11	0.89	95.18	97.05	0.93	0.5
	PS	51.43	21.43	0	27.14	100	35.29		
	PE	37.5	0	62.5	0	93.75	75		
b. RF		**Non.P**	**PS**	**PE**	**Other**	**P**	**F1**	**OA**	κ
True label	**Non.P**	100	0	0	0	98.25	99.12	0.98	0.9
	PS	22.86	77.14	0	0	100	87.1		
	PE	0	0	100	0	100	100		
c. SVM		**Non.P**	**PS**	**PE**	**Other**	**P**	**F1**	**OA**	κ
True label	**Non.P**	84.08	1.34	0.56	14.03	91.74	87.74	0.79	0.14
	PS	88.57	11.43	0	0	40	17.78		
	PE	25	0	75	0	78.26	76.6		
Total		898	70	24	-				

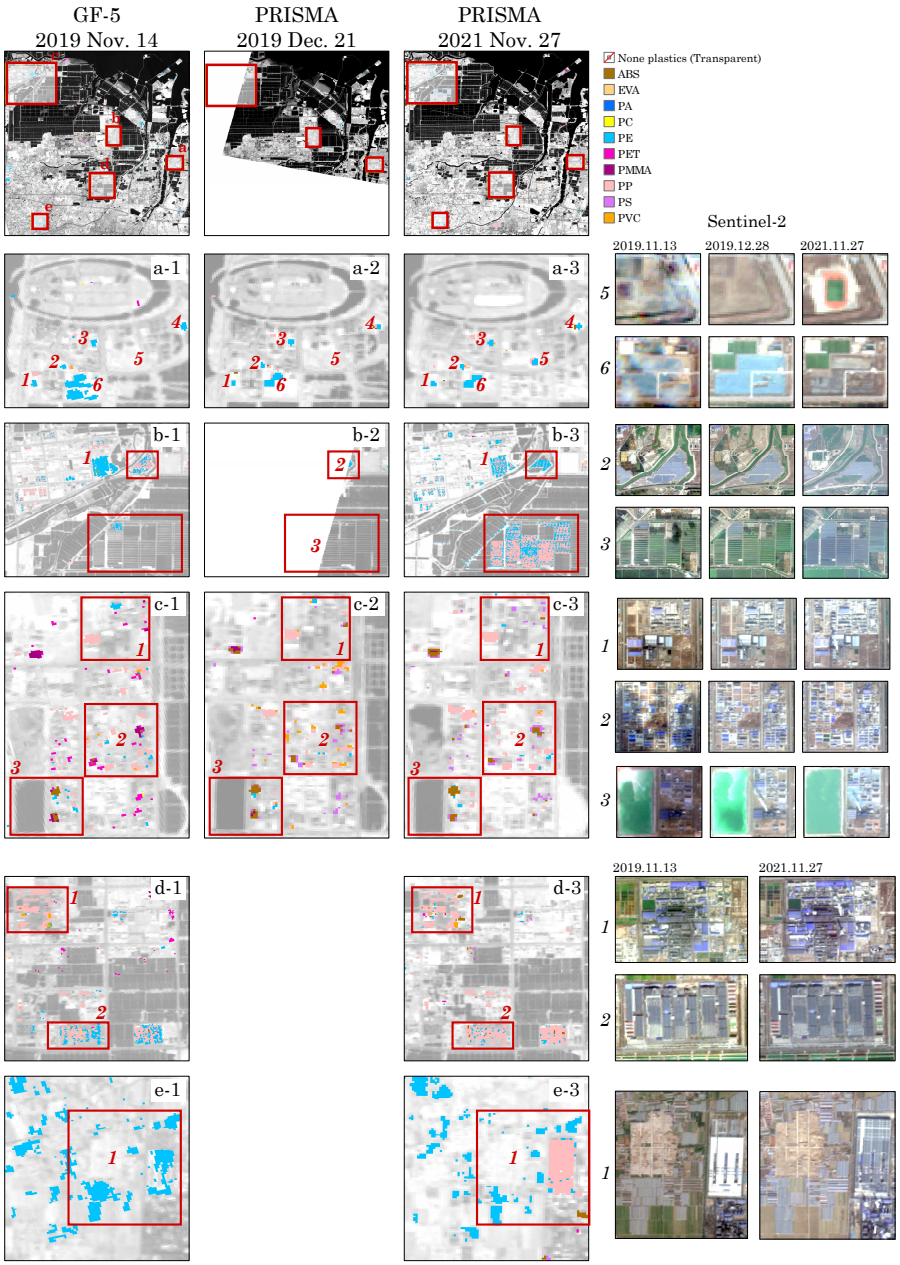

Figure 5.11: Results of the RF classifier applied to one GF-5 image recorded in 2019 and two PRISMA datasets recorded 2019 and 2021 from Weifang City, Shandong, China. Top row: Subscenes of the recorded data with comparable boundaries. Consecutive rows depict enlargements of subscenes marked in the top row mainly characterized by (a) sport fields, (b) photovoltaics (PV), (c) industrial site 1, (d) industrial site 2, (e) greenhouses. Clusters of identified plastics are superimposed to a single waveband at 1570 nm. Sentinel-2 data of nearly the same recording date as GF-5 and PRISMA are added to support the visual recognition of targets and possible changes within the two years by its higher spatial resolution of 10 m GSD. Numbers are referred to in the text. *The non-plastic class in the results is displayed as transparent to avoid masking of the background image.

also found at further locations in the satellite scene, where the respective mixed signals are obviously reflected from solar cells also called photovoltaic panels (PVs). The reason of the mixed signatures can be explained by the diversity of components embedded in PVs and used for their shielding, as well as by the diversity of materials used by the manufacturers. There are crystalline silicon cells, thin film panels, and organic cells constructed with several layers (Oreski et al., 2021), where a variety of plastic materials is used as cover (PP, PC, PMMA), for encapsulation (EVA, PO (polyolefine)), and as back sheet (PET, PP, PC, PE, PVF (Polyvinyl fluoride)). POs are polymers with the main representatives PE and PP. Both plastics are chemically quite similar and depict a rather uniform spectral behavior when scanned at 10 nm spectral resolution and sampling interval. It can be assumed that the PVs in the entire recorded region around Weifang City are very similar in construction and may also come from the same manufacturer, which explains the distinct detection of all solar panels with a mixed signature of PE and PP. Examining this slightly varying mixed signatures in the context of the minor differentiating acquisition dates with the respective sun angles as well as tilted PVs and flat on the roof mounted PVs, we cannot discern a significant correlation.

Area 2 also clearly marks the presence of PVs with some areal reduction at the north and south of the PV area in the PRISMA '21 data and easy to validate by the Sentinel-2 data. Area 3 is of specific interest, as it shows a fish farming area that, from its structure at the low resolution of 30 m GSD, looks similar to PVs. Moreover, only the PRISMA '21 data exhibit an extensive areal sprawl of PEs. Studying the project schedule of the local government reveals the construction of PVs over the water surfaces of the fish farm started in March 2021. The water below is used for fish and shrimp farming, while the PV panels provide a good shielding and are utilized for energy production (`https://taiyangnews.info/markets/china-pv-news-snippets-4/`). The Sentinel-2 data provide a more detailed view in terms of identifying the changing patterns. The project was completed mid of November 2021, which explains the missing signal for PE in the GF-5 '19 data.

Image sections c and d are recordings of industrial areas. The geometric patterns of the identified plastics in the GF-5 and the two PRISMA datasets show a significant consistency. The marked areas 1-3 in c1-3 indicate clear patterns of different plastics of the ABS, PE, PET, PMMA, PP, PS, and PVC type with only minor discrepancies for ABS to PMMA and PP to PVC. These slight differences in classification, mainly obvious in the PRISMA '19 data can be attributed to the classifier or are triggered by the already mentioned haze in the respective recording. According to the Sentinel-2 data, the signals are coming from targets like roofs of factory buildings and storage, encapsulated large boilers and pipelines and further not identifiable materials found in industrial plants. Changes in appearance of the one or other target in the different recordings can be explained by respective renovations on the ground indicated by the Sentinel-2 data. A similar situation is found in area 1 of image section d, where only very minor discrepancies occur in connection to ABS and PET. The reciprocal appearance in the d-1 and d-3 recordings may be explained by changes on the ground indicated by Sentinel-2 data. Area 2 in this image section d shows widespread PVs on the roof of large workshops of a tire factory, that are mapped clearly in great detail by mixed signals of PE and PP for both satellites, where in this case GF-5 tends more to PE and PRISMA more to PP. PA, commonly named Nylon, is only present in a few pixels within the industrial sites. Although it is found in households and the industry it is mostly used in small scale applications.

Image section e, located south-west of Weifang City is an agricultural area characterized by numerous wide spread greenhouses. These are mainly built of PE films at the roof and partly of plates of PE and/or PC at the upright sidewalls and of PP pipes as supporting structures. In our case, the RF classifier detected PE without exception, indicated by the cyan color assignment in the imagery. There are obvious differences in the patterns of GF-5 '19 and PRISMA '21 data, but those can be explained and validated on the basis of the Sentinel-2 recordings. The greenhouses are partly not immobile over a longer period of time and are moved occasionally for whatever reason. Area 1, a larger storage building located in the middle to the right of the image section e-1/3, changed the material from PE to PP between the years '19 and '21 according to the respective GF-5 and PRISMA recordings. But there are no significant misclassifications, as the roof was refurbished, which is visualized by the Sentinel-2 data.

In principle, it can be stated that the RF classifier produced very good and reliable results for the data of both sensors. The results do not reveal any significant clues about the differences in the spectral resolution, the effective spatial resolution, the SNR estimations (see Table 5.2) and probable preprocessing and resampling procedures. Main common plastics targets identified are associated with greenhouses, artificial sport grounds, industrial constructions and PV panels on soils, roofs, and water. To further improve the quality of the results, more endmember measurements and related training data, as well as a higher spectral resolution and sampling rate of future sensors is needed to more accurately separate the distinct absorption features of plastics. To detect garbage on land surfaces, the spatial resolution of the analyzed hyperspectral space sensors is by far not adequate and a challenge for future technical sensor developments.

5.6.5 Assessment

This study proves the feasibility of identifying different plastics on terrestrial surfaces recorded by hyperspectral sensors using machine/deep-learning models trained with lab-derived spectra. The analyses concerning the detection of various types of plastic on different backgrounds, including urban areas, grasslands and water bodies, identify the Random Forest model as the one with the most convincible performance. It achieves plausible classification results, whether applied to different aircraft or satellite systems.

The spectral reflectance characteristic of selected dominant plastic targets recorded by the four sensors investigated, is displayed together with the model's calculated importance of each wavelength in Fig. 5.12a-e. Considering the spectral curves recorded by the HyMap sensor (Fig. 5.12a), and despite the fact that PVC/PE/PP depict rather comparable features here with only subtle differences, the trained Random Forest model succeeded with high accuracies (Table 5.4b). In contrast, more than 30% of PET in the ground truth map are classified as other plastic types, which may result from the smoothing of the serrated feature at 2200 nm due to the coarse spectral resolution of only 15 nm. The results concerned with the HySpex recordings are in contrast quite well and balanced (Table 5.5 and 5.6; Fig 5.12b). The two spectra (PE and PP) extracted from the GF-5 and PRISMA satellite recordings (Fig. 5.12c, d) are taken from the imagery displayed by Fig. 5.11a, site 3. Very consistent classification results are derived in all three recordings, regardless of the sensor type or recording time.

When comparing these satellites derived spectral curves of PE and PP with the curves in the spectral library (Fig. 5.11), the classification results are still consistent considering the double absorption peaks of PE at around 1700 nm clearly reproduced in the 10-11 nm

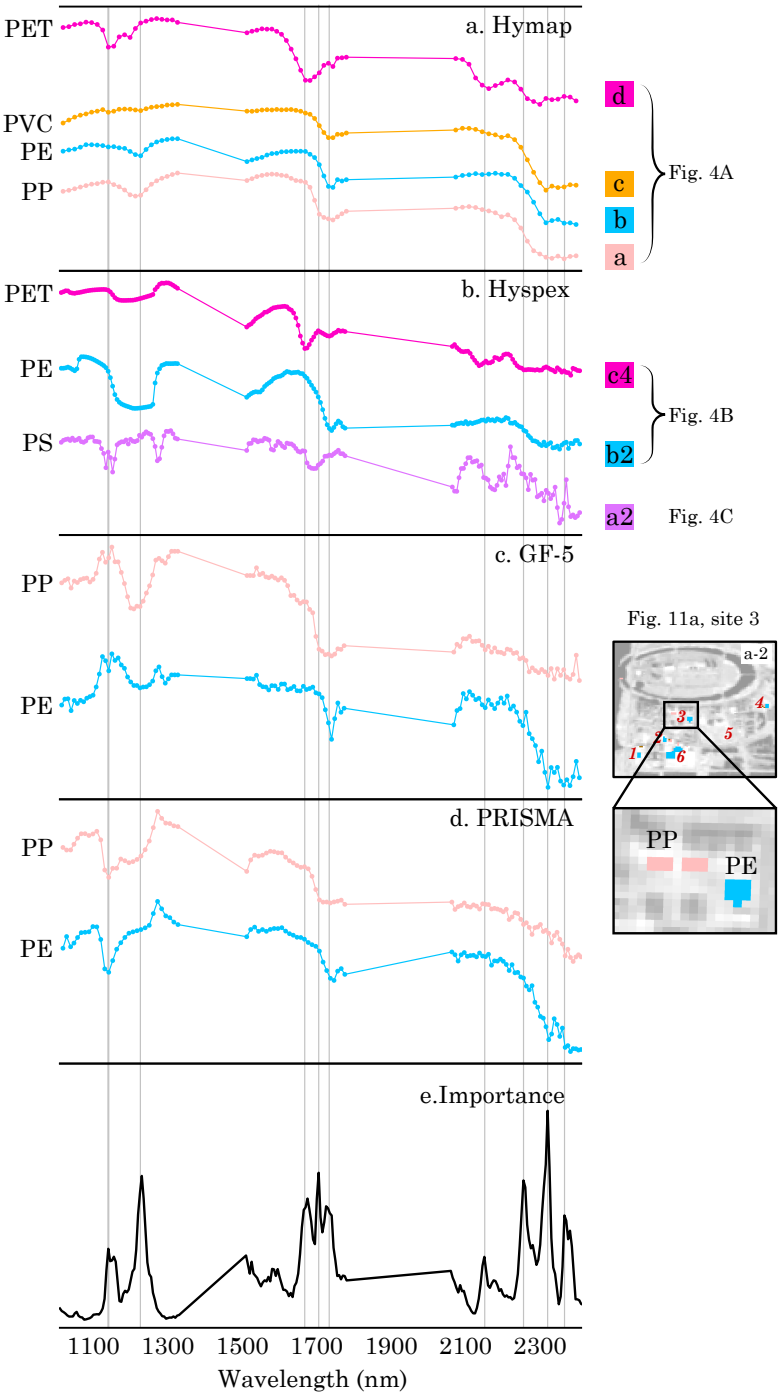

Figure 5.12: Stacked plot of spectra of plastic targets recorded by (a) HyMap, (b) HySpex, (c) GF-5 and (d) PRISMA. The sampled location is referring to Fig. 4 and Fig. 11. (e) Dimensionless feature importance along the wavelength. Water absorption bands are masked out (1320-1500 nm and 1770-2050 nm).

spectral resolution of both satellite sensors. However, the PE and PP spectra derived by the data of the two satellite systems show somewhat different shapes within the 1100-1300 nm range. This may be partly attributable to the atmospheric correction procedures that are accomplished once by the provider (PRISMA) or inhouse (GF-5). Nevertheless, the RF model classified them 'correctly', as the relevant absorption features are still more or less strongly depicted. This could be the benefit of the voting system of the Random Forest model.

When focusing at the wavelength importance of the trained Random Forest model, we note that the higher importance wavelength ranges are in accordance with our in-depth investigation of the plastic molecular structure in Section 5.3.1. This indicates that the model has learned some fundamental features, which leads to a higher transferability concerning different sensors and various scenarios.

With all advantages of the trained classifier, there are also limitations to be mentioned. According to Fig. 5.7, only when the abundance exceeds 20%, the trained Random Forest model can reach the F1 score of 0.8. This may not be enough to detect real plastic litter since this is generally sparsely distributed and rarely accumulated on larger areas. With the coarse spatial resolution of 30 m x 30 m of today's hyperspectral satellite systems, plastic waste can hardly be detected. Furthermore, spectral features of weathering or degradation processes of plastics need to be more involved in the model, as these are usually associated with broken chemical bonds. Neglecting them may lead to failures in classification.

For the future it is planned to investigate those weathering issues, to research the quantification capability using hyperspectral satellite sensors and to fuse them with multi-source data for intelligent object-based identification. Besides, we tend to focus on a diversification of our present workflow to other targets. The model trained in this study is dedicated to identify different plastics types with high precision and is incapable of detecting other materials. However, the workflow to build training datasets, as described in section 5.5.1 could be generalized in classifying any materials with inter-class similarities. E.g., by switching the spectral collection of minerals into the target pool and treat plastic as background materials, one can train a new model focusing on the differentiation of various minerals as well as mask out non-minerals.

5.7 Conclusion

This study demonstrates the feasibility of using machine/deep-learning models trained with laboratory derived spectra to identify several distinct types of plastics on terrestrial surfaces in controlled laboratory experiments and in hyperspectral recordings of different aircraft –, and satellite sensors. We proposed a conventional random mixing strategy to synthetically generate training and test datasets from endmember spectra using spectra of 10 different plastic types and numerous non-plastic materials (background) obtained from an inhouse and three public spectral libraries. Three widely used deep -, and machine learning algorithms comprising CNN, RF, and SVM were trained and compared in their performance using the synthesized spectra. The evaluation of the performance of the three models is based on the test dataset, the laboratory experiments, and three aircraft images recorded by different hyperspectral sensors in Germany. Thereby, the trained RF classifier behaves most robustly and reliably, also against noise and conditions concerned with unknown plastics and unknown background surfaces. Though the RF model is only one of

a variety of classifiers in our study, it outperforms the CNN and SVM models specifically designed for this task and trained on the same dataset. Finally, the RF classifier was applied to three satellite recordings of Weifang City in China taken at different times and dates by two different hyperspectral systems, the GF-5 and the PRISMA. The classification results derived from data of both types of sensors with comparable nominal specifications are excellent for plastic materials which form larger, homogeneous surfaces on the ground when considering the relatively low spatial resolution of 30 m GSD. The evaluation of the results also indicates that the chosen concept to diagnostically detect plastic enables the transferability between different sensors despite of inevitable preprocessing procedures, and is an essential approach when ground truth data are difficult to collect.

6 Identification of plastic functions using hyperspectral PRISMA and Sentinel-2 satellite data

This chapter is submit as:
Zhou, S., Mou, L., Hua, Y., Zhang, L., Kaufmann, H., & Zhu, X.X. . Can we use deep learning models to identify the functionality of plastics from space?

6.1 Abstract

Pollution from plastics is becoming an increasingly important issue, and the function of plas-tics in particular determines whether they need to be recycled. This study proposes a two-stage workflow to explore the feasibility to identify the functionality of plastic materials on land surfaces using deep learning models trained with Sentinel-2 satellite imagery. First, a pre-existing classification map including 10 distinct types of aromatic and aliphatic plastic materials was obtained by evaluating hyperspectral PRISMA data. Then, based on the RGB information extracted from Sentinel-2 images, different deep learning algorithms are used to assign functions to the initially classified plastic targets. Therefore, the functions of a total of 1,645 plastic polygons were carefully evaluated and manually labeled on Sentinel-2 RGB imagery in collaboration with existing high-resolution imagery and on-line information. To have a sufficient variety and number of different plastic materials available, we chose a coastal area in Weifang City, Shandong Province, China as study area. Here we found 5 major distinct functionalities, namely plastic cover sheeting for construction areas, greenhouse structures, photovoltaic panels (PVs), roof materials, and sport field floorings. By comparing three state-of-art deep learning models including GoogLeNet, VGGNet, and ResNet as well as different depth among each type of networks, an overall accuracy of 78% was achieved on the test dataset using a VGG-13 net. To evaluate the model's performance, several metrics were used, including accuracy, F1 score, precision, and recall. The results indicate that the model performs well in identifying PVs, greenhouses and covered construction sites, with F1 scores of 0.85, 0.77, and 0.71, respectively. This is beneficial for practical applications, where the identification of PVs can provide information about the development and utiliza-tion of clean energy, while the detection of greenhouses and construction sites is just as im-portant, as these are the most likely sources of plastic waste among the five functional types. The model's performance in identifying roofs and sport field floorings was lower, with F1 scores of 0.57 and 0.59, respectively. This is probably due to a high mutual visual similarity of these plastic functional areas, their fundamentally small size as compared to the used sat-ellite imagery, and the relatively low sample number of these categories. Overall, the results suggest that the proposed workflow is effective in identifying the functions of plastic mate-rials on land surfaces using deep learning algorithms trained on Sentinel-2 satellite imagery. This study contributes to the advanced use of satellite imagery in addressing global plastic (waste) management issues.

6.2 Introduction

Since their widespread introduction in the 1930s, plastic products are increasingly dominating the market, thanks to their low weight, waterproofness, and durability characteristics (Feldman, 2008). The production of plastic has quadrupled over the past four decades (Geyer et al., 2017). Improper disposal of plastic waste, along with its longevity and durability, have caused its extensive accumulation in terrestrial and aquatic ecosystems (Derraik, 2002). This leads to an extensive environmental damage to wildlife (Browne et al., 2008; Uhrin and Schellinger, 2011) and its habitats (Lebreton et al., 2017). The disintegration of plastic in the presence of ambient solar radiation releases the greenhouse gases methane and ethylene, contributing to climate change and global warming (Royer et al., 2018; Vishwakarma, 2020). With the growing awareness of the effects of plastics on

ecosystems and human health, plastic pollution is becoming a more prominent issue (Law, 2017). Plastic detection and monitoring will be a commitment for the future to identify the sources, traces, functions, and the evolution of plastics waste.

In this context, remote sensing offers itself as a very promising technique for the monitoring of plastic materials. Mapping and quantification of marine and coastal plastic based on remote sensing data (NIR, SWIR, TIR) has been well researched (Goddijn-Murphy and Williamson, 2019; Moy et al., 2018; Topouzelis et al., 2020). However, 80% of the marine plastic waste originates on land and only about 20% is directly introduced into the ocean (Li et al., 2016). Thus, it becomes increasingly important to monitor terrestrial plastic regularly to prevent further pollution. Yet most studies have focused on the differentiation of various plastic types by infrared spectra based on laboratory measurements (Moroni et al., 2015; Moshtaghi et al., 2021; Topouzelis et al., 2021). Only a few studies have used remote sensing data for single-class detection of plastics (Heiden et al., 2007; Kühn et al., 2004; Wetherley et al., 2017) and multi-class classifications on land surfaces (Zhou et al., 2021, 2022). Although plastic types are categorized, their functions cannot be directly assigned based on the chemical bond alone, but the designation of functions will help determine whether these plastic materials need to be recycled. The aforementioned pixel-level processing techniques that assign each pixel to one of the categories based on its spectral information are not sufficient to the functionality of e.g., plastic materials. The spectrally derivable information of a distinct plastic type does not necessarily correspond to the function of the respective plastic material. Plastic products with the same function can be made of different plastic types and vice versa, or even have different appearances. For instance, the photovoltaic panels (PVs) are mixtures of various plastic materials (Oreski et al., 2021) and roofs can have different colors and shapes. Thus, contextual information (in spatial domain) ought to be integrated additionally into classifiers to further differentiate the utility or function of a plastic-covered areas.

Deep learning (DL) has recently emerged as a discipline used in remote sensing and Earth sciences and is increasingly used for satellite image classification including scene identification, land use and land cover (LULC) classification, and object detection (Ma et al., 2019a; Zhu et al., 2017). For spectral-spatial classification, deep learning models is one of the most preferred option, as it allows simultaneous input of spectral and spatial information. However, the spatial resolution of data provided by currently operating hyperspectral satellites is generally low (about 30 m GSD), which leads to difficulties in extracting contextual features. Another possibility is to use the classification results of the hyperspectral dataset to locate the plastic coverage area. With a known distribution of plastic in an area, an alternative satellite image with higher resolution is used to determine its respective function. Open-access Sentinel-2 satellite images with 10 m GSD have a great potential in this case.

A Convolutional Neural Network (CNN) is such a type of deep learning algorithms that is designed to work with image data (LeCun et al., 2015). It has proven to be very effective in image classification and object detection tasks, as it is able to capture both local and global features in an image. CNNs are widely used in remote sensing applications (Ghanbari et al., 2021), mainly for land cover classification and object detection from satellite imagery. They are robust concerning their architecture, which includes local receptive fields, shared weights, and subsampling (Kattenborn et al., 2021). The local receptive fields allow CNNs to focus on small, localized regions of an image and extract features from them, while shared weights allow networks to learn features that are useful

across multiple regions of the image. Subsampling is a process of down-sampling the feature maps, what helps to reduce computational complexity and improve the stability of networks. Together, these architectural elements help to make CNNs robust to changes in the input data and to variations in imaging conditions, such as changes in illumination or viewpoint. This allows CNNs to generalize well to new data and produce consistent results, demonstrating their effectiveness and robustness for image analysis tasks in remote sensing applications.

This study is the first to investigate the potential of satellite imagery to differentiate the utility functions of land-based plastic products. To meet the objective, a two-stage workflow was applied.

1) The generation of a plastic type classification map based on hyperspectral satellite data (PRISMA) provides the type and location of the plastic materials, which is achieved based on the methodology proposed in our previous study (Zhou et al., 2022).

2) The assignment of respective functions of these classified plastic materials is based on Sentinel-2 images using three state-of-the-art deep learning models of varying depth.

6.3 Materials

6.3.1 Study area

The study area depicted in Fig. 6.1 is located in the north of Weifang City, Shandong Province, China (N 37°5′20.4″, E 119°7′30″). It encompasses agricultural, residential, and industrial regions, with agricultural fields primarily located in the southwest of the selected area. The region is known for its thriving agriculture, with plastic greenhouses, mostly made of polyethylene (PE), polypropylene (PP), and polycarbonate (PC), covering around 20% of its total cropland (Rasheed et al., 2020). The rapid pace of urbanization in the region, driven by the local government, is especially accentuated by an increased investment in green energy, specifically in PVs built by layers of different plastic materials such as PP, PE, and ethylene vinyl acetate (EVA) (Rasheed et al., 2020). The high coverage and diversity of plastic products in Weifang City, including the greenhouses and photovoltaics, and further objects such as roofs, sport field floorings, and sheeting materials connected to construction zones, make it an attractive research area for evaluating the feasibility of predicting functions to different plastic materials based on satellite images.

6.3.2 Plastic type map

The feasibility of using hyperspectral satellite data and machine learning models to distinguish various types of plastic materials present on terrestrial surfaces has been explored. We trained the models using lab-derived spectra and evaluated their performance on a test dataset recorded by aircraft and two different hyperspectral sensors (PRISMA and GaoFen). The results showed that the random forest (RF) algorithm was the most reliable model for clearly separating 10 types of aromatic and aliphatic plastics on various backgrounds, including urban areas, grasslands, and water bodies, with an overall accuracy of approximately 96% (Zhou et al., 2022). The plastic classification chart used for this study was generated from four PRISMA L2D images of 30 m GSD, two each recorded on November 27 and December 3, 2021, covering the study area depicted by Sentinel-2 imagery in Fig. 6.1. The trained RF classifier from our previous research produces an exhaustive partitioning of the set of image pixels into 11 classes, including 10 different

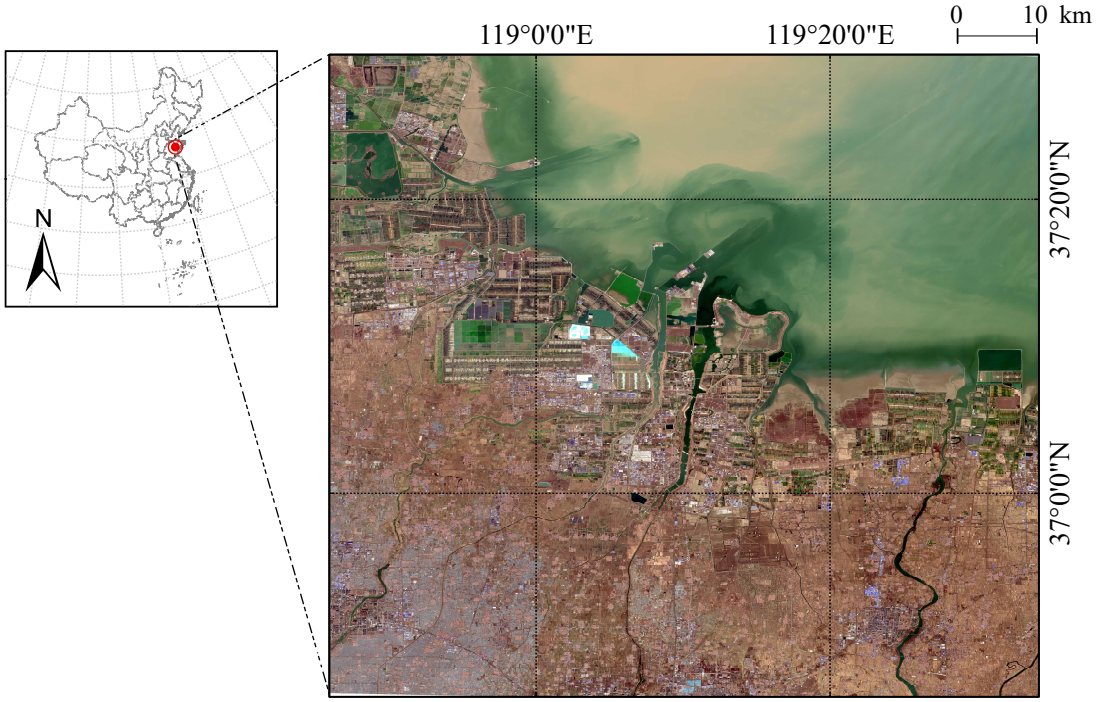

Figure 6.1: RGB image sketch of the test site Weifang City as recorded by the Sentinel-2 MSI sensor

plastic types and one non-plastic type. Based on the classification result, which achieved a high satisfactory level of accuracy, we assigned functions to each plastic pixel in the image (see details in Chapter 6.4).

6.3.3 Sentinel-2 images

The Copernicus Sentinel-2 mission comprises a constellation of two polar-orbiting satellites (Sentinel-2A/B) placed in the same sun-synchronous orbit, phased at 180° to each other. For this study, an image taken by the multispectral instrument (MSI) mounted on the Sentinel-2B was used. The image was obtained on December 2, 2021, close to the time of acquisition of the hyperspectral data from which the plastic classification map was generated. The Sentinel-2B MSI provides multispectral images with varying spatial and spectral resolutions. Detailed information about the Sentinel-2B is given in Table 6.1. To meet the requirement of a higher spatial resolution, only 10 m Level-2A surface reflectance data were considered, of which R/G/B bands were used to generate the dataset (see details in Chapter 6.4).

6.4 Methodology

We trained and compared commonly used deep learning-based classification models and tested them to automatically classify the functions of different plastic materials. An overview of the data preparation, model training and assessment in this study is depicted in a flowchart (Fig. 6.2).

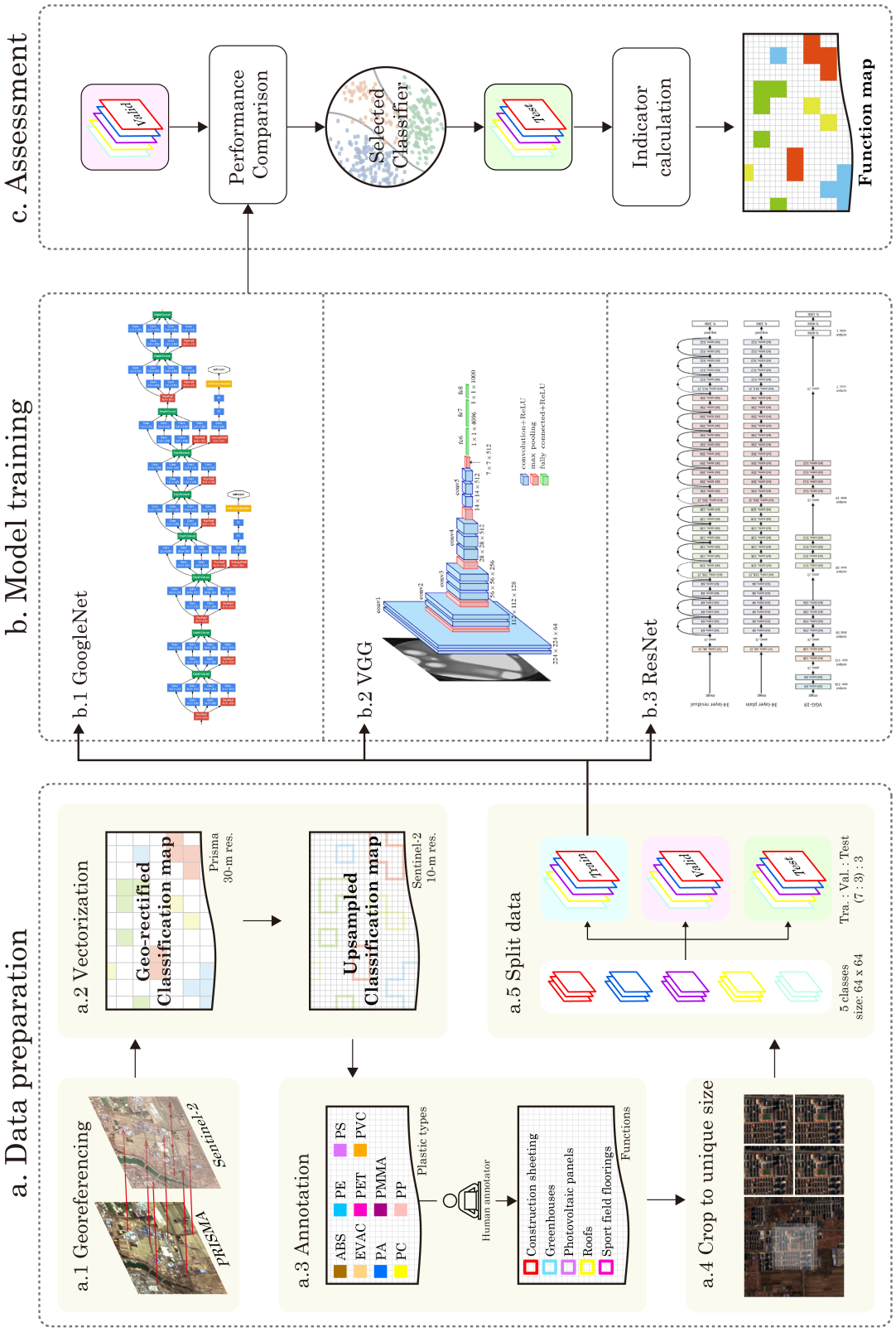

Figure 6.2: Flow chart of the evaluation concept. See text for acronyms.

Table 6.1: Main parameters of Sentinel-2B

Parameters	Value
Repeat cycle	12 days
Spectral range	443 nm to 2190 nm
Swath width	290 km
Spectral bands	13
Spatial resolutions	10 m, 20 m, and 60 m

6.4.1 Data preparation

6.4.1.1 Image registration

The classification map of plastic types is generated from four PRISMA L2D images, so both sharing the same geo-coding information. To accurately project this classification map onto the Sentinel-2 recorded data, image registration is performed to align the different datasets. Ground control points (GCPs) collected from the Sentinel-2 images are used as reference points to perform the image registration of the PRISMA L2D imagery using ArcGIS 10.8 Software. Around 30 pairs of GCPs per PRISMA L2D scene are utilized in the registration process to ensure a high degree of accuracy. Affine transform is applied. The final root mean square error (RMSE) is controlled to be less than 1, which is a measure of the overall accuracy of the image registration process. Upon the completion of the image registration, the transforms are applied to the classification map.

6.4.1.2 Up-sampling and annotation

The spatial resolution of the original classification map is 30 m, which differs from the 10-meter resolution of the Sentinel-2 image. To reconcile this discrepancy, the most straightforward approach is to vectorize the classification map from its original raster format into a shapefile format, which is comprised of polygons. This conversion process was carried out using ENVI 5.4. The resulting shapefile was up-sampled from 30 meters to 10 meters by loading it onto the Sentinel-2 dataset, which enabled its effective integration with the Sentinel-2 dataset.

The classification map categorizes pixels into 11 classes, including 10 distinct types of plastic and one non-plastic type. In this study, only plastic pixels were used. Thus, each pixel is endowed by a numerical label of the plastic type to which it belongs. However, this process does not utilize spatial information, leading to the possibility that pixels with the same label may either be connected in the image plane and form a polygon region or be disjoint from one another. During the up-sampling process, the original classification map is converted into a vector shapefile that includes multiple polygons with unique IDs. This conversion also allows for the extraction of individual plastic material regions, enabling each connected region to be assigned a label that indicates its functionality.

It is assumed that each of the polygons extracted represents a single functional unit of plastic products. A total of 1,645 polygons were extracted and manually labeled with functional information. Ground truthing for the functional information was realized by an assessment process that utilized high-resolution airborne images from Google Earth Pro, as well as local photographs (Fig. 6.2a.3). Following a careful labeling procedure, the extracted polygons were categorized into 5 major functions namely: plastic cover

sheeting for construction areas, greenhouses, PVs, roofs, and sport field floorings. The correspondence is shown in Fig. 6.3.

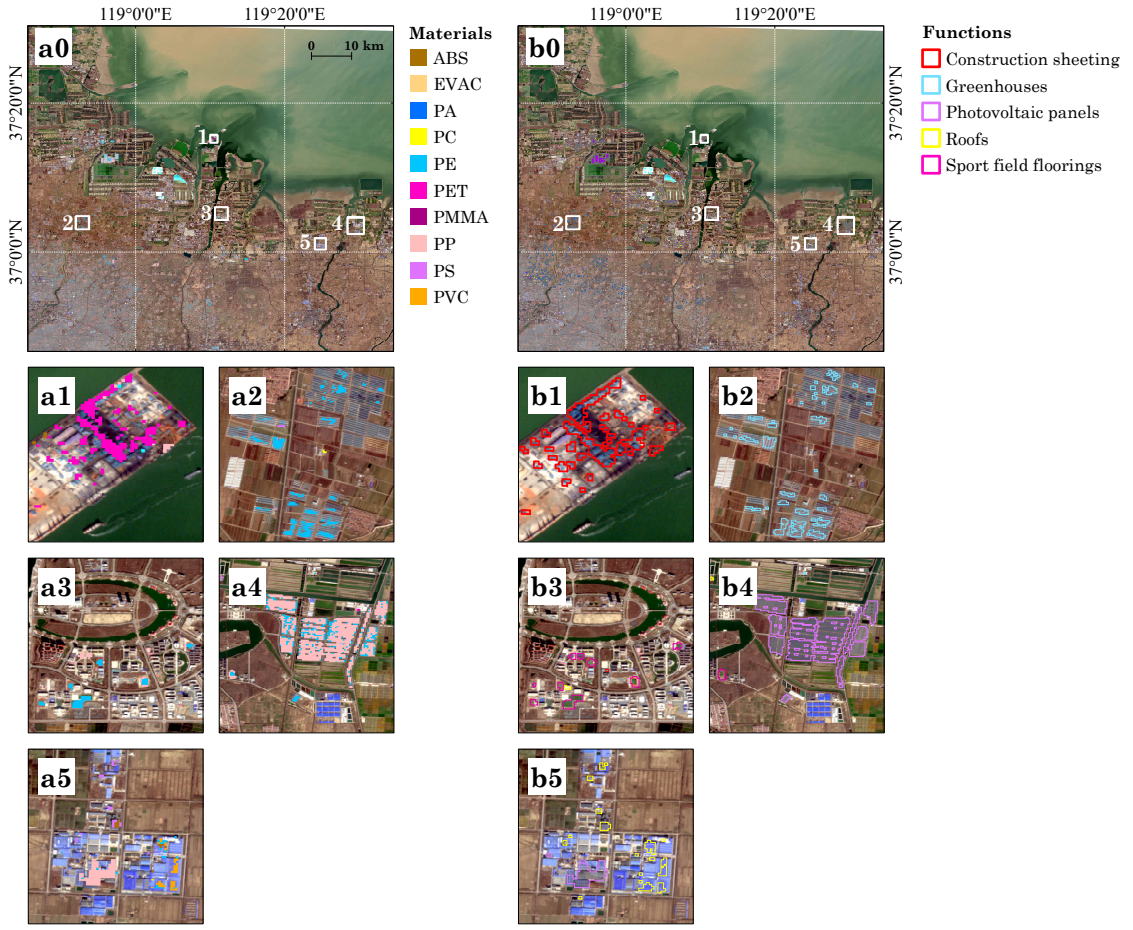

Figure 6.3: Sentinel-2 imagery superimposed with a0: a plastic type map (Zhou et al., 2022) with enlarged subscenes (a1-a5), and b0: a labeled classification map of the respective functions of plastic materials with enlarged subscenes (b1-b5). ABS=acrylonitrile butadiene styrene; EVAC=ethylene vinyl acetate; PA=polyamide; PC=polycarbonate; PE= polyethylene; PET=polyethylene terephthalate; PMMA=polymethyl methacrylate; PP=polypropylene; PS=polystyrene; PVC=polyvinyl chloride.

6.4.1.3 Patches and data split

Deep learning classification algorithms require a fixed input image size (rectangle) as they rely on CNNs, which use convolutional layers to extract features from the input data. The consistency in size allows for convolutional filters to have a standard size and shape for processing information. Furthermore, having a consistent input size helps standardize the data, reducing the need for pre-processing and simplifying the model's learning process. By using a fixed input image size, the deep learning classification algorithms can perform more efficiently and effectively, leading to an improved accuracy and performance.

As the resulting shapefile from the up-sampling and annotation process involves irregular polygons, we calculated the outer rectangle of a polygon. After evaluating the

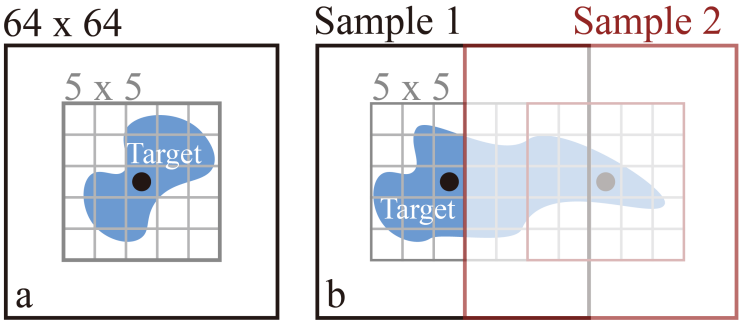

Figure 6.4: Schematic diagram of sampling for a plastic polygon when its size (a) smaller than 5×5 pixels and (b) bigger than 5×5 pixels.

Table 6.2: Number of annotated plastic sites after the cropping procedure

Function	Amount
Construction sheeting	560
Greenhouses	2190
PVs	7770
Roofs	1445
Sport field flooring	266

distribution of sizes of the outer rectangles, it was found that the size distribution of plastic products in the study area was wide-ranging, from several dozen pixels to several thousand pixels. To cater the suggestion of fixed input image size in deep learning classification algorithms, the following strategy was employed in this study (Fig. 6.4). First, a moving window of 5 x 5 pixels was used to determine the smallest polygon unit. This window was then used to crop larger polygons into smaller patches. The centroid of each cropped polygon subset was collected and used to create a bounding box with a size of 64 x 64 pixels, which served as the final input image size. By using the generated bounding boxes to crop the Sentinel-2 dataset, examples of the final samples are depicted in Fig. 6.5.

Figure 6.5: Examples of Sentinel-2 image sections of (a) construction site cover, (b) greenhouses, (c) voltaic panels, (d) pure roofs, (e) sport field

After cropping, the dataset contained 12,468 finely annotated plastic sites with 5 functional classes (Table 6.2). Each image contains information of the three MSI-channels red (R), green (G), and blue (B).

Data were partitioned into training, validation, and test sets, which is an important step in machine learning to prevent overfitting and to estimate the generalization perfor-

mance of the models. The test set comprised 30% of the dataset, while the remaining 70% was divided into training and validation sets using a 7:3 ratio. The three sets were spatially independent of each other. The final ratio of training, validation, and test dataset was approximately 5:2:3.

6.4.2 Deep learning algorithms

CNNs are a highly effective choice for image classification tasks, as they have demonstrated state-of-the-art performance on many benchmark datasets. The hierarchical representation learning ability and spatial correlation handling capability of CNNs make them particularly well-suited for image classification. These networks consist of multiple layers, including convolutional, pooling, and fully connected layers, which are responsible for extracting features, reducing spatial dimensionality, and making predictions, respectively. Models like the GoogLeNet (Szegedy et al., 2015), VGGNet (Simonyan and Zisserman, 2014), and ResNet(He et al., 2016) have proven their efficacy in various computer vision tasks and have been widely adopted in various applications. In this study, these models served as base models and were fine-tuned and compared to meet specific requirements of identifying plastic functionality from satellite images.

6.4.2.1 GoogLeNet

GoogLeNet, also known as Inception, was introduced by Szegedy et al. (2014). It is designed to reduce the computational complexity of deep neural networks through the use of inception modules. The inception modules consist of multiple parallel convolutional filters of varying sizes, which enable the network to learn multiple scales of features simultaneously. GoogLeNet introduced the concept of "Inception modules," which are blocks of network architecture that apply multiple filters of different sizes in parallel to extract information at multiple scales (Fig. 6.2b.1). This allows the network to learn hierarchical representations of the input image and reduces the number of parameters compared to traditional ConvNets with sequential layers. GoogLeNet also employs global average pooling and softmax activation functions, and uses auxiliary classifiers to improve the overall accuracy of the network. These innovations help to set the stage for further advancements in deep learning models for computer vision and have inspired many other models that have been developed since.

6.4.2.2 VGGNet

VGGNet is a deep neural network architecture designed for image classification tasks, developed by the Visual Geometry Group at the University of Oxford (Simonyan and Zisserman, 2014). VGGNet has obtained state-of-the-art results on several benchmark datasets and consists of multiple convolutional and fully connected layers (Fig. 6.2b.2). The architecture emphasizes the use of small (3x3) convolutional filters and a deep network structure with up to 16 weight layers. The Max pooling and ReLU activation functions are used in VGGNet architecture. It is a widely cited model in computer vision and often used as a benchmark for evaluating other deep learning models. In this study, VGG-11, VGG-13, VGG-16, and VGG-19 models were utilized. These models differ in the depth of the network, whereby VGG-19 has more weight layers compared to VGG-11, allowing it to learn more complex representations of the input data.

6.4.2.3 ResNet

ResNet is a deep CNNs developed by Microsoft Research (He et al., 2016) that addresses the degradation problem in deep networks. The key innovation of ResNet's structure is the use of identity shortcuts, also known as skip connections. These shortcuts allow the information to propagate directly from lower to higher layers of the network, alleviating the problem of vanishing gradients and enabling the network to learn deeper architectures with up to 152 weight layers (Fig. 6.2b.3). The use of identity shortcuts helps to improve the stability and convergence during training, as well as reducing the reliance on a careful weight initialization. This innovative structure of ResNet has been widely adopted in vision tasks and continues to deliver a leading performance on various benchmark datasets.

6.4.3 Training

6.4.3.1 Data augmentation

The purpose of data augmentation is to make a model more robust to unseen data by forcing it to learn from multiple variations of the same images. By using augmented data in the training procedure, the model is better generalized and over-fitting to the original training data is avoided. In this study, random transformations including flipping, scaling and cropping are applied to training data. It is also common to perform the normalization on data before the augmentation step. The normalization helps center the data and can make it easier for the model to learn from the augmented data. In this study, normalization is applied to each channel of images independently, using the mean and standard deviation calculated from the entire dataset, including training, validation, and test sets.

6.4.3.2 Model tuning

Choosing right loss function is of major importance for model training. The negative log likelihood loss (NLL Loss) was utilized for all models applied. This loss function is widely used in supervised learning and is especially suitable for multi-class classification problems (MIRANDA, 2017). As shown in Table 6.2, our dataset exhibits a class-imbalanced distribution. Therefore, the weight of each class in the loss function was adjusted. To further enhance the performance, the log-softmax function was employed in conjunction with the NLL Loss. This activation function encourages the model to predict high probabilities for the correct class, providing a well-behaved optimization objective (Vincent et al., 2015).

The log-softmax activation was applied in the last fully connected classification layer of all models. The Adam optimizer was used for training, which is known for its efficiency and effectiveness. The hyperparameters, including learning rate, batch size, training epochs and drop-out rate were adjusted in this study. This involved a process of fine-tuning the pre-trained ResNet, VGGNet, and GoogLeNet models, which were trained on the ImageNet dataset, to achieve the best performance. The optimal settings were determined independently for each model, through experimentation with different combinations. All models were implemented in PyTorch 1.12.1 using Python 3.8. All neural networks was trained with three NVIDIA Quadro P4000 GPUs, each with 8GB of memory.

Table 6.3: Overall accuracy and Kappa coefficient of all models calculated on the test dataset. OA: overall ac-curacy, κ: Kappa coefficient.

Models	OA (%)	κ
GoogLeNet	68.63	0.50
VGG-11	73.74	0.62
VGG-13	78.13	0.66
VGG-16	76.56	0.63
VGG-19	74.54	0.59
ResNet-18	72.32	0.56
ResNet-50	73.02	0.57
ResNet-101	76.36	0.63
ResNet-152	77.32	0.64

6.4.4 Evaluation

For the evaluation of the models, confusion matrices based on true labels were derived. Statistical indices like recall, precision and overall accuracy (OA) were employed to determine the reliability and generalizability of classifier in categorizing the function of plastic materials when applied to both validation and test sets. The F1-score were obtained by calculating the harmonic mean of recall and precision to avoid bias from imbalanced ground truth. The higher the F1 value the better the performance. Additionally, Cohen's kappa coefficient was considered to estimate the consistency and robustness of classifier.

6.5 Results

Each model was fine-tuned individually by learning rate, batch size, training epochs and drop-out rate. For all selected depths of the three deep learning models, those parameters that showed the highest accuracy for each model in the validation dataset were used to evaluate the test set (Fig. 6.2c).

6.5.1 Model comparison

The classification performance of all models is evaluated by the overall accuracy (OA) and the kappa coefficient on the test set (Table 6.3). All these standard models provide an OA over 68%, giving a positive answer to the question of whether it is feasible to use satellite images of 10 m GSD to predict the respective functions to hyperspectrally identified plastic materials.

The GoogLeNet achieves the lowest OA value of all models at 68.93%. For ResNets, it shows that the accuracy increases with the depth of the model, and the OA is highest when using ResNet-152, reaching about 77%. For the VGGNets, the accuracy increases with the greater depth first, followed by a consecutive decrease. The best OA value of all models was reached by VGG-13 at 78%. In contrast, the lowest overall accuracy on the test dataset was reached by the GoogLeNet model (¡70%) indicating that this model may not be as effective as the other models in predicting the function of plastic materials in the study region. Furthermore, these results highlight the importance of selecting the appropriate machine learning algorithm for multi-class classification tasks.

The Kappa coefficient provides a measure of the agreement between the predictions made by the models and the ground truth labels, adjusted for chance agreement. A kappa

Table 6.4: Confusion matrix of the 5 function types of plastic materials calculated on the test dataset using the trained VGG-13 model. Constr.: construction sheeting, G.houses: greenhouses, Sport: sport field flooring. Recall values are highlighted in bold. P: precision, F1: F1-score

		Predict label (% Recall)					P	F1
		Constr.	**G.houses**	**PVs**	**Roofs**	**Sport**		
	Constr.	62.88	7.20	25.38	3.79	0.76	81.77	71.09
True	**G.houses**	0.88	74.01	18.83	5.26	1.02	79.47	76.64
	PVs	0.60	6.44	88.32	4.64	0.00	82.57	85.35
label	**Roofs**	6.94	4.10	18.30	55.84	14.83	58.80	57.28
	Sport	0.00	1.94	26.21	7.77	64.08	54.10	58.67

coefficient higher than 0.60 is generally considered to indicate a substantial agreement between the predicted and actual classifications, indicating that the model is effectively distinguishing between the different classes. Among all models, the VGG-13, VGG-16, ResNet-101, and ResNet-152 exceeded 0.6. among them, the highest Kappa coefficient reached 0.66 when using VGG-13. In summary, the VGG-13 model showed the best performance in both the OA and Kappa coefficient.

6.5.2 Confusion matrix calculated on the test dataset

To gain a more detailed understanding of the best model's performance, a confusion matrix of the trained VGG-13 model was calculated, shown in Table 6.4. This reveals, that the number of samples in each class varied significantly (Table 6.2). The imbalance of categories may in-fluence the performance of the classifier as it might have learned to prioritize those catego-ries with a high number of samples at the expense of categories based on a lower number of samples. To address this issue, we used class weighting in the loss function during model training, with weights of 2, 2, 1, 3, and 9 for the plastic sheeting for construction site covers, greenhouses, PVs, roofs, and sport field floorings, respectively. The weighting helped to bal-ance the importance of each class in the training process, potentially improving the classifi-er's performance on classes provided with a lower number of samples.

The diagonal values in the confusion matrix reveal the recall rate. Examining the values in the confusion matrix, it can be seen that the model had varying levels of performance for the different classes. Of the models tested, PVs had the highest recall rate at approximately 88%, greenhouses reach 74%, while roofs had the lowest recall rate at around 56%. What the remaining classes is concerned, more than 18% of samples were falsely classified as PVs. As for the roof materials, about 14% were misclassified as sport field flooring. In terms of precision and F1 score, these scores provide insight into the classifier's ability to identify instances for each class and balance.

Starting with the plastic sheeting for construction areas, we observe a high precision score of 0.82 and an F1 score of 0.71, indicating that the model is able to correctly identify instances for this class with high accuracy while maintaining a reasonable balance between precision and recall. This suggests that the classifier is effective in distinguishing the plastic sheeting for construction area from other functions, which is an encouraging result. The precision score for greenhouses is 0.79, and the F1 score is 0.77, which are slightly lower than those of the first function type but still in the range of high precision and a good

balance between precision and recall. This suggests that the classifier still works well in identifying greenhouses.

For PVs, we observe a high precision score of 0.83 and an F1 score of 0.85, which is similar to that of the construction area sheeting. This indicates that the classifier is similarly effective in distinguishing PVs from other classes while maintaining a high balance between precision and recall. All in all, these results make it clear that the classifier is performing well in identifying instances for the plastic sheeting for construction sites, greenhouses and PVs.

The precision and F1 scores for roof materials and sport field floorings are somewhat lower than those of the other classes. The precision score for roofs is 0.59, with an F1 score of 0.57, and the values of sport fields are 0.54 and 0.59, respectively. These results indicate that the classifier is not as effective in recognizing these two categories, also showing a significant imbalance between precision and recall. This further implies the need for a potential improvement in the classifier's performance concerning these categories. Thus, further research is necessary to identify the reasons for the varying levels of performance and to develop strategies for an improvement.

6.6 Discussion

6.6.1 Assessment

The results of our study demonstrate the feasibility of using deep learning frameworks based on Sentinel-2 satellite images for a viable functional classification of plastic objects. The VGG-13 model achieved the highest overall accuracy, with the PVs category exhibiting the best precision and F1 scores, suggesting that the model is very effective in distinguishing this functional category from others. The accurate identification of solar panels (PVs), by our model approach can provide precise information for the development and utilization of clean energy, thus contributing to environmental protection and a sustainable development. The high-grade identification of greenhouses and construction site covers is also essential, as these are the most likely sources of plastic waste among the five elaborated functional classes. The model achieved the second and third highest precision and F1 scores for these categories, and thus, can help guiding environmental management and policy-making. The precision and F1 scores for roofs and sports fields are of viable quality, whereby the lower results may be attributable to the high visual similarity of the plastic functional areas and/or the relatively few amount of samples of these categories. Future research could focus on increasing the sample number of these classes and investigate the performance of the model under different hyperparameters. Our findings also underscore the importance of using appropriate weights in the loss function, with the highest weight given to the sport fields category due to the limited number of samples.

Overall, the results of the analysis of the indicator matrices provide valuable insights into the performance of the classifier on the test dataset. The findings suggest that the classifier is effective in identifying specific functions, while there is potential for improvement in identifying other classes.

6.6.2 Visualization

As mentioned in Section 6.4.1.3, the original plastic objects were cropped by a 5x5 pixel window, thus, there can be several predictions for one larger plastic object. To solve this

issue, we determined the final assignment of the function of each entire plastic object by means of a voting procedure. Thereby, the plurality of the model's predicted values for all subsamples will be the predicted value of the plastic object.

Fig. 6.6 shows representative subscenes of the ground truth map (left) and the final function map (right) generated based on the VGG-13 and voting procedure. In the subscenes a/b1 most of the polygons of construction sheeting are assigned the right functionality. The few misassignments as greenhouses or roofs are due to smallest polygons. For subscenes a/b2 greenhouses and a/b3 sport field floorings also large area polygons are misjudged while the respective ground truth map does not show any significant difference to the remaining ones. Photovoltaic panels a/b4 are classified very accurately, only again one small area polygon is misassigned as construction sheeting. Roofs are depicted together with minor PVs in subscene a/b5. Roofs are generally of smaller size and especially those with the smallest extension are again misassigned here. The results of all functionalities in the subscenes are representative for the entire classified Sentinel-2 scene, what can be inspected by zooming into it.

There is a clear trend to misassignments of functions when training targets are to small, mostly because of their natural structure such as roofs or sport fields. A suitable solution may be found in (future) higher resolving remotely sensed data. What the larger misclassified training targets is concerned, there is no obvious difference to those correctly assigned. Here an improvement can be achieved by additional training data.

6.6.3 Challenges and limitations

Although this study has demonstrated the feasibility of using deep learning models for plastic functional recognition, there are also challenges and limitations that need to be addressed. The main challenge is the limited availability of labeled data. To train deep learning models more effectively, a large amount of labeled data is required, especially for collecting samples from roofs, sport fields and eventually additional categories. This could be a major challenge for a global monitoring approach, as plastic materials with the same function in different regions may have different forms or surrounding environments. Therefore, a large number of diverse samples is needed to represent this inter-class diversity, although accurate labeling of samples requires a considerable amount of time and effort.

Besides, we used pre-trained weights for all model initializations. While this contributes significantly to the accuracy improvement of the model, one is limited to using only RGB images (real color composites) as input, although other spectral bands might be more suitable. When not initialized with pre-trained weights, the best overall accuracy of the model is only about 46% based on the dataset used in this study. A large amount of training data is further needed in order to get rid of the pre-trained weights. This way, the input can also be extended to more bands present in the Sentinel-2 data and the plastic type information obtained from the hyperspectral analysis can also be used as an additional band.

Another limitation of this study is that, although the training, validation and test datasets were spatially independent of each other, they are for feasibility reason all located in one study region in the Shandong Province. This may limit the generalizability of the models, as their ability to generalize to unseen areas cannot be fully assessed. Thus, future works could explore the model's performance on datasets with more diverse spatial distributions.

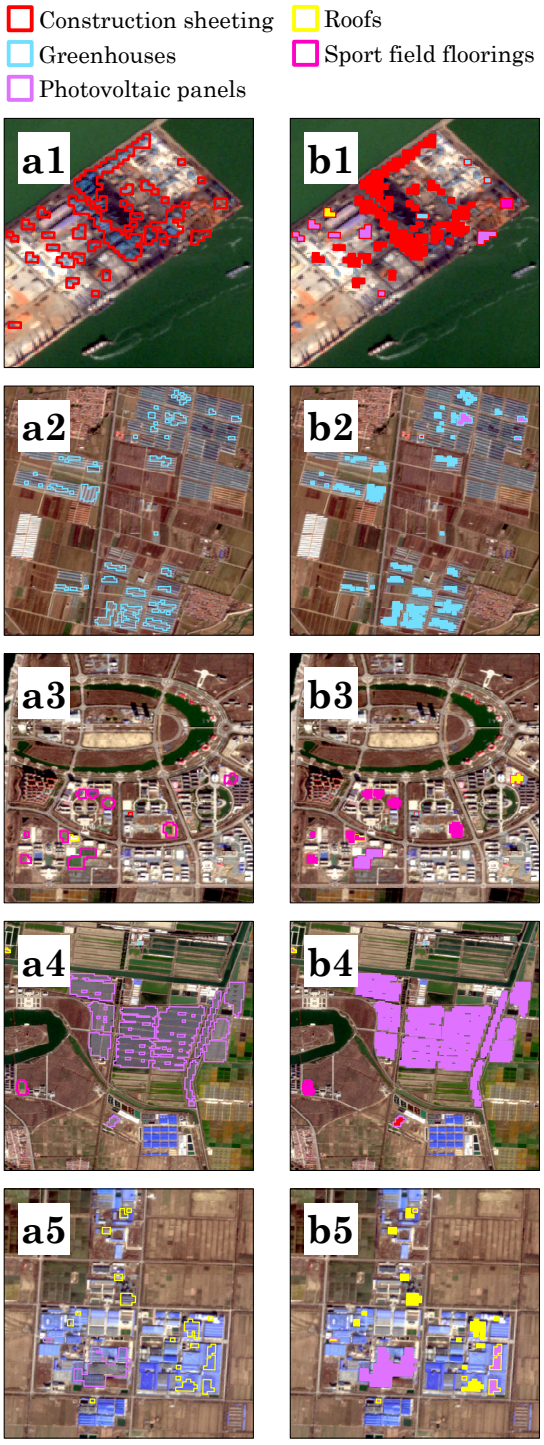

Figure 6.6: Enlarged subscenes of Sentinel-2 imagery, (a1-a5) superimposed with the ground truth map of the respective functions (colors) of plastic materials in polygons, and (b1-b5) with filled polygons as a result of the function assignment using the VGG-13 model. Misclassifications are depicted when the colors of polygons and fillings are differing (e.g. top b2; bottom right b5). Only polygons included in the test dataset are displayed.

The requirement for prior knowledge of plastic distribution through hyperspectral imaging introduces additional challenges to the automation of plastic functional recognition. This is because the collection and analysis of hyperspectral data is time-consuming and requires specialized expertise to ensure accurate identification and classification of plastic materials. Furthermore, the need to register the basic plastic classification map with the Sentinel-2 image each time the model is applied can be a time-intensive process, further limiting the efficiency and scalability of the plastic recognition system.

To overcome the challenges and limitations mentioned above, further investigations could be conducted to either develop end-to-end models that do not require prior knowledge of the plastic distribution or to simplify the registration process of classification maps with Sentinel-2 images. These advances can contribute to the overall goal of reducing plastic waste and promoting sustainability through improved plastic functional recognition and management.

6.6.4 Outlook

For our ultimate goal of identifying plastic functionality, the aim is actually to use satellite imagery to identify non-functional plastic waste that needs to be cleared. We think our approach has the potential to be a valuable tool in addressing this goal, but what plastic waste is concerned, there is a dependency on a number of future technological and methodological developments.

First of all, plastic waste is usually distributed in small quantities, so, to be able to detect them, there is a need of hyperspectral systems with better spatial resolutions than those presently available at 30m GSD. Moreover, future research in artificial intelligence should focus on developing deep learning models specifically made for the recognition of plastic functionality, and the availability of more labeled data with higher spatial resolutions for training of these models. Data of high-resolution commercial satellites can be a solution, and may improve the level of details captured and thus, enhance the classification accuracy, but the data of those presently operating are rather expensive with a limited availability.

In our future research, we aim to develop an end-to-end deep learning model for functional classification of plastics. We plan to collect and label more samples recorded by different sensors and we intend to integrate this classifier with multiple sources of data to achieve more intelligent recognition capabilities. Our ultimate goal is to improve the overall performance and applicability of the classifier, and to make further significant contributions to the field of plastic (waste) management.

6.7 Conclusion

As a follow-up task to our two previous works, this study demonstrates the feasibility of using deep learning models trained on satellite imagery to identify the functionality of plastics on land surfaces. Thereby, it proposes a two-stage workflow. First, we obtained a classification map identifying 10 distinct plastic types based on the analysis of hyperspectral PRISMA satellite data with 30m GSD. Based on color composites of Sentinel's-2 red, green, and blue bands with 10m GSD a deep learning algorithm was used to assign functions to the initially classified plastic polygon objects. Five clearly salient functionali-

ties were found to be existing in the study area including plastic sheeting for construction sites, greenhouses, PVs, roofs, and sport fields.

The study demonstrates the feasibility of using a deep learning framework based on Sentinel-2 satellite imagery for the accurate classification of the functions of plastic objects, where the scores for the category roofs and sports fields show viable findings and solar panels, greenhouses, and construction site covers show best results. Near future research will focus on increasing the sample number and investigating the performance of the model under different hyperparameters. This study further highlights the importance of using appropriate weights in the loss function, especially for categories with limited amounts of samples.

The use of satellite imagery and deep learning to functionally classify plastics can aid in monitoring and evaluating their distribution and impact on the environment, providing guidance for environmental management while also providing valuable data for plastic pollution control. An accurate classification of functional plastics, such as solar panels, can enhance the monitoring and evaluation of clean energy potential and efficiency. Although, there are challenges such as inadequate spatial resolutions, the need for more tagging data and alignment of different data sources, is an important step towards addressing global plastic waste management.

7 Synthesis and outlook

7.1 Synthesis

Due to the increasing attention being paid to the impact of plastics on ecosystems and human health, there is a growing interest in using remote sensing techniques to monitor and identify plastic materials and associated wastes in the terrestrial environment. For this reason, the presented thesis examined the capability of existing optical remote sensing technologies to detect and identify various sorts of plastics. Recent developments in sensor technology, data accessibility and evaluation methods now allow the utilization of increasing amounts of data analyzable by new advanced algorithms and models. In this context, the present thesis takes an in-depth look at the potential of optical remote sensing technology to identify different types of plastics that are to be found on land surfaces. By conducting several sequential feasibility studies, the thesis aims to shed light on the effectiveness of this technology in addressing the growing concern of plastic pollution. The three consecutive studies presented in this thesis explore different aspects of the feasibility of using optical remote sensing for this purpose, providing a comprehensive understanding of the topic.

It demonstrates the feasibility and potential of using machine/deep learning models trained on multi-, super-, and hyperspectral satellite imagery to detect various types of plastics, and even determine their functionality on terrestrial surfaces. The first study showed that a knowledge-based classifier can be used to identify most common plastic materials of the aliphatic and aromatic groups with high hit ratios and robustness, without requiring any training data or statistical approaches. The second study demonstrated that a conventional random mixing strategy can be used to synthetically generate spectral training and test datasets from so-called endmember spectra taken from available inhouse and international accessible databases. Of several applied classifiers the RF model was shown to be the most robust and reliable and produced the best results for plastic detection at different background scenarios. Finally, the third study proposed a two-stage workflow to now assign functionality to the hyperspectral classified plastics. The results were found to be accurate for different categories, including solar panels, greenhouses, and covers of construction sites.

The combination of these three studies offers a promising approach to addressing the global plastic waste crisis, providing valuable data for pollution control and environmental management. The use of satellite imagery and deep learning models can aid in monitoring and evaluating the distribution and impact of plastic waste, helping to identify areas in need of intervention and providing guiding efforts towards a cleaner environment.

In conclusion, the results of these studies should encourage and highlight the potential of using satellite imagery and machine/deep learning models to address the plastic waste issue. The continued development of these techniques and their widespread adoption could be a significant step towards a more sustainable and environmentally conscious future.

7.2 Outlook

The trend of increased data availability is set to continue with the launch of several new hyperspectral satellite systems providing data in the VNIR-SWIR spectral range for the next few years. The development of sensor technology is anticipated to enhance spectral sampling and radiometric performance, leading to better signal-to-noise ratios at higher spatial resolutions (Rast and Painter, 2019). The German ENMAP launched on April 1, 2022 is one of a new generation of instruments (Guanter et al., 2015) that just started to provide additional hyperspectral data from space. It has similar technical specifications to PRISMA, for which applications for data acquisition were opened in late 2022. PRISMA and EnMAP will coexist with other similar and complementary missions such as the Italian-Israeli Space Hyperspectral Applications Land and Ocean Mission SHALOM (Feingersh and Dor, 2015), which supposes to obtain an increased spatial resolution of 10 m. The mission will mainly focus on commercial uses and applications in coastal zone ecosystems. Next-generation hyperspectral satellite missions launched from the mid-2020s, such as ESA's new Sentinel Candidate CHIME (Nieke and Rast, 2018), and NASA's SBG satellite (Cawse-Nicholson et al., 2021), are designed with wider swath widths providing larger scenes and an improved repetition rate allowing a higher rate of up-to-dateness. Due to an expected steady improvement of the detector technology, future hyperspectral instruments might also provide higher spatial resolutions at adequate signal to noise ratios. That would offer the possibility to detect even smaller congregations of plastic and as such more waste and garbage. Here, an ultimate objective is to utilize satellite imagery for the identification of non-functional plastic waste, and we believe that our approach can be a valuable tool for achieving this goal. Technical improvements may further help to address the presently hardly avoidable misclassification of polymers with chemical compositions similar to plastic such as asphalt, whose spectral signatures a very similar to those of plastic of the aliphatic group. Also, the effect of plastic thickness needs more accurate attention and to be considered for future quantitative studies of transparent or translucent plastic materials, as thin plastics may not be recognizable to the classifier. Further, the degradation of plastics, which often involves the breaking of chemical bonds, has not been explicitly considered, although some of the lab experiments and simulation studies conducted involved samples collected from the open environment. Future research should also explore the quantification ability of classifiers considering the thickness and degradation of plastics, as well as broadening its application to other targets. Moreover, the fusion with multi-source data to achieve additional intelligent recognition functions can be a goal for the future.

As well our study has confirmed that optical remote sensing is not sensitive enough to detect dark to black plastics with an average reflectance of less than 10%. In such cases, hyperspectral thermal sensors, which can detect the fundamental vibrations of C-H bonds in the TIR, are a more promising option. But until today only a very limited number of studies explored the feasibility of using thermal infrared wavelengths to identify plastics (Goddijn-Murphy et al., 2022; Nogo et al., 2021; Goddijn-Murphy and Williamson, 2019), and the synergistic potential of solar reflectance spectroscopy and thermal emission spectroscopy is unexplored so far. For example the ECOSystem Spaceborne Thermal Radiometer Experiment (ECOSTRESS) is equipped with a 6-band multispectral thermal camera that has been installed on the International Space Station since mid-2018 (Hook, 2019). Due to its design features, it can be considered a further promising tool for moni-

toring large-scale plastics and its effectiveness should be evaluated through testing. In this context, also very high-resolution commercial satellite data can improve the classification accuracy, but these are currently prohibitively expensive and moreover difficult to obtain.

What artificial intelligence is concerned, we will concentrate on creating deep learning models tailored specifically for the identification of spectral plastic signatures and providing more tagged data with higher spatial resolution to train these models. Thus, we intend to further develop an end-to-end deep learning model for the functional classification of plastics. Thereby, we plan to gather and tag more samples captured by different sensors and integrate this classifier with various data sources to improve its intelligent recognition capabilities. Our ultimate aim is to enhance the overall performance and usefulness of our classification scheme and make further substantial contributions to the field of plastics (waste) detection and management.

List of Figures

List of Tables

Bibliography

Abadi M, Agarwal A, Barham P, Brevdo E, Chen Z, Citro C, Corrado GS, Davis A, Dean J, Devin M, Ghemawat S, Goodfellow I, Harp A, Irving G, Isard M, Jia Y, Jozefowicz R, Kaiser L, Kudlur M, Levenberg J, Mane D, Monga R, Moore S, Murray D, Olah C, Schuster M, Shlens J, Steiner B, Sutskever I, Talwar K, Tucker P, Vanhoucke V, Vasudevan V, Viegas F, Vinyals O, Warden P, Wattenberg M, Wicke M, Yu Y, Zheng X (2016) Tensorflow: Large-scale machine learning on heterogeneous distributed systems. 1603.04467

Acuña-Ruz T, Uribe D, Taylor R, Amézquita L, Guzmán MC, Merrill J, Martínez P, Voisin L, Mattar C (2018) Anthropogenic marine debris over beaches: Spectral characterization for remote sensing applications. Remote Sensing of Environment 217:309–322

Aguilar M, Nemmaoui A, Novelli A, Aguilar F, García Lorca A (2016) Object-based greenhouse mapping using very high resolution satellite data and landsat 8 time series. Remote Sensing 8(6):513, DOI 10.3390/rs8060513

Aguilar M, Jiménez-Lao R, Nemmaoui A, Aguilar F, Koc-San D, Tarantino E, Chourak M (2020) Evaluation of the consistency of simultaneously acquired sentinel-2 and landsat 8 imagery on plastic covered greenhouses. Remote Sensing 12(12):2015, DOI 10.3390/rs12122015

Andrady AL (2017) The plastic in microplastics: A review. Marine pollution bulletin 119(1):12–22

Asadzadeh S, de Souza Filho C (2016) Investigating the capability of worldview-3 superspectral data for direct hydrocarbon detection. Remote Sensing of Environment 173(173):162–173, DOI 10.1016/j.rse.2015.11.030

Baldridge A, Hook S, Grove C, Rivera G (2009) The aster spectral library version 2.0. Remote Sensing of Environment 113(4):711–715, DOI 10.1016/j.rse.2008.11.007

Beć K, Grabska J, Czarnecki M (2018) Spectra-structure correlations in nir region: Spectroscopic and anharmonic dft study of n-hexanol, cyclohexanol and phenol. Spectrochimica Acta - Part A: Molecular and Biomolecular Spectroscopy 197:176–184, DOI 10.1016/j.saa.2018.01.041

Beć KB, Huck CW (2019) Breakthrough potential in near-infrared spectroscopy: Spectra simulation. a review of recent developments. Frontiers in Chemistry 7, DOI 10.3389/fchem.2019.00048

Behling R, Bochow M, Foerster S, Roessner S, Kaufmann H (2015) Automated gis-based derivation of urban ecological indicators using hyperspectral remote sensing and height information. Ecological Indicators 48:218–234, DOI 10.1016/j.ecolind.2014.08.003

Belgiu M, Drăgu L (2016) Random forest in remote sensing: A review of applications and future directions. ISPRS Journal of Photogrammetry and Remote Sensing 114:24–31, DOI 10.1016/j.isprsjprs.2016.01.011

Biermann L, Clewley D, Martinez-Vicente V, Topouzelis K (2020) Finding plastic patches in coastal waters using optical satellite data. Scientific Reports 10(1):5364, DOI 10.1038/s41598-020-62298-z

Bohn N, Guanter L, Kuester T, Preusker R, Segl K (2020) Coupled retrieval of the three phases of water from spaceborne imaging spectroscopy measurements. Remote Sensing of Environment 242:111708, DOI 10.1016/j.rse.2020.111708

Breiman L (2001) Random forests. Machine Learning 45(1):5–32, DOI 10.1023/A:1010933404324

Brell M, Rogass C, Segl K, Bookhagen B, Guanter L (2016) Improving sensor fusion: A parametric method for the geometric coalignment of airborne hyperspectral and lidar data. IEEE Transactions on Geoscience and Remote Sensing 54(6):3460–3474, DOI 10.1109/TGRS.2016.2518930

Browne MA, Dissanayake A, Galloway TS, Lowe DM, Thompson RC (2008) Ingested microscopic plastic translocates to the circulatory system of the mussel, *mytilus edulis* (l.). Environmental Science & Technology 42(13):5026–5031, DOI 10.1021/es800249a

Cawse-Nicholson K, Townsend P, Schimel D, Assiri A, Blake P, Buongiorno M, Campbell P, Carmon N, Casey K, Correa-Pabón R, Dahlin K, Dashti H, Dennison P, Dierssen H, Erickson A, Fisher J, Frouin R, Gatebe C, Gholizadeh H, Gierach M, Glenn N, Goodman J, Griffith D, Guild L, Hakkenberg C, Hochberg E, Holmes T, Hu C, Hulley G, Huemmrich K, Kudela R, Kokaly R, Lee C, Martin R, Miller C, Moses W, Muller-Karger F, Ortiz J, Otis D, Pahlevan N, Painter T, Pavlick R, Poulter B, Qi Y, Realmuto V, Roberts D, Schaepman M, Schneider F, Schwandner F, Serbin S, Shiklomanov A, Stavros E, Thompson D, Torres-Perez J, Turpie K, Tzortziou M, Ustin S, Yu Q, Yusup Y, Zhang Q, the SAWG (2021) Nasa's surface biology and geology designated observable: A perspective on surface imaging algorithms. Remote Sensing of Environment 257, DOI 10.1016/j.rse.2021.112349

Chapelle O, Vapnik V, Bousquet O, Mukherjee S (2002) Choosing multiple parameters for support vector machines. Machine Learning 46(1-3):131–159, DOI 10.1023/A:1012450327387

Chawla I, Karthikeyan L, Mishra AK (2020) A review of remote sensing applications for water security: Quantity, quality, and extremes. Journal of Hydrology 585:124826

Cocks T, Jenssen R, Stewart A, Wilson I, Shields T (1998) The hymaptm airborne hyperspectral sensor: The system, calibration and performance. In: Proceedings of the 1st EARSeL Workshop on Imaging Spectroscopy, pp 37–42

Cogliati S, Sarti F, Chiarantini L, Cosi M, Lorusso R, Lopinto E, Miglietta F, Genesio L, Guanter L, Damm A, Pérez-López S, Scheffler D, Tagliabue G, Panigada C, Rascher U, Dowling T, Giardino C, Colombo R (2021) The prisma imaging spectroscopy mission: Overview and first performance analysis. Remote Sensing of Environment 262, DOI 10.1016/j.rse.2021.112499

Conel JE, Green RO, Vane G, Bruegge CJ, Alley RE, Curtiss BJ (1987) Airborne imaging spectrometer-2: Radiometric spectral characteristics and comparison of ways to compensate for the atmosphere. In: Vane G (ed) 31st Annual Technical Symposium, San Diego, CA, United States, p 140, DOI 10.1117/12.942294

Cruz Sanchez FA, Boudaoud H, Camargo M, Pearce JM (2020) Plastic recycling in additive manufacturing: A systematic literature review and opportunities for the circular economy. Journal of Cleaner Production 264:121602, DOI 10.1016/j.jclepro.2020.121602

Czarnecki M, Morisawa Y, Futami Y, Ozaki Y (2015) Advances in molecular structure and interaction studies using near-infrared spectroscopy. Chemical Reviews 115(18):9707–9744, DOI 10.1021/cr500013u

Derraik JG (2002) The pollution of the marine environment by plastic debris: A review. Marine Pollution Bulletin 44(9):842–852, DOI 10.1016/S0025-326X(02)00220-5

Editor (2018) The future of plastic. Nature Communications 9(1):2157, s41467–018–04565–2, DOI 10.1038/s41467-018-04565-2

Eisenreich N, Rohe T (2006) Infrared spectroscopy in analysis of plastics recycling. Encyclopedia of Analytical Chemistry: Applications, Theory and Instrumentation

El Mahrad B, Newton A, Icely J, Kacimi I, Abalansa S, Snoussi M (2020) Contribution of remote sensing technologies to a holistic coastal and marine environmental management framework: A review. Remote Sensing 12(14):2313, DOI 10.3390/rs12142313

Fallati L, Polidori A, Salvatore C, Saponari L, Savini A, Galli P (2019) Anthropogenic marine debris assessment with unmanned aerial vehicle imagery and deep learning: A case study along the beaches of the republic of maldives. Science of The Total Environment 693:133581, DOI 10.1016/j.scitotenv.2019.133581

Fauvel M, Benediktsson J, Chanussot J, Sveinsson J (2008) Spectral and spatial classification of hyperspectral data using svms and morphological profiles. IEEE Transactions on Geoscience and Remote Sensing 46(11):3804–3814, DOI 10.1109/TGRS.2008.922034

Feingersh T, Dor EB (2015) Shalom - a commercial hyperspectral space mission. In: Qian SE (ed) Optical Payloads for Space Missions, John Wiley & Sons, Ltd, Chichester, UK, pp 247–263, DOI 10.1002/9781118945179.ch11

Feldman D (2008) Polymer history. Designed Monomers and Polymers 11(1):1–15, DOI 10.1163/156855508X292383

Garaba SP, Aitken J, Slat B, Dierssen HM, Lebreton L, Zielinski O, Reisser J (2018) Sensing ocean plastics with an airborne hyperspectral shortwave infrared imager. Environmental science & technology 52(20):11699–11707

Geyer R, Jambeck JR, Law KL (2017) Production, use, and fate of all plastics ever made. Science Advances 3(7):e1700782, DOI 10.1126/sciadv.1700782

Ghanbari H, Mahdianpari M, Homayouni S, Mohammadimanesh F (2021) A meta-analysis of convolutional neural networks for remote sensing applications. IEEE Journal of Selected Topics in Applied Earth Observations and Remote Sensing 14:3602–3613, DOI 10.1109/JSTARS.2021.3065569

Goddijn-Murphy L, Williamson B (2019) On thermal infrared remote sensing of plastic pollution in natural waters. Remote Sensing 11(18):2159

Goddijn-Murphy L, Williamson B (2019) On thermal infrared remote sensing of plastic pollution in natural waters. Remote Sensing 11(18):2159

Goddijn-Murphy L, Williamson BJ, McIlvenny J, Corradi P (2022) Using a uav thermal infrared camera for monitoring floating marine plastic litter. Remote Sensing 14(13):3179

Guanter L, Kaufmann H, Segl K, Foerster S, Rogass C, Chabrillat S, Kuester T, Hollstein A, Rossner G, Chlebek C, Straif C, Fischer S, Schrader S, Storch T, Heiden U, Mueller A, Bachmann M, Mühle H, Müller R, Habermeyer M, Ohndorf A, Hill J, Buddenbaum H, Hostert P, Van Der Linden S, Leitão P, Rabe A, Doerffer R, Krasemann H, Xi H, Mauser W, Hank T, Locherer M, Rast M, Staenz K, Sang B (2015) The enmap spaceborne imaging spectroscopy mission for earth observation. Remote Sensing 7(7):8830–8857, DOI 10.3390/rs70708830

Guarini R, Loizzo R, Facchinetti C, Longo F, Ponticelli B, Faraci M, Dami M, Cosi M, Amoruso L, De Pasquale V, et al. (2018) Prisma hyperspectral mission products. In: IGARSS 2018-2018 IEEE International Geoscience and Remote Sensing Symposium, IEEE, pp 179–182

Guénard M (2013) Cairo puts its faith in ragpickers to manage the city's waste problem. The Guardian

Guo X, Li P (2020) Mapping plastic materials in an urban area: Development of the normalized difference plastic index using worldview-3 superspectral data. ISPRS Journal of Photogrammetry and Remote Sensing 169:214–226, DOI 10.1016/j.isprsjprs.2020.09.009

Ham J, Chen Y, Crawford M, Ghosh J (2005) Investigation of the random forest framework for classification of hyperspectral data. IEEE Transactions on Geoscience and Remote Sensing 43(3):492–501, DOI 10.1109/TGRS.2004.842481

Han CG, Son MS, Choi HK (2012) Development of efficient curing sheet for thermal insulation curing of concrete in cold weather. J Korea Institute of Building Construction 12(3):291–298

Hartigan JA, Wong MA (1979) Algorithm as 136: A k-means clustering algorithm. Applied Statistics 28(1):100, DOI 10.2307/2346830, 10.2307/2346830

He K, Zhang X, Ren S, Sun J (2016) Deep residual learning for image recognition. In: Proceedings of the IEEE conference on computer vision and pattern recognition, pp 770–778

Heiden U, Segl K, Roessner S, Kaufmann H (2007) Determination of robust spectral features for identification of urban surface materials in hyperspectral remote sensing data. Remote Sensing of Environment 111(4):537–552, DOI 10.1016/j.rse.2007.04.008

Hoffbeck JP, Landgrebe DA (1996) Classification of remote sensing images having high spectral resolution. Remote Sensing of Environment 57(3):119–126

Hörig B, Kühn F, Oschütz F, Lehmann F (2001) Hymap hyperspectral remote sensing to detect hydrocarbons. International Journal of Remote Sensing 22(8):1413–1422, DOI 10.1080/01431160120909

Huth-Fehre Th, Feldhoff R, Kantimm Th, Quick L, Winter F, Cammann K, van den Broek W, Wienke D, Melssen W, Buydens L (1995) Nir - remote sensing and artificial neural networks for rapid identification of post consumer plastics. Journal of Molecular Structure 348:143–146, DOI 10.1016/0022-2860(95)08609-Y

Karthikeyan L, Chawla I, Mishra AK (2020) A review of remote sensing applications in agriculture for food security: Crop growth and yield, irrigation, and crop losses. Journal of Hydrology 586:124905

Kattenborn T, Leitloff J, Schiefer F, Hinz S (2021) Review on convolutional neural networks (cnn) in vegetation remote sensing. ISPRS Journal of Photogrammetry and Remote Sensing 173:24–49, DOI 10.1016/j.isprsjprs.2020.12.010

Keshava N, Mustard JF (2002) Spectral unmixing. IEEE signal processing magazine 19(1):44–57

Knaeps E, Sterckx S, Strackx G, Mijnendonckx J, Moshtaghi M, Garaba S, Meire D (2021) Hyperspectral-reflectance dataset of dry, wet and submerged marine litter. Earth System Science Data 13(2):713–730, DOI 10.5194/essd-13-713-2021

Kokaly RF, Clark RN, Swayze GA, Livo KE, Hoefen TM, Pearson NC, Wise RA, Benzel WM, Lowers HA, Driscoll RL (2017) Usgs spectral library version 7. Tech. rep., US Geological Survey

Kremezi M, Kristollari V, Karathanassi V, Topouzelis K, Kolokoussis P, Taggio N, Aiello A, Ceriola G, Barbone E, Corradi P (2022) Increasing the sentinel-2 potential for marine plastic litter monitoring through image fusion techniques. Marine pollution bulletin 182:113974

Kruse F, Lefkoff A, Boardman J, Heidebrecht K, Shapiro A, Barloon P, Goetz A (1993) The spectral image processing system (sips)—interactive visualization and analysis of imaging spectrometer data. Remote Sensing of Environment 44(2-3):145–163, DOI 10.1016/0034-4257(93)90013-N

Kuester T, Bochow M (2019) Spectral modeling of plastic litter in terrestrial environments - use of 3d hyperspectral ray tracing models to analyze the spectral influence of different natural ground surfaces on remote sensing based plastic mapping. In: 2019 10th Workshop on Hyperspectral Imaging and Signal Processing: Evolution in Remote Sensing (WHISPERS), IEEE, Amsterdam, Netherlands, pp 1–7, DOI 10.1109/WHISPERS.2019.8920847

Kuester T, Spengler D, Barczi JF, Segl K, Hostert P, Kaufmann H (2014) Simulation of multi-temporal and hyperspectral vegetation canopy bidirectional reflectance using detailed virtual 3-d canopy models. IEEE Transactions on Geoscience and Remote Sensing 52(4):2096–2108, DOI 10.1109/TGRS.2013.2258162

Kühn F, Oppermann K, Hörig B (2004) Hydrocarbon index - an algorithm for hyperspectral detection of hydrocarbons. International Journal of Remote Sensing 25(12):2467–2473, DOI 10.1080/01431160310001642287

Küster T (2011) Modellierung von getreidebestandsspektren zur korrektur brdf-bedingter einflüsse auf vegetationsindizes im rahmen der enmap-mission

Kwan C, Ayhan B, Chen G, Jing Wang, Baohong Ji, Chein-I Chang (2006) A novel approach for spectral unmixing, classification, and concentration estimation of chemical and biological agents. IEEE Transactions on Geoscience and Remote Sensing 44(2):409–419, DOI 10.1109/TGRS.2005.860985

Kwan C, Ayhan B, Budavari B, Lu Y, Perez D, Li J, Bernabe S, Plaza A (2020) Deep learning for land cover classification using only a few bands. Remote Sensing 12(12):2000, DOI 10.3390/rs12122000

Lanorte A, De Santis F, Nolè G, Blanco I, Loisi R, Schettini E, Vox G (2017) Agricultural plastic waste spatial estimation by landsat 8 satellite images. Computers and Electronics in Agriculture 141:35–45, DOI 10.1016/j.compag.2017.07.003

Law K (2017) Plastics in the marine environment. Annual Review of Marine Science 9(1):205–229, DOI 10.1146/annurev-marine-010816-060409

Law KL, Thompson RC (2014) Microplastics in the seas. Science 345(6193):144–145, DOI 10.1126/science.1254065

Lebreton LCM, van der Zwet J, Damsteeg JW, Slat B, Andrady A, Reisser J (2017) River plastic emissions to the world's oceans. Nature Communications 8(1):15611, DOI 10.1038/ncomms15611

LeCun Y, Bengio Y, Hinton G (2015) Deep learning. Nature 521(7553):436–444, DOI 10.1038/nature14539

Li W, Tse H, Fok L (2016) Plastic waste in the marine environment: A review of sources, occurrence and effects. Science of the Total Environment 566–567:333–349, DOI 10.1016/j.scitotenv.2016.05.084

Lithner D, Larsson A, Dave G (2011) Environmental and health hazard ranking and assessment of plastic polymers based on chemical composition. Science of the Total Environment 409(18):3309–3324, DOI 10.1016/j.scitotenv.2011.04.038

Liu YN, Sun DX, Hu XN, Ye X, Li YD, Liu SF, Cao KQ, Chai MY, Zhou WYN, Zhang J, Zhang Y, Sun WW, Jiao LL (2019) The advanced hyperspectral imager: Aboard china's gaofen-5 satellite. IEEE Geoscience and Remote Sensing Magazine 7(4):23–32, DOI 10.1109/MGRS.2019.2927687

Loshchilov I, Hutter F (2019) Decoupled weight decay regularization. `1711.05101`

Lu T, Li S, Fang L, Jia X, Benediktsson J (2017) From subpixel to superpixel: A novel fusion framework for hyperspectral image classification. IEEE Transactions on Geoscience and Remote Sensing 55(8):4398–4411, DOI 10.1109/TGRS.2017.2691906

Ma L, Liu Y, Zhang X, Ye Y, Yin G, Johnson BA (2019a) Deep learning in remote sensing applications: A meta-analysis and review. ISPRS Journal of Photogrammetry and Remote Sensing 152:166–177, DOI 10.1016/j.isprsjprs.2019.04.015

Ma L, Peng Y, Pei Y, Zeng J, Shen H, Cao J, Qiao Y, Wu Z (2019b) Systematic discovery about nir spectral assignment from chemical structural property to natural chemical compounds. Scientific Reports 9(1):9503, DOI 10.1038/s41598-019-45945-y

Madhvee D, Shobha J, Nidhi R (2022) Impact of plastic pollution on wildlife and its natural habitat. Pharma Innov J 11(6S):141–143

Martínez-Vicente V, Clark JR, Corradi P, Aliani S, Arias M, Bochow M, Bonnery G, Cole M, Cózar A, Donnelly R, Echevarría F, Galgani F, Garaba SP, Goddijn-Murphy L, Lebreton L, Leslie HA, Lindeque PK, Maximenko N, Martin-Lauzer FR, Moller D, Murphy P, Palombi L, Raimondi V, Reisser J, Romero L, Simis SG, Sterckx S, Thompson RC, Topouzelis KN, van van Sebille E, Veiga JM, Vethaak AD (2019) Measuring marine plastic debris from space: Initial assessment of observation requirements. Remote Sensing 11(20):2443, DOI 10.3390/rs11202443

Masoumi H, Safavi SM, Khani Z (2012) Identification and classification of plastic resins using near infrared reflectance. Int J Mech Ind Eng 6:213–220

Meerdink SK, Hook SJ, Roberts DA, Abbott EA (2019) The ecostress spectral library version 1.0. Remote Sensing of Environment 230:111196, DOI 10.1016/j.rse.2019.05.015

Melgani F, Bruzzone L (2004) Classification of hyperspectral remote sensing images with support vector machines. IEEE Transactions on Geoscience and Remote Sensing 42(8):1778–1790, DOI 10.1109/TGRS.2004.831865

MIRANDA LJ (2017) Understanding softmax and the negative log-likelihood. https://ljvmiranda921.github.io/notebook/2017/08/13/softmax-and-the-negative-log-likelihood/

Moller D, Chao Y, Maximenko N (2016) Remote sensing of marine debris. In: International Geoscience and Remote Sensing Symposium (IGARSS), IEEE, Beijing, China, vol 2016-November, pp 7690–7693, DOI 10.1109/IGARSS.2016.7731005

Moroni M, Mei A, Leonardi A, Lupo E, La Marca F (2015) Pet and pvc separation with hyperspectral imagery. Sensors (Switzerland) 15(1):2205–2227, DOI 10.3390/s150102205

Moshtaghi M, Knaeps E, Sterckx S, Garaba S, Meire D (2021) Spectral reflectance of marine macroplastics in the vnir and swir measured in a controlled environment. Scientific reports 11(1):5436, DOI 10.1038/s41598-021-84867-6

Moy K, Neilson B, Chung A, Meadows A, Castrence M, Ambagis S, Davidson K (2018) Mapping coastal marine debris using aerial imagery and spatial analysis. Marine Pollution Bulletin 132:52–59, DOI 10.1016/j.marpolbul.2017.11.045

Nieke J, Rast M (2018) Towards the copernicus hyperspectral imaging mission for the environment (chime). In: Igarss 2018-2018 ieee international geoscience and remote sensing symposium, IEEE, pp 157–159

Nogo K, Ikejima K, Qi W, Kawashima N, Kitazaki T, Adachi S, Wada K, Nishiyama A, Ishimaru I (2021) Identification of black microplastics using long-wavelength infrared hyperspectral imaging with imaging-type two-dimensional fourier spectroscopy. Analytical Methods 13(5):647–659

Novelli A, Aguilar MA, Nemmaoui A, Aguilar FJ, Tarantino E (2016) Performance evaluation of object based greenhouse detection from sentinel-2 msi and landsat 8 oli data: A case study from almería (spain). International Journal of Applied Earth Observation and Geoinformation 52:403–411, DOI 10.1016/j.jag.2016.07.011

Oreski G, Eder G, Voronko Y, Omazic A, Neumaier L, Mühleisen W, Ujvari G, Ebner R, Edler M (2021) Performance of pv modules using co-extruded backsheets based on polypropylene. Solar Energy Materials and Solar Cells 223:110976, DOI 10.1016/j.solmat.2021.110976

Pedregosa F, Varoquaux G, Gramfort A, Michel V, Thirion B, Grisel O, Blondel M, Prettenhofer P, Weiss R, Dubourg V, Vanderplas J, Passos A, Cournapeau D, Brucher M, Perrot M, Duchesnay É (2011) Scikit-learn: Machine learning in python. Journal of Machine Learning Research 12(85):2825–2830

Rani M, Marchesi C, Federici S, Rovelli G, Alessandri I, Vassalini I, Ducoli S, Borgese L, Zacco A, Bilo F, Bontempi E, Depero LE (2019) Miniaturized near-infrared (micronir) spectrometer in plastic waste sorting. Materials 12(17):2740, DOI 10.3390/ma12172740

Rasheed A, Kwak CS, Kim HT, Lee HW (2020) Building energy an simulation model for analyzing energy saving options of multi-span greenhouses. Applied Sciences 10(19):6884, DOI 10.3390/app10196884

Rast M, Painter TH (2019) Earth observation imaging spectroscopy for terrestrial systems: An overview of its history, techniques, and applications of its missions. Surveys in Geophysics 40(3):303–331

Rast M, Ananasso C, Bach H, Ben-Dor E, Chabrillat S, Colombo R, Bello UD, Feret JB, Giardino C, Green RO, Guanter L, Marsh S, Nieke J, Ong CCH, Rum G, Schaepman ME, Schlerf M, Skidmore AK, Strobl P (2019) Copernicus hyperspectral imaging mission for the environment: Mission requirements document

Richards JA (2021) Remote Sensing Digital Image Analysis, 6th edn. Springer, Berlin Heidelberg

Richter R, Schläpfer D (2007) Atmospheric/topographic correction for satellite imagery: Atcor-2/3 user guide. DLR IB pp 565–01

Richter R, Schläpfer D (2019) Atmospheric and topographic correction (atcor theoretical background document). DLR IB 1:0564–03

Rochman CM, Browne MA, Halpern BS, Hentschel BT, Hoh E, Karapanagioti HK, Rios-Mendoza LM, Takada H, Teh S, Thompson RC (2013) Classify plastic waste as hazardous. Nature 494(7436):169–171, DOI 10.1038/494169a

Rogass C, Koerting FM, Mielke C, Brell M, Boesche NK, Bade M, Hohmann C (2017) Translational imaging spectroscopy for proximal sensing. Sensors 17(8):1857, DOI 10.3390/s17081857

Royer SJ, Ferrón S, Wilson ST, Karl DM (2018) Production of methane and ethylene from plastic in the environment. PLOS ONE 13(8):e0200574, DOI 10.1371/journal.pone.0200574

Sahajwalla V, Gaikwad V (2018) The present and future of e-waste plastics recycling. Current Opinion in Green and Sustainable Chemistry 13:102–107, DOI 10.1016/j.cogsc.2018.06.006

Sassi A, Stefanescu A, Menaspa P, Bosio A, Riggio M, Rampinini E (2011) The cost of running on natural grass and artificial turf surfaces. Journal of Strength and Conditioning Research 25(3):606–611, DOI 10.1519/JSC.0b013e3181c7baf9

Scarascia-Mugnozza G, Sica C, Russo G (2011) Plastic materials in european agriculture: Actual use and perspectives. Journal of Agricultural Engineering 42(3):15–28, DOI 10.4081/jae.2011.3.15

Schläpfer D, Richter R (2002) Geo-atmospheric processing of airborne imaging spectrometry data. part 1: Parametric orthorectification. International Journal of Remote Sensing 23(13):2609–2630, DOI 10.1080/01431160110115825

Schluep M, Terekhova T, Manhart A, Müller E, Rochat D, Osibanjo O (2012) Where are weee in africa? In: 2012 Electronics Goes Green 2012+, pp 1–6

Schmidhuber J (2015) Deep learning in neural networks: An overview. Neural Networks 61:85–117, DOI 10.1016/j.neunet.2014.09.003

Schwanninger M, Rodrigues JC, Fackler K (2011) A review of band assignments in near infrared spectra of wood and wood components. Journal of Near Infrared Spectroscopy 19(5):287–308, DOI 10.1255/jnirs.955

Shimabukuro YE, Smith JA (1991) The least-squares mixing models to generate fraction images derived from remote sensing multispectral data. IEEE Transactions on Geoscience and Remote sensing 29(1):16–20

Simonyan K, Zisserman A (2014) Very deep convolutional networks for large-scale image recognition. arXiv preprint arXiv:14091556

Smith ML, Smith LN, Hansen MF (2021) The quiet revolution in machine vision-a state-of-the-art survey paper, including historical review, perspectives, and future directions. Computers in Industry 130:103472

Sun H, Wang L, Lin R, Zhang Z, Zhang B (2021) Mapping plastic greenhouses with two-temporal sentinel-2 images and 1d-cnn deep learning. Remote Sensing 13(14):2820, DOI 10.3390/rs13142820

Swayze GA, Clark RN, Goetz AF, Chrien TG, Gorelick NS (2003) Effects of spectrometer band pass, sampling, and signal-to-noise ratio on spectral identification using the tetracorder algorithm. Journal of Geophysical Research: Planets 108(E9)

Szegedy C, Liu W, Jia Y, Sermanet P, Reed S, Anguelov D, Erhan D, Vanhoucke V, Rabinovich A (2014) Going deeper with convolutions. DOI 10.48550/arXiv.1409.4842, `arXiv:1409.4842`

Szegedy C, Liu W, Jia Y, Sermanet P, Reed S, Anguelov D, Erhan D, Vanhoucke V, Rabinovich A (2015) Going deeper with convolutions. In: Proceedings of the IEEE conference on computer vision and pattern recognition, pp 1–9

Teuten EL, Saquing JM, Knappe DRU, Barlaz MA, Jonsson S, Björn A, Rowland SJ, Thompson RC, Galloway TS, Yamashita R, Ochi D, Watanuki Y, Moore C, Viet PH, Tana TS, Prudente M, Boonyatumanond R, Zakaria MP, Akkhavong K, Ogata Y, Hirai H, Iwasa S, Mizukawa K, Hagino Y, Imamura A, Saha M, Takada H (2009) Transport and release of chemicals from plastics to the environment and to wildlife. Philosophical Transactions of the Royal Society B: Biological Sciences 364(1526):2027–2045, DOI 10.1098/rstb.2008.0284

Themistocleous K, Papoutsa C, Michaelides S, Hadjimitsis D (2020) Investigating detection of floating plastic litter from space using sentinel-2 imagery. Remote Sensing 12(16):2648, DOI 10.3390/rs12162648

Tong X, Tian F, Brandt M, Liu Y, Zhang W, Fensholt R (2019) Trends of land surface phenology derived from passive microwave and optical remote sensing systems and associated drivers across the dry tropics 1992–2012. Remote Sensing of Environment 232:111307

Topouzelis K, Papageorgiou D, Karagaitanakis A, Papakonstantinou A, Arias Ballesteros M (2020) Remote sensing of sea surface artificial floating plastic targets with sentinel-2 and unmanned aerial systems (plastic litter project 2019). Remote Sensing 12(12):2013, DOI 10.3390/rs12122013

Topouzelis K, Papageorgiou D, Suaria G, Aliani S (2021) Floating marine litter detection algorithms and techniques using optical remote sensing data: A review. Marine Pollution Bulletin 170:112675, DOI 10.1016/j.marpolbul.2021.112675

Tou JT, Gonzalez RC (1974) Pattern recognition principles

Toure S, Diop O, Kpalma K, Maiga AS (2019) Shoreline detection using optical remote sensing: A review. ISPRS International Journal of Geo-Information 8(2):75

Tremlett G (2013) Spanish sperm whale death linked to uk supermarket supplier's plastic. The Guardian

Uhrin AV, Schellinger J (2011) Marine debris impacts to a tidal fringing-marsh in north carolina. Marine Pollution Bulletin 62(12):2605–2610, DOI 10.1016/j.marpolbul.2011.10.006

US EPA (2002) Guidelines for ensuring and maximizing the quality, objectivity, utility, and integrity of information disseminated by federal agencies; republication. https://www.federalregister.gov/documents/2002/02/22/R2-59/guidelines-for-ensuring-and-maximizing-the-quality-objectivity-utility-and-integrity-of-information

Van der Meer, de Jong SM (2011) Imaging Spectrometry: Basic Principles and Prospective Applications. Springer Science & Business Media

Veettil BK, Quan NH, Hauser LT, Van DD, Quang NX (2022) Coastal and marine plastic litter monitoring using remote sensing: A review. Estuarine, Coastal and Shelf Science p 108160

Vincent P, de Brébisson A, Bouthillier X (2015) Efficient exact gradient update for training deep networks with very large sparse targets. In: Advances in Neural Information Processing Systems, Curran Associates, Inc., vol 28

Vishwakarma A (2020) Unsustainable management of plastic wastes in india: A threat to global warming and climate change. In: Singh P, Singh RP, Srivastava V (eds) Contemporary Environmental Issues and Challenges in Era of Climate Change, Springer Singapore, Singapore, pp 235–244, DOI 10.1007/978-981-32-9595-7_13

Wetherley EB, Roberts DA, McFadden JP (2017) Mapping spectrally similar urban materials at sub-pixel scales. Remote Sensing of Environment 195:170–183, DOI 10.1016/j.rse.2017.04.013

Woods E (2011) Garbage city. Virginia Quarterly Review 87(2):4–27

Yan H, Siesler H (2018) Identification performance of different types of handheld near-infrared (nir) spectrometers for the recycling of polymer commodities. Applied Spectroscopy 72(9):1362–1370, DOI 10.1177/0003702818777260

Yu S, Jia S, Xu C (2017) Convolutional neural networks for hyperspectral image classification. Neurocomputing 219:88–98, DOI 10.1016/j.neucom.2016.09.010

Zhou S, Kuester T, Bochow M, Bohn N, Brell M, Kaufmann H (2021) A knowledge-based, validated classifier for the identification of aliphatic and aromatic plastics by worldview-3 satellite data. Remote Sensing of Environment 264:112598, DOI 10.1016/j.rse.2021.112598

Zhou S, Kaufmann H, Bohn N, Bochow M, Kuester T, Segl K (2022) Identifying distinct plastics in hyperspectral experimental lab-, aircraft-, and satellite data using machine/deep learning methods trained with synthetically mixed spectral data. Remote Sensing of Environment 281:113263, DOI 10.1016/j.rse.2022.113263

Zhu XX, Tuia D, Mou L, Xia GS, Zhang L, Xu F, Fraundorfer F (2017) Deep learning in remote sensing: A comprehensive review and list of resources. IEEE Geoscience and Remote Sensing Magazine 5(4):8–36, DOI 10.1109/MGRS.2017.2762307